THE UNIVERSITY OF CHICAGO

CREATING COMPRESSIBLE MANY-BODY STATES OF LIGHT THROUGH ADIABATIC TUNING OF DISORDER

A DISSERTATION SUBMITTED TO
THE FACULTY OF THE DIVISION OF THE PHYSICAL SCIENCES
IN CANDIDACY FOR THE DEGREE OF
DOCTOR OF PHILOSOPHY

DEPARTMENT OF PHYSICS

BY
BRENDAN SAXBERG

CHICAGO, ILLINOIS
MARCH 2023

Copyright © 2023 by Brendan Saxberg

All Rights Reserved

TABLE OF CONTENTS

LIST OF FIGURES

LIST OF TABLES

ACKNOWLEDGMENTS

It is impossible to thank each person that helped me on my journey to this point. I've shared countless moments with so many that have accumulated to not just this work, but my entire P.h.D. Understand that this section is incomplete.

First, I would like to thank my undergraduate research advisor Subhadeep Gupta for taking a chance on me as an undergraduate researcher and giving me a space to grow as an experimentalist at the University of Washington. I would particularly like to call out the opportunity afforded to me during the gap year of continuing to do research in the lab, simulating the graduate school experience of dedicated research and publishing a paper. Each event in our lives snowball into the rest, but some are more critical than others. In this case I believe this mattered quite a lot, influencing the trajectory of my life further pursuing academics.

I would like to thank my current research advisors: Jonathan Simon and David Schuster. The mutually constructive non-linear (classical?) interactions between these two not only produced the very quantum simulation project that motivated me to shift from ultracold atoms research, but continued to produce science, direction, ideas, and guidance that I found invaluable throughout my time at the University of Chicago. I am sure their futures will continue to be bright, but I will still wish the best for them here as they continue on at Stanford (though after the transition we will lose the delocalization jokes about "finding your advisor" spanning multiple states).

I would like to extend thanks to Alex Ruichao Ma, a postdoctoral researcher on the quantum simulation team who I worked quite closely with in my initial years. As a fresh-faced graduate student on-boarding onto this project, I absorbed knowledge from him each day like a dry sponge thrown into the ocean. Within him, I saw qualities of a very successful scientist that I have tried to replicate in myself. I was very happy for him when I heard the news of his new role as a professor at Purdue, and though it has been several years since the

transition for him I wish him continued success.

I would like to extend special thanks to Gabrielle Roberts, a fellow graduate student researcher, and Andrei Vrajitoarea, a postdoctoral scholar, who joined the quantum simulation group in 2019 and 2020 respectively. Both have been fantastic additions and wonderful coworkers to tackle the myriad challenges we face in giving microwave light some character. Indeed, despite the setbacks we faced, which include an entire global pandemic, working with Gabrielle and Andrei seemlessly produced great scientific work through quality teamwork. If I could put them in my pocket and take them with me to my next job I would.

When I finished defending I was asked many times how I felt, if I felt a sense of relief now that it was over. I can say truthfully that while there were difficulties throughout the experience, the sensation at the end was more a chapter closing. I will miss the many members of the Simon and Schuster labs, past and present. this has truly been a remarkable journey.

ABSTRACT

Creating a desired many-body state within large quantum systems is a common desire among several related fields, ranging from quantum information science to many-body physics and quantum metrology. In this work we demonstrate state preparation using a low-complexity technique by combining two common methods: step-by-step assembly and adiabatic evolution, to create low-entropy quantum many-body fluids of light. These fluid-like states of light are generated on our Bose-Hubbard chain of flux-tunable transmon qubits. By tuning the on-site energies of each qubit we start in a disordered lattice where the eigenstates are known and localized to single sites (qubits). We create individual excitations, then adiabatically remove the disorder allowing quantum fluctuations to melt the localized photons into a fluid. We first benchmark this lattice melting technique by building and characterizing arbitrary single particle-in-a-box states, then assemble multi-particle strongly correlated fluids. Inter-site entanglement measurements indicate that the particles in the fluid delocalize, while two-body density correlation measurements demonstrate that they also avoid one another, revealing Friedel oscillations characteristic of a Tonks-Girardeau gas. This work opens new possibilities for preparation of topological and otherwise exotic phases of synthetic matter.

CHAPTER 1

INTRODUCTION

In P.W. Anderson's "More is Different" [3], he presents a well-known argument against reductionism stating that when given the ability to reduce everything to simple fundamental physical laws, one is not guaranteed to be able to use those laws and replicate the world. The emergent properties that arise at each new physical scale can defy simple extrapolation of principles at smaller scales, and thus the study of the emergent itself become fundamental.

Understanding phenomena that arise due to the physics from many particles in interacting materials is the heart of condensed-matter physics. Some of these are well understood, such as the familiar first-order phase transition of boiling water, or the band-structure of electrons giving us the transistor [4]. Even systems demonstrating macroscopic quantum phenomena, such as the observation of superfluidity in a mixture of Helium isotopes [5] or Bose-Einstein Condensates made of atoms suspended in a vacuum chamber [6, 7], while exotic, are captured by descriptions at the microscopic scale due to the non-interacting or weakly-interacting nature of their constituent components.

Our interest lies in improving our understanding in systems that are not as well understood due to the strongly interacting and strongly correlated nature of their components. These dynamics at the microscopic scale can produce rich, but poorly understood phenomena at the macroscopic scale. Techniques to simplify, such as mean field theory, often fail to produce effective models. For instance, the fractional quantum hall effect [8, 9] shows an emergent fractionalized Hall conductance due to the collective behavior of electrons interacting within the confines of the two-dimensional electron surface in the presence of an external magnetic field. Another example of a system where strong correlations at the microscopic scale produce flavorful behavior at the macroscopic scale are high-T_c superconductors, such as cuprates, where interactions between electrons within the material generate macroscopic superconductivity at higher temperatures than other materials whose superconductivity is

governed by correlations explained by the momentum-pairing in BCS theory [10, 11].

To understand why these many-body, strongly correlated systems in the quantum regime are difficult to build theoretical descriptions of, let us consider the tools we have available. Directly studying the materials themselves can be difficult - establishing the relationship between the macroscopic behavior and the microscopic dynamics in real materials requires understanding the dynamics of these strongly correlated electrons. Direct classical computation of quantum many-body systems is exponentially expensive [12], requiring instead that we construct a quantum computer to compete with the growth in computational complexity. An alternative to building such a device (despite incredible efforts to do so) is to build an analogous system that behaves according to the same underlying physical principles - a quantum simulator. When building a quantum simulator, our goal is to directly implement the physical dynamics we wish to study, then learn from them. With this method of experiment we are free from the needs of replicating all properties the the real-space system and can design a platform that is more advantageous to our experimentation.

As such, quantum simulation is a popular method for studying macroscopic quantum many-body properties. One such platform uses ultracold atoms suspended in laser light in an ultra-high vacuum chamber. In this implementation, the atoms are manipulated directly with light [13] to generate an ever expanding set of quantum phenomena. In this platform the canonical critical quantum phase transition between a superfluid and a Mott insulator state [14] was observed in a Bose-Einstein Condensate of Rubidium. Site-resolved dynamics [15] using a grid of light, and time-resolved dynamics [16] within these quantum gas microscopes make this platform suited for performing quantum simulation experiments, such as bad metallic transport within the Fermi-Hubbard model [17], direct measurements of entanglement via interference [18], or quantum scarring [19]. Another platform, trapped ions, confine and manipulate an array of charged atoms with the coulomb force in a confining Penning or Paul trap [20]. Using these ions one can create experiments involving Quantum

reservoir engineering [21], phase transitions from paramagnetic to ferromagnetic order [22], observe emergent hydrodynamics from long-range interactions [23], or extending the Ising model interactions to hundreds of spins [24].

In this work we use another platform for quantum simulation - photons in superconducting qubits [25, 26]. Our specific circuit is a one-dimensional chain of capacitively coupled transmon qubits. The nearest-neighbor tunneling and nonlinearity of the qubits create a Bose-Hubbard model simulator for photons. In this context we can think of qubits as lattice sites for microwave photon excitations which can tunnel between sites if qubits are coupled together. We generate interacting physics for photons by mediating photon-photon collisions through the nonlinear qubits. Other simulation platforms exist to create interactions and topologies for systems comprised of light [27]. Superconducting circuits have proven quite successful for quantum simulation with demonstrations of many-body localization [28, 29], dissipative phase transitions [30], flat [31, 32] and chiral [33] lattice structures.

In our platform, and indeed all platforms, we are performing two steps when starting these simulation experiments: Hamiltonian engineering and state preparation. So far we have discussed the first. We must choose a physical state within a designed physical system to study, then find a way to prepare this specific state. In the case of quantum many-body systems, particularly systems that replicate the strongly interacting and strongly correlated physics that motivate these experiments to begin with, these states can become quite complex and difficult to generate.

There are broadly three common methods for initializing quantum states: step-by-step, adiabatic, and dissipative. Step-by-step assembly by gates is common in digital quantum simulation and was recently used in the superconducting qubit platform to generate non-abelian exchange statistics of a surface code on a quantum processor [34]. Adiabatic state preparation involves the manipulation of the Hamiltonian by some tunable parameter such that the states follow the instantaneous eigenstates of the tuned Hamiltonian. This technique

is used often in the ultracold atoms context to move from the a B.E.C. ground state to a new known ground state [15, 35]. Dissipative state preparation [36] is quite useful in overcoming the inherent loss systems built from photons experience through automatic repumping of population number. In previous work we used this method to stabilize the unit-filled Mott-insulator state on a chain of transmon qubits [37].

Here, we approach state preparation on our one-dimensional lattice of transmon qubits is two-fold: we combine step-by-step assembly of qubit excitations with adiabatic manipulation of tunable disorder to prepare delocalized and entangled many-body fluids of light on the lattice. Our one-dimensional lattice of flux-tunable transmons are individually capable of tuning their on-site energies via locally threading an external magnetic field, allowing us to impart an arbitrary potential landscape, or disorder, to the lattice. When the detuning is much larger than the nearest-neighbor tunneling rate, the hybridization between sites is suppressed and the energy eigenstates of the system are localized to individual qubits. In this phase, our system is a direct-product of the states of each qubit, allowing us to prepare any chosen energy eigenstate by manipulating individual qubits. As we remove the disorder adiabatically, we follow the instantaneous eigenstates of the tunable parameter, disorder, until the disorder is removed and we arrive at the equivalent eigenstate of the disorder-less lattice. Via the adiabatic theorem we build a map between each of the energy eigenstates of the disorder-less Bose-Hubbard lattice and the direct-product disordered array of individual qubits, thus we are able to prepare a chosen eigenstate in the disorder-less case.

Using this method of state preparation, we create the delocalized and entangled compressible eigenstates in the disorder-less limit and examine them. With only a single particle, the final eigenstates are indistinguishable from the non-interacting particle-in-a-box picture, which we show for a few quasi-momenta. As our system is strongly-interacting, the presence of multiple photons allows collision and pushes our state distribution far from what we expect from a non or weakly interacting picture with condensation. We look at the lowest

quasi-momenta state for all compressible states below unit filling on our lattice. Additionally we perform simultaneous readout and look at conditional probability and $g^(2)(x)$ density-density correlation functions to probe the structure of the multi - photon states and show the interaction term results in anti-bunching for photons on the lattice. Finally, we track the delocalization of excitations from the localized disordered single-particle excitations to the delocalized disorder-less lattice configuration through the global entanglement metric.

The structure of this thesis is as follows: in chapter two, we discuss the basic building blocks of circuit QED needed to create the quantum simulator and interact with it, as well as design and simulation discussions. Chapter three discusses the creation of the sample in a cleanroom facility and transitions into the surrounding experimental setup at cryogenic and room temperatures. In chapter four the sample is ready to measure and calibration experiments to characterize the sample are discussed. Once these are completed, we move to the next chapter where the main experimental results of the adiabatic state preparation protocol and state characterization are presented. Finally, in chapter six, we conclude and briefly touch on future work possible with this setup and these prepared states.

CHAPTER 2

BUILDING BLOCKS OF CIRCUIT QUANTUM ELECTRODYNAMICS

To perform quantum simulation using superconducting circuits, we must create such systems from the bottom up out of circuit elements. Here we will motivate the design of the basic transmon qubit, the SQUID, connecting a resonator dispersively for reading out the state of the qubit, and purcell filtering. The following discussions on the building blocks in Circuit Quantum Electrodynamics can be found in [38] and [39].

2.1 The Quantum Harmonic Oscillator

A classical lumped element LC harmonic oscillator is formed when we connect an inductor and capacitor in parallel. Recall that the inductive energy $E_{ind} = LI^2$ and the capacitive energy $E_{cap} = CV^2$. Expressing the Hamiltonian using the conjugate variable pair of charge q on the capacitor and flux ϕ in the inductor we have:

$$H = \frac{\phi^2}{2L} + \frac{q^2}{2C}$$

Note that

$$\frac{\partial H}{\partial \phi} = \frac{\phi}{L} = I = \dot{q}$$

$$\frac{\partial H}{\partial q} = \frac{q}{C} = V = -L\dot{I} = -\dot{\phi}$$

So q,ϕ are conjugate variables and can be identified as generalized position and momentum variables, satisfying $[\hat{\phi}, \hat{q}] = -i\hbar$

The above is also seen in the form

$$H = 4E_c\hat{n}^2 + \frac{1}{2}E_L\hat{\phi}^2$$

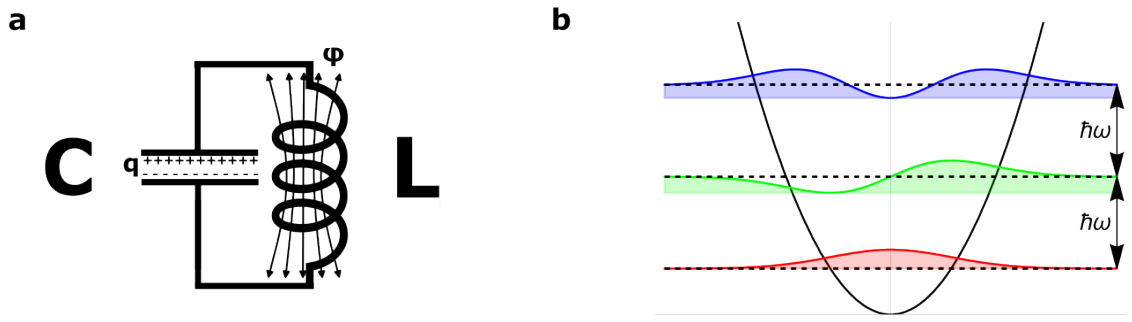

Figure 2.1: **Quantization of the LC harmonic oscillator**. By treating the flux and the inductive energy as a momentum and kinetic energy, and the charge and capacitive energy as an effective position and potential energy, the LC electronic oscillator has the same dynamics as a classical particle in a harmonic trap. Quantization of the conjugate variables proceeds the same way.

where $E_c = e^2/2C$ and $E_L = (\Phi_0)^2/L$ are the charging energy and inductive energy.

We can match the electronic Hamiltonian to the classical Hamiltonian and replace the variables needed for second quantization:

$$H = \frac{\hat{p}}{2m} + \frac{1}{2}m\omega^2\hat{x}^2 = \hbar\omega(a^\dagger a + \frac{1}{2})$$

where $\omega = \frac{1}{\sqrt{LC}} = \frac{\sqrt{8E_L E_c}}{\hbar}$. Here Ladder operators take the form:

$$a = \frac{\hat{q}}{\sqrt{2\hbar\omega C}} + \frac{i\hat{\phi}}{\sqrt{2\hbar\omega L}}$$

$$a^\dagger = \frac{\hat{q}}{\sqrt{2\hbar\omega C}} - \frac{i\hat{\phi}}{\sqrt{2\hbar\omega L}}$$

and energy eigenstates, called Fock states, satisfy

$$H|n\rangle = \hbar\omega(a^\dagger a + \frac{1}{2})|n\rangle = \hbar\omega(n + 1/2)|n\rangle$$

The energy eigenstates, or Fock states, of this system are quantized excitations - each additional excitation adds the same amount of energy to the system as the excitation before.

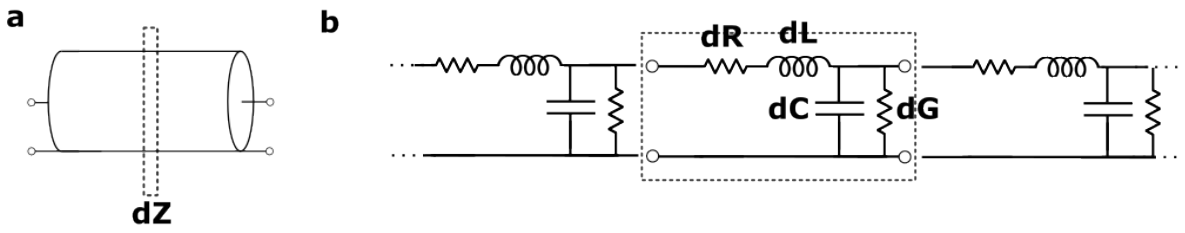

Figure 2.2: **Circuit Model of the Transmission Line**. **a** A cartoon depiction of the transmission line as a circuit element, resembling a coaxial cable with a pin and ground. A differential slice is depicted. **b** "zooming in" on a slice of the transmission line, we see an equivalent description of the transmission line as an infinite series of lumped element resonators, responsible for modeling loss, and capacitance and inductance, responsible for modeling the reactive component of the impedance.

This linearity is a defining property of the harmonic oscillator.

2.2 Transmission Lines

Transmission lines allow us to propagate electromagnetic signals over distances greatly exceeding the wavelengths within that signal. In this experiment we create transmission lines using the geometries of coaxial cables and coplanar waveguides to route microwave signals to and from our Bose-Hubbard lattice. Modifying the geometry of transmission lines offer the potential for microwave engineering outside the lumped-element regime as the physical size of the device can exceed the relevant wavelengths of interest. Although in this work we do not create distributed-element microwave devices using transmission lines such as the SIPF [40], it is good to understand how we end up using a resonance (which can be modeled as a single pole LC circuit as above) from a transmission line. The following discussion mostly comes from Chapter 2 of [41].

A classical transmission line can be modeled as a continuum of differential L's,C's, and R's when we consider normalizing over space. R_l and G_l comprise the loss of the transmission line, and are associated with conductor loss and dielectric loss respectively. For a lossless transmission line $R_l, G_l \to 0$, leaving only the capacitance C and inductance L to define the

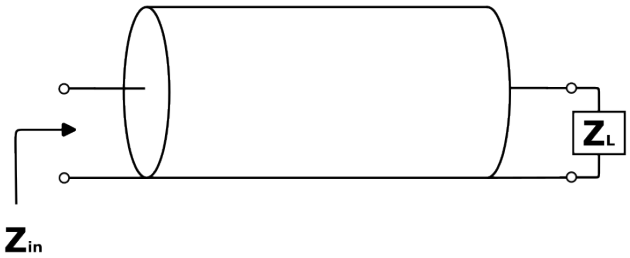

Figure 2.3: **Transmission Line Input Impedance**. We can connect a load Z_L to the transmission line, shown here schematically. This allows us to interact with the load over a long electrical distance, or we can interpret this as altering the electrical properties of the transmission line itself (understood by calculating the input impedance Z_{in}).

impedance.

We see the impedance of a small section (Fig. 2.2) of the transmission line is

$$Z_0 = \sqrt{\frac{R + j\omega L}{G + J\omega C}}$$

and in the limit of no dissipation $Z_0 \to \sqrt{L/C}$. When solving the classical telegrapher's equations on this system one encounters the complex wave propagation coefficient: $\gamma = \sqrt{(R + j\omega L)(G + j\omega C)}$. Decomposing $\gamma = \alpha + j\beta$ with α, β real, α describes the amplitude variation and β describes the phase information of the wave. For a wave travelling on the line the phase velocity is $v_p = \omega/\beta$ and the wavelength is given by $\lambda = 2\pi/\beta$. With a lossless line, $R = G = \alpha = 0$ and $\beta = \omega\sqrt{LC}$.

When we connect circuit components to the ends of transmission lines that load changes the "flat" travelling wave behavior. The impedance of a transmission line of length l with a load Z_L connected to it is

$$Z_{input} = Z_0 \left(\frac{Z_L + Z_0 \tanh \gamma l}{Z_0 + Z_L \tanh \gamma l} \right)$$

where Z_0 is the characteristic impedance of the transmission line.

2.3 Transmission Line Resonators

If we create open or closed boundary conditions on the transmission line, which has a characteristic impedance and allows wave propagation of light over a distance, then our intuition should lead us to conclude that the eigenmode solutions we find should look like standing waves with node/anti-nodes fixed at the ends. Let's proceed to show this is true.

From above, we know the input impedance of a transmission line with an arbitrarily connected load Z_L - restricting it to behave as either an open ($Z_L \to \infty$ or short $Z_L \to 0$) reduces the expression to:

$$Z_{short} = Z_0 \tanh \gamma l$$

$$Z_{open} = Z_0 \coth \gamma l$$

In this work we solely use capacitively coupled elements - which are effectively open boundary conditions. Both boundary conditions have two eigenmode solution types - $\lambda/2$ and $\lambda/4$ modes where $\lambda/2$ modes produce symmetric nodes / anti-nodes and $\lambda/4$ produce modes with a node and anti-node at either end. We make use of $\lambda/2$ modes on the capacitively coupled open boundary conditions - as the eigenmode solutions produce large electric fields at the boundary allowing larger capacitive couplings.

The input impedance for an open boundary at $\lambda/2$ is

$$Z_{in} = Z_0 \frac{1 + j \tan \beta l \tanh \alpha l}{\tanh \alpha l + j \tan \beta l}$$

in the lossless case $G = R = \alpha = 0$ this expression becomes

$$Z_{in} = -j Z_0 \cot \beta l$$

Resonances occur when $l = n\lambda/2$, and we will have poles in the above expression when

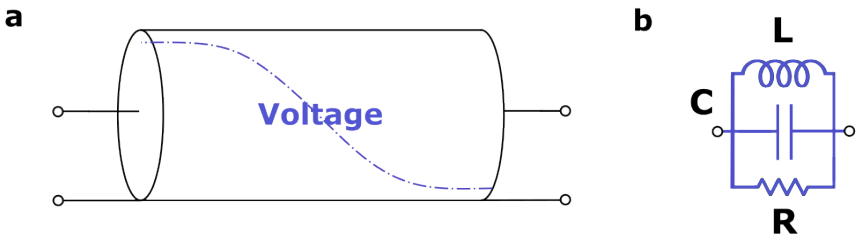

Figure 2.4: **Transmission Line Resonator**. **a** The open-ended transmission line creates boundary conditions, and therefore standing wave solutions to the transmission line equations. The lowest eigenmode, with voltage anti-nodes, is depicted here. **b** Each of these solutions can be locally approximated with an equivalent lumped-element model.

$\beta l \sim (n+1)\pi/\beta$. At $\omega = \omega_{\lambda_2} + \delta\omega \sim \omega_{\lambda/2}$:

$$\beta l = \frac{n\omega_{\lambda/2} + \delta\omega}{\omega_{\lambda/2}}$$

Assuming a small loss term we can expand the above expression:

$$Z_{in} = \frac{Z_0/\alpha l}{1 + j(\pi\Delta\omega/\alpha l\omega_{\lambda/2})}$$

The impedance of the lumped element parallel resonator is

$$Z_{LCR} = \left(j\omega C + \frac{1}{j\omega L} + \frac{1}{R}\right)^{-1}$$

We can expand the above about frequencies near resonance: $\Delta\omega = \omega - \omega_{res}$, giving us:

$$Z_{LCR} = \frac{R}{1 + 2JQ\Delta\omega/\omega_{res}}$$

The above form of the lumped element parallel LCR resonator impedance is quite similar to the input impedance expression for our simplified model of the open transmission line. We can use this similarity to map the lumped element model parameters to the transmission

line parameters, giving us:

$$\omega_n = n\omega_{\lambda_2}$$

$$R = \frac{Z_0}{\alpha l}$$

$$C_n = \frac{\pi}{2Z_0 n\omega_{\lambda/2}}$$

$$L_n = \frac{1}{\omega_n^2 C_n} = \frac{2Z_0}{\pi n^2 \omega_{\lambda/2}}$$

The Q factor of the lumped element resonator $Q_{LCR} = \omega RC$, so

$$Q_n = \omega_{\lambda/2} RC = \frac{\beta}{2\alpha}$$

2.4 The Coplanar Waveguide

The transmission line equations above are quite general. In practice we must fabricate circuit elements in the microwave regime by depositing and removing a thin layer (200nm) of metal (Ta) atop a sapphire chip. This motivates the choice for the transmission line circuit element as the Coplanar Waveguide (CPW) [41] - a compressed 2D version of a coaxial line. A flat center pin carries the propagating signal while the metal plane on either side, separated by the insulated gap, are grounded. Other geometries, such as a balanced version of this design (CPS) or the microstrip can also be used to create transmission lines in this fabricated format. A drawback of the latter design is the ground plane existing at the edge of the dielectric, drawing the field of the mode through the lossy dielectric in contrast to CPW architectures where the nearby ground plane constrains the field propagation and helps isolation. Additionally using the CPW geometry we can easily vary the impedance by varying the ratio of the pin (p) to gap (s) sizes and vary the size of the waveguide without changing the impedance to interface with different circuit elements.

In the limit of infinite thickness for the dielectric substrate ($h \to \infty$) The impedance of

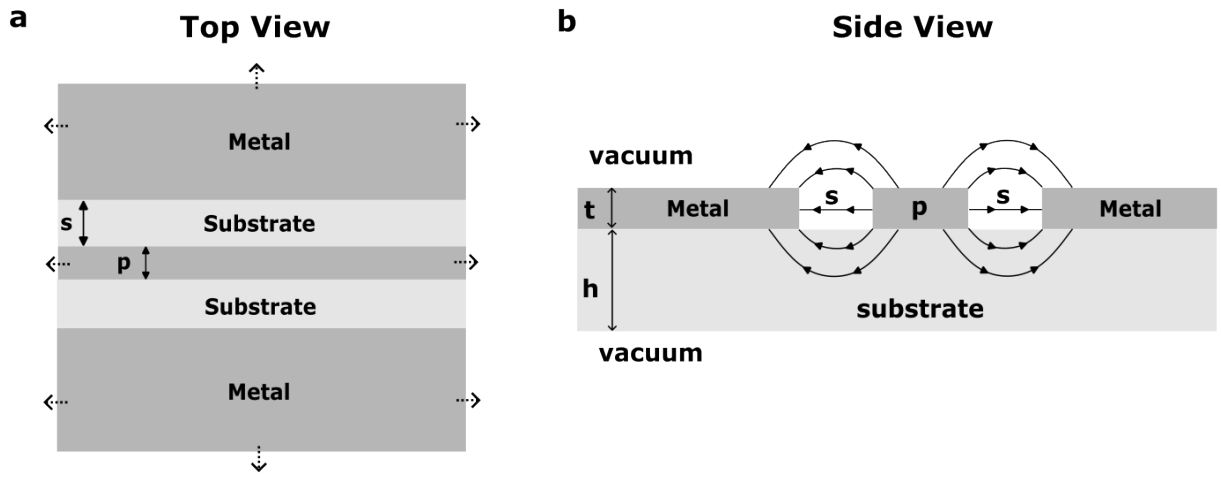

Figure 2.5: **Coplanar Waveguide**. **a** Top view of the CPW transmission line geometry. This 2D circuit is widely used to propogate signals on chips, both in superconducting and room temperature applications. Ground planes extend out from either side of an electrically gapped pin. The impedance is set by the leftover length scales: the ratio of the pin length (p) and gap length (s), in addition to the dielectric properties this circuit is printed on and the metal this is made of. **b** Side view of the geometry, not to scale, showing a few electric field lines to get a sense for the mode profile. In our sample the top Tantalum metal layer is 200nm thick, while the Sapphire substrate layer is 450μm thick.

the CPW transmission line can be analytically solved as:

$$Z_0 = \frac{30\pi}{\sqrt{\epsilon_{eff}}} \frac{K(k_0')}{K(k_0)}$$

where

$$k_0 = \frac{p}{p+2s}$$

$$k_0' = \sqrt{1-k_0^2}$$

and the effective dielectric seen by the mode is

$$\epsilon_{eff} = \frac{\epsilon_{sub}+1}{2}$$

For a sapphire substrate with $\epsilon_r = 11.5$, if we can keep the gap width twice the pin width

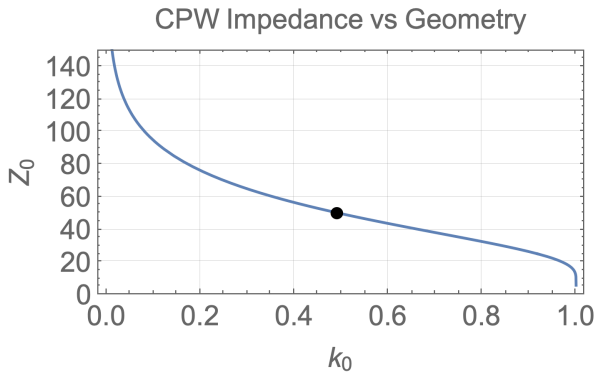

Figure 2.6: **Coplanar Waveguide Impedance**. by adjusting the pin-to-gap size ratio $k_0 = \frac{p}{p+2s}$ the impedance of the waveguide can be tuned (dot indicates $k_0 = \frac{1}{2} \rightarrow Z_0 = 50\Omega$ for our setup), or k_0 held constant while the waveguide increases or decreases in absolute size.

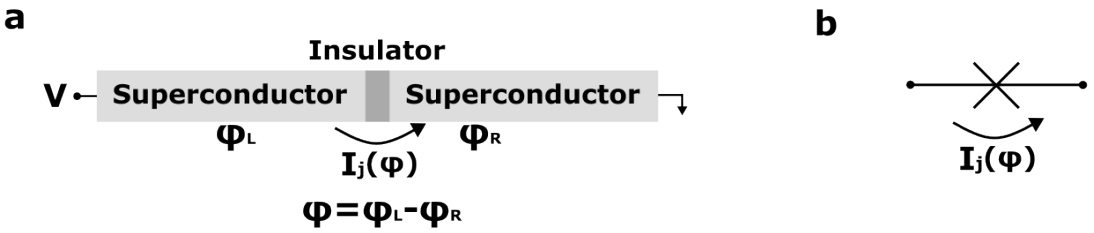

Figure 2.7: **Josephson Junction**. **a** A depiction of the SIS Josephson junction, formed by an Insulating tunnel barrier between two Superconducting electrodes. The difference in the superconducting phases, ϕ, is the gauge-invariant term that plays a physical role in the Josephson equations - determining the dynamics of this circuit element. **b** The symbol of the Josephson junction as a circuit element.

$s = 2p$ then $k_0 = 0.5$ and $Z_0 \approx 50\Omega$. This allows continuous impedance matching while tapering the physical size of the transmission line.

2.5 Josephson Junction

To create qubits out of microwave light, we need a circuit element that creates a strong non-dissipative and non-linear interaction between them. This can be done using the Josephson effect, and a simple element that does this is called the Josephson Junction (JJ) [42, 43].

The SIS Josephson Junction (Fig. 2.7) is a stack of superconducting, insulating, and

superconducting material. The insulating segment allows tunneling of the macroscopic wavefunction of the cooper pairs of electrons, and thus the phase term between the two superconductors differs. The Josephson equations that govern the electrical properties of the junction are [38]:

$$I(t) = I_c \sin(\phi(t))$$

$$\frac{\partial \phi(t)}{\partial t} = \frac{2eV(t)}{\hbar}$$

The current and voltage $(I(t), V(t))$ across the junction are sensitive to the phase difference across $(\phi(t))$ the junction.

If we define

$$\Phi_0 \equiv \frac{h}{2e},$$

$$\Phi \equiv \Phi_0 \frac{\phi}{2\pi}$$

then

$$V = \frac{\hbar}{2e}\frac{\partial \phi}{\partial t} = \frac{d\Phi}{dt}$$

The voltage now cleanly expresses the kinetic inductance - the energy associated with the motion of cooper pairs across the junction.

2.5.1 Josephson Inductance

We tend to think of this circuit element as a strong non-linear inductance when composing larger circuits and qubits using it as an element. To see this, we can use the above Josephson equations to understand the inductive properties of the junction. Taking the derivative of the current relation, we see:

$$\frac{\partial I(t)}{\partial t} = I_c \cos(\phi(t)) \frac{2eV(t)}{\hbar} = \frac{V(t) I_c 2\pi}{\Phi_0} \cos(\phi(t))$$

$$V(t) = \left(\frac{\Phi_0}{\cos(\phi(t))2\pi I_c}\right)\frac{\partial I(t)}{\partial t}$$

Recall the relation between the potential energy and current for an inductor: $V = L\partial_t I$. Using this, we define the parameterized inductance above for the Josephson junction:

$$L(\phi(t)) \equiv \frac{\Phi_0}{\cos(\phi(t))2\pi I_c} = \frac{L_j}{\cos(\phi(t))}$$

and we define the *characteristic* Josephson inductance $L_j \equiv L(0) = \Phi_0/2\pi I_c$.

2.5.2 Josephson energy

When designing qubits the Josephson energy, the energy stored in the junction due to the motion of the cooper pairs, is an important parameter to control. To describe the energy within the junction, we note that the change in the internal energy of the junction must be equal to the work done on the junction:

$$\Delta U = \int_i^f I(t)V(t)dt = \int_i^f I_c \sin(\phi(t))\frac{\Phi_0}{2\pi}\frac{\partial\phi}{\partial t}dt =$$
$$\frac{\Phi_0 I_c}{2\pi}\int_i^f \sin(\phi)d\phi = \frac{-\Phi_0 I_c}{2\pi}\left(\cos(\phi_f) - \cos(\phi_i)\right)$$

So the internal energy of the junction is

$$E(\phi) \equiv \frac{-\Phi_0 I_c}{2\pi}\cos(\phi)$$

and similar to the inductive case, we define a characteristic energy $E_J \equiv E(0) = \Phi_0 I_c/2\pi$ allowing us to write

$$E(\phi) \equiv \frac{-E_J}{\cos(\phi)}$$

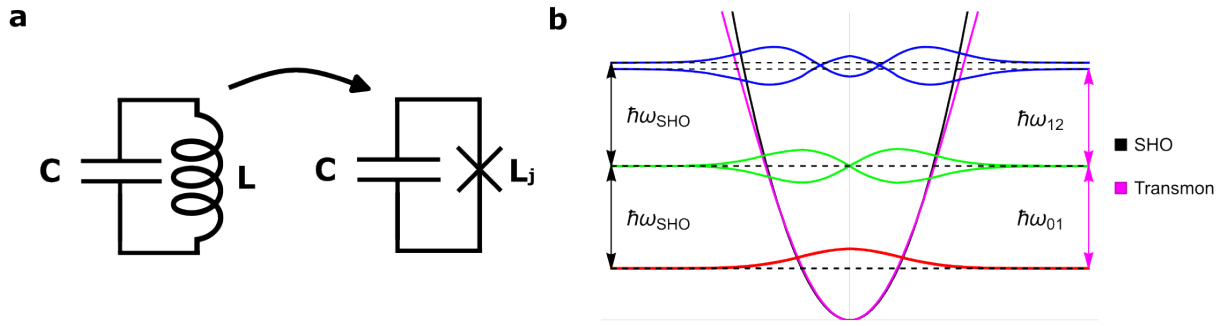

Figure 2.8: **Transmon Qubit created through Josephson inductance**. **a** By replacing the linear inductance in an LC oscillator with the non-linear inductance gained from the Josephson junction element (cross) we obtain a non-linear LC oscillator for microwave light. **b** A toy example of a quantum SHO model with a transmon nonlinear oscillator calibrated for the first transition $\hbar\omega_{10} = \hbar\omega_{SHO} = 1/\sqrt{LC}$. The negative anharmonicity: $\alpha = \hbar\omega_{21} - \hbar\omega_{10}$ of the transmon can be seen as the change in the $|2\rangle$ state energies.

2.6 Transmon

For now, let us discuss the Transmon as the anharmonic LC oscillator formed when the linear inductor of the *harmonic* LC oscillator is replaced with the Josephson junction:

$$H_{transmon} = 4E_c\hat{n}^2 - E_J\cos(\hat{\phi}).$$

By keeping only the quadratic term we have again a simple harmonic oscillator:

$$H_{SHO} = 4E_c\hat{n}^2 - E_J\left(1 - \phi^2/2\right) = \sqrt{8E_cE_j}\left(a^\dagger a + \frac{1}{2}\right)$$

To explicitly continue the series expansion, it is helpful to re-write the second quantized operators $\hat{a}, \hat{a}^\dagger$ in the $\hat{n}, \hat{\phi}$:

$$\hat{\phi} = \frac{1}{\sqrt{2}}\left(\frac{8E_c}{E_J}\right)^{\frac{1}{4}}(\hat{a} + \hat{a}^\dagger)$$

$$\hat{n} = \frac{-i}{\sqrt{2}}\left(\frac{E_c}{8E_J}\right)^{\frac{1}{4}}(\hat{a} - \hat{a}^\dagger)$$

If we place these terms into the expanded $H_{transmon}$ out to fourth order:

$$H_{transmon} \approx \hbar\omega(\hat{a}^\dagger a + \frac{1}{2}) - \frac{E_c}{12}(\hat{a}^\dagger + \hat{a})^4$$

Thus, to leading order the transmon non-linearity is sensitive only to the charging energy. If we look at the perturbed shift of the energy eigenstate levels due to the adding this quartic term:

$$\Delta E_n = \langle n| \left(\frac{-E_c}{12}\right) (\hat{a}^\dagger + \hat{a})^4 |n\rangle$$

$$\Delta E_n = \frac{-E_c}{12}(6n^2 + 6n + 3)$$

So the eigenstate energies including the quartic term for the transmon are

$$E_n = \hbar\omega \left(n + \frac{1}{2}\right) + \frac{-E_c}{12}(6n^2 + 6n + 3) = \sqrt{8E_cE_j} \left(n + \frac{1}{2}\right) + \frac{-E_c}{12}(6n^2 + 6n + 3)$$

2.6.1 SQUID

The ability to generate interactions between photons is critical to making a platform for synthetic materials out of light. However, practical experimental concerns soon arise once we imagine actually using these elements. What happens to our experiment when we create an array of non-linear oscillators, but there is undesired disorder in the frequency? To add the flexibility of *tuning* the energy of the qubits, we add a Superconducting Quantum Interference Device (SQUID), depicted in Fig. 2.9. The idea is to add another Josephson junction in parallel, creating a junction term to the Hamiltonian with two degrees of freedom:

$$H_J = E_{JL} \cos\phi_L + E_{JR} \cos\phi_R$$

Through flux quantization of the loop [44] it is possible to re-express the above as

$$H_J = (E_{JL} + E_{JR}) \cos \pi \frac{\Phi}{\Phi_0} \cos \phi (E_{JL} - E_{JR}) \sin \pi \frac{\Phi}{\Phi_0} \sin \phi$$

Defining the sum and difference of the junction energies as

$$E_{J\Sigma} = (E_{JL} + E_{JR})$$

$$d = \frac{(E_{JL} - E_{JR})}{E_{J\Sigma}}$$

the asymmetric SQUID loop Hamiltonian term can be written as

$$H_J = -E_{J\Sigma} \cos \left(\frac{\pi \Phi}{\Phi_0} \right) \sqrt{1 + \left(d \tan \left(\pi \frac{\Phi}{\Phi_0} \right) \right)^2} \cos (\phi - \phi_0)$$

The transmon qubit lives in-between the perfect two-level system and the harmonic oscillator as an anharmonic oscillator. It is often characterized by it's *anharmonicity* α - the degree to which the level structure deviates from an ideal harmonic oscillator: $\alpha = E_{21} - E_{10}$. For a perfect harmonic oscillator $\alpha = 0$, and for a two-level system $\alpha \to \infty$. A system with sufficient anharmonicity to push the $|2\rangle$ state out of any accessible physics is effectively a two-level system. For the physics we will focus on later we will show that the anharmonicities we achieve, roughly -230 MHz, put us well into the two-level system limit.

2.7 Qubit - Resonator Coupling

One of the most important foundations of circuit QED is the qubit-resonator coupling scheme. In general this is often presented in the context of a generic two-level system interacting with a simple harmonic system - the canonical Jaynes-Cummings model [45] (Fig. 2.10)

The Hamiltonian of the qubit-resonator system can be broken into the form

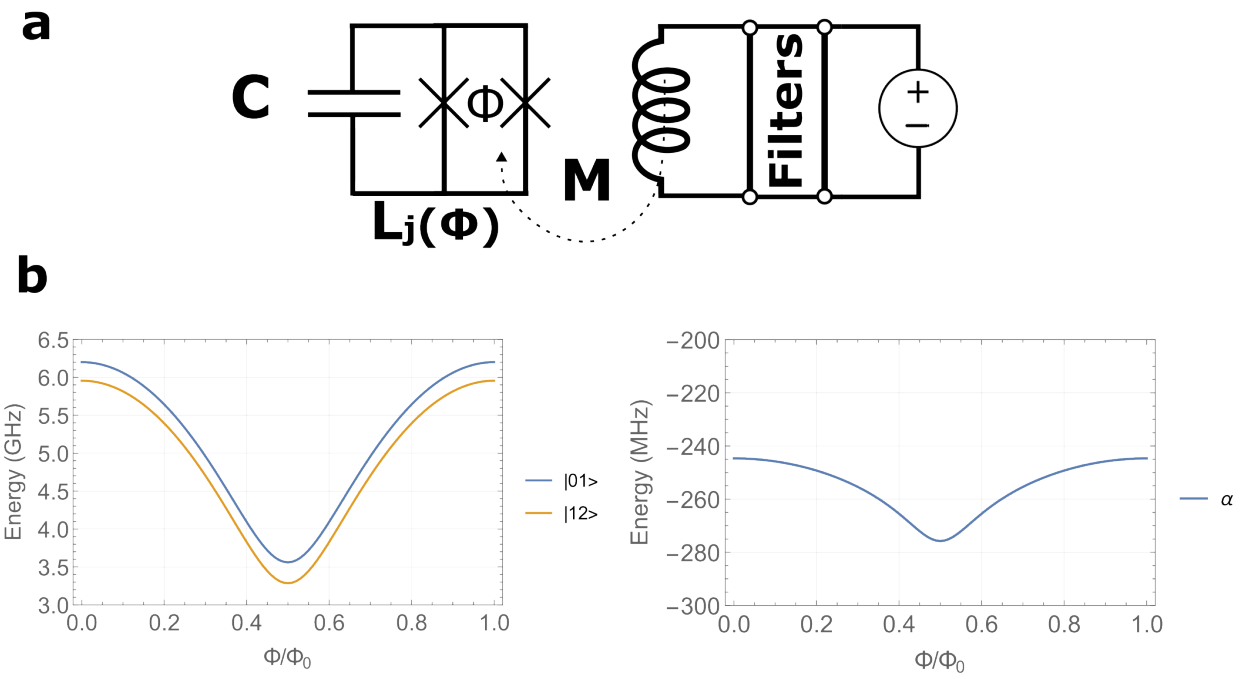

Figure 2.9: **Flux Tunable Transmon**. **a** By breaking the single Josephson junction element into two separate junctions, we create a new magnetic-field sensitive $E_J(\Phi)$ due to the constraint imposed by the Aharanov-Bohm effect. The mutual inductance between the flux-loop in the SQUID junction and the flux bias line is **M**. **b** This sensitivity to the magnetic field flux allows us to tune the transmon transition frequencies while keeping the anharmonicity values relatively stable. These plotted values are very close to our experimental operating points.

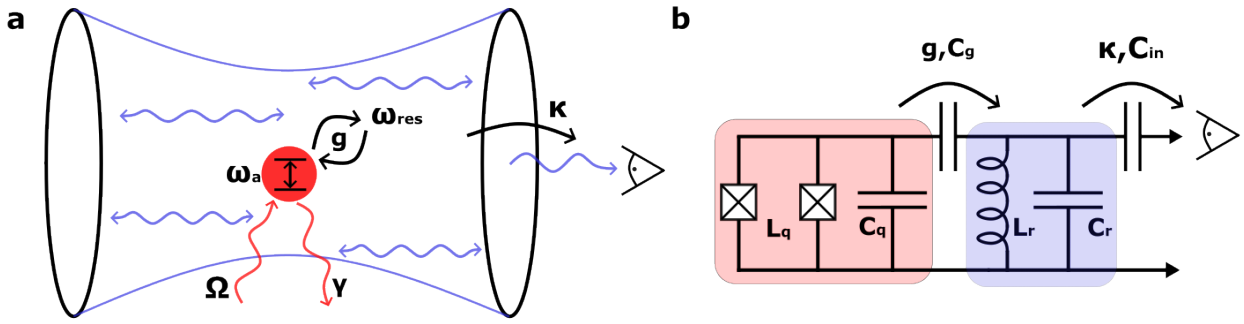

Figure 2.10: **Jaynes Cummings Model**. **a** The Jaynes-Cummings model describes a model wherein a two-level system is dipole-coupled to a harmonic single-mode system. External interactions can be included, such as with the environment via an external drive (Ω) or dissipation (γ, κ) which both push dynamics away from the closed-system description. We use engineered decay of the harmonic oscillator component to perform measurements. Many physical systems realize this model, here **b** we fabricate a qubit and capacitively couple a harmonic oscillator circuit, producing the same physics.

$$H = H_q + H_r + H_I$$

where, taking the rotating-wave approximation with the interaction term, yields a simplified model:

$$H/\hbar = \omega_a \frac{\sigma_z}{2} + \omega_{res}(a^\dagger a) + g(\sigma^+ a + \sigma^- a^\dagger).$$

In terms of our circuit model parameters, the above $H_q + H_r + H_I$ can be expressed as (see [Appendix A [46]]):

$$H = 4E_C\hat{n}^2 - E_J\cos(\hat{\phi}) + \hbar\omega_r(\hat{a}^\dagger\hat{a} + 1/2) + 2e\beta\hat{V}_r\hat{n}$$

$$H = 4E_C\hat{n}^2 - E_J\cos(\hat{\phi}) + \hbar\omega_r(\hat{a}^\dagger\hat{a} + 1/2) + 2e\beta\hat{V}_{rms}(a^\dagger + a)\hat{n}$$

where $\beta = C_g/(C_\Sigma)$ is the ratio of the capacitive coupling to the total capacitance and $V_{rms} = \sqrt{\hbar\omega_r/2C}$

If we re-express the above using the transmon basis states, we obtain:

$$H = \hbar\sum_i \omega_i|i\rangle\langle i| + \hbar\sum_{i,j} g_{i,j}|i\rangle\langle j|(a + a^\dagger)$$

where the mixing terms between transmon states is given by

$$\hbar g_{i,j} = 2\beta e V_{rms}\langle i|\hat{n}|j\rangle$$

If we express the number operator using the transmon creation and annihilation operators (here $b, b^\dagger$):

$$\hat{n} = -\frac{1}{\sqrt{2}}\left(\frac{E_J}{8E_C}\right)^{1/4}(b - b^\dagger)$$

then

$$\hbar g_{i,j} = \hbar 2\beta e V_{rms} \langle i|\hat{n}j\rangle = \sqrt{2}g \left(\frac{E_J}{8E_C}\right)^{1/4} \langle i|(b - b^\dagger)|j\rangle$$

where g is the coupling strength between the transmon and the resonator: $g = eV_0\beta/\hbar$, $V_0 = \sqrt{\hbar\omega_r/2C}$. If we restrict our vision to transitions between neighboring levels: $|i\rangle \leftrightarrow |i+1\rangle$, we can simplify the expression for the coupling:

$$\hbar g_{i,i+1} = \hbar g \left(\frac{E_J}{8E_C}\right)^{1/4} \sqrt{2(i+1)}$$

We can simplify the total Hamiltonian by keeping only terms that couple nearest-neighbors and using the rotating wave approximation:

$$H = \hbar \sum_i \omega_i |i\rangle\langle i| + \hbar\omega_r \hat{a}^\dagger \hat{a} + \hbar \sum_i g_{i,i+1}(|i\rangle\langle i+1|\hat{a}^\dagger + |i+1\rangle\langle i|\hat{a}).$$

Where the last term almost forms the traditional Jaynes-Cummings Hamiltonian, save our preservation of the multi-level transmon structure (truncation would give us the TLS we expect). We operate the qubit and resonator in the dispersive regime: $g/\Delta << 1$, where $\Delta = \omega_q - \omega_r$. In this limit the interaction between the qubit and the cavity can be eliminated with a canonical transformation (Appendix D in [46]) and if we restrict the Hilbert space to the first excited state the effective renormalized Hamiltonian becomes

$$\tilde{H} = \frac{\hbar}{2}\tilde{\omega}_{01}\hat{\sigma}_z + \hbar\tilde{\omega}_r \hat{a}^\dagger \hat{a} + \hbar\chi\hat{\sigma}_z \hat{a}^\dagger \hat{a}$$

where $\tilde{\omega_{01}} = \omega_{01} + \chi_{01}$, $\tilde{\omega}_r = \omega_r - \chi_{12}/2$, $\chi = \chi_{01} - \chi_{12}/2$

and the partial dispersive shifts

$$\chi_{i,j} = \frac{g_{i,j}^2}{\omega i, j - \omega_r}.$$

We now have an expression for understanding the dynamics between our qubit and it's

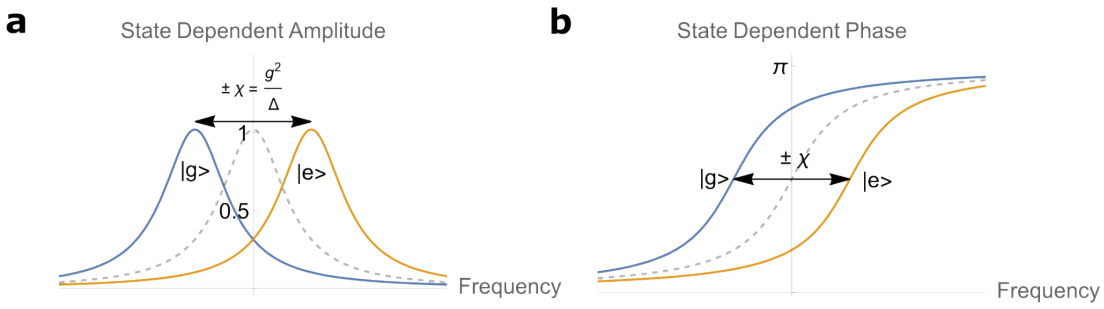

Figure 2.11: **State Dependent Readout**. We show a representation of dispersive readout in the two-level approximation. Probing the cavity transmission in **a** amplitude will produce a shift from low to high power when measuring at the qubit ground state if the qubit becomes excited, whereas measuring at the cavity frequency is excited will result in the cavity transmission decreasing. Measuring in the middle minimizes information in the amplitude, but maximizes informaiton in **b** phase.

dispersively coupled resonator. Our main goal in doing this is to use the resonators as probes to see the state of the qubit. In this form of the Hamiltonian we can make this process abundantly clear - by collecting $H_r + H_I$ we have $(\hbar\tilde{\omega}_r + \hbar\chi\hat{\sigma}_z)\hat{a}^\dagger\hat{a}$, so the resonator energy changes by $\hbar\chi$ based on the qubit occupation.

2.8 Readout and Purcell Filter

The dispersive measurement technique used above is a simple and effective way to measure the state of the qubit. However, with every design choice there are consequences. In this dispersive limit the qubit's hybridized participation in the resonator $|\psi\rangle \approx |q\rangle + \frac{g}{\Delta}|res\rangle$, implies the leakage rate of the population $|\psi|^2$ of the hybridized qubit out through the readout resonator with linewidth κ should present a loss rate, or purcell rate, of

$$\Gamma = \kappa\frac{g^2}{\Delta^2}$$

This loss rate presents conflicting design incentives. Either increasing the qubit-readout coupling or decreasing the detuning (and hence increasing the χ shift) allow increased readout

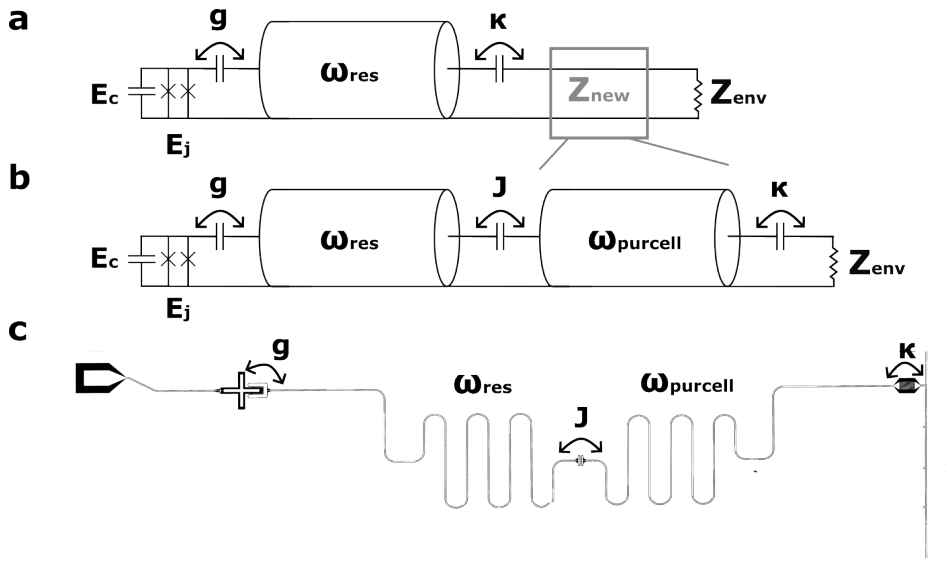

Figure 2.12: **Individual Purcell Filters for Improved Qubit Performance**. In previous work each qubit lattice site was dispersively coupled to a single narrow-linewidth single-pole readout mode, which leaves room for additional purcell filtering **a** by adding an element between the resonator and the environment. We choose to add another $\lambda/2$ resonator on each lattice site **b** and use the lowest eigenmode centered at the readout frequency. The optical image **c** for a single transmon lattice site using this scheme is shown.

speed and fidelity, but increase this purcell loss rate.

Several solutions to this are possible. As part of our experiment we dynamically flux tune our qubits, effectively making $\Delta \to \Delta(t)$, pushing the purcell loss Γ during the experiment down. However this solution exchanges the readout fidelity due to loss during the readout window.

Another route to solving this is to add other circuit elements that change the impedance and increase the qubit lifetime (Fig. 2.12a). Changing the effective decay rate out to the environment in this way is called Purcell filtering. A simple extension on top of the common single-pole readout resonator scheme is to add yet another single pole resonator connected in series between the first resonator and the environment (Fig. 2.12b).

We use a single-pole purcell filter in our work (Fig. 2.12c), where both readout and filter resonators exist as eigenmodes of capacitively coupled $\lambda/2$ coplanar waveguides. By connecting two together in series we are able to create individual filters for each qubit readout

system in our lattice, increasing the speed of readout, enhancing qubit protection against loss, and suppressing crosstalk between lattice sites when driving excitations through the common feedline.

To understand how a purcell filter of this form helps us we can model the field amplitude a, b evolution inside the readout resonator and purcell filter [47]:

$$\dot{a} = -i\Delta_{R,D}a - igb - i\epsilon_r$$

$$\dot{b} = -i\Delta_{F,D}b - iga - \kappa b/2$$

where the detunings between the readout and filter are

$$\Delta_{R,D} = \omega_R - \omega_D$$

$$\Delta_{F,D} = \omega_F - \omega_D$$

By looking at quasistatic solutions for the filter ($\dot{b} = 0$):

$$b = \frac{-ig}{\kappa/2 + i\Delta_{F,D}}a$$

and plugging this result back into the expression for $\dot{a}$, we can isolate a term $-\frac{\kappa_{eff}}{2}a$ where κ_{eff} is real, corresponding to the leakage of a through b as an effective environment:

$$\kappa_{eff} = \frac{4g^2}{\kappa}\frac{1}{1 + (2\Delta_{F,D}/\kappa)^2}$$

Note the the effective loss rate from the readout resonator depends on the drive frequency. When we probe the resonator $\omega_D = \omega_R$. We can consider a photon decaying from the qubit an effective drive at the qubit frequency: $\omega_D = \omega_Q$. If we compare the ratio of these two different leakage rates κ_R, κ_Q respectively:

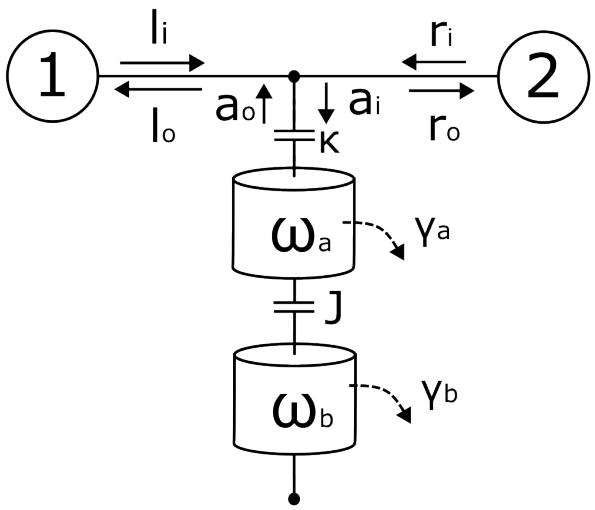

Figure 2.13: **Simplified Model of Purcell Filter**. To extract an analytic model for the scattering amplitude S_{21} of the hanger measurement on our Purcell filter, an input-output model is used to capture the dynamics of the field amplitudes within the readout resonator and the purcell filter.

$$\frac{\kappa_Q}{\kappa_R} = \frac{1 + (2(\omega_F - \omega_R)/\kappa)^2}{1 + (2(\omega_F - \omega_Q)/\kappa)^2}$$

If our design criteria for the filter linewidth is much smaller than the qubit-filter detuning, $\kappa << \omega_F - \omega_Q$, then $\frac{\kappa_Q}{\kappa_R} << 1$ - the effective loss rate for the photon in the readout resonator at the qubit frequency is *much less* than the effective loss for the readout resonator photon at the native resonator frequency.

While the above is a quick method to motivate this design, matching transmission spectra requires a model that captures what we should expect from the scattering parameter S_{21} of such a system. Starting from the hanger model [48] (Fig. 2.13) with purcell and readout mode a, b respectively,

The equations that govern the evolution of the field amplitudes for both resonators are

$$\dot{a} = -i(\omega_a - \omega_d) - \frac{(\kappa_a + \gamma_a)}{2}a - iJb + \sqrt{\kappa_a}a_i$$

$$\dot{b} = -i(\omega_b - \omega_d) - \frac{(\gamma_b)}{2}b - iJa$$

The T junction [41] connecting the filter resonator to the hanger is a symmetric and unitary circuit element that must take the form

$$l_0 = (-1/3)l_i + (2/3)r_i + (2/3)a_0$$

$$r_0 = (2/3)l_i + -(1/3)r_i + (2/3)a_0$$

$$a_i = (2/3)l_i + (2/3)r_i + (-1/3)a_0$$

which, combined with the input-output relations for the filter mode a, we can use to re-express the field amplitude evolution equations as

$$\dot{a} = -i(\omega_a - \omega_d) - \frac{(\kappa_a/2 + \gamma_a)}{2}a - iJb + (\sqrt{\kappa_a}/2)l_i$$

$$\dot{b} = -i(\omega_b - \omega_d) - \frac{(\gamma_b)}{2}b - iJa$$

To extract a scattering amplitude S_{21} from the above we can look at the steady state behavior $\dot{a} = \dot{b} = 0$ of the ratio of the input to output amplitudes r_i/l_o: resulting in

$$S_{21} = 1 - \frac{\kappa(\gamma_b + 2i(\omega_b - \omega_d))}{4J^2 + (\gamma_a + 2i(\omega_a - \omega_d) + \kappa)(\gamma_b + 2i(\omega_b - \omega_d))}$$

In our experiment each readout-filter system is characterized by fitting the transmission spectra to the analytic form of S_{21}, sometimes with an additional impedance mismatch term added to the hanger to absorb imperfections observed in the transmission measurement.

2.9 Design and Simulation

We want to realize a Bose-Hubbard Hamiltonian 2.9 fabricated out of a lattice of individual transmon qubit lattice sites. Additionally, we require each lattice site to be flux-tunable and have a purcell-filtered readout resonator. The two major microwave components we need are the Coplanar Waveguide (CPW) and the Transmon qubit, here manufactured with a Superconducting Quantum Interference Device (SQUID).

$$H/\hbar = -J \sum_{\langle i,j \rangle} a_i^\dagger a_j + \frac{U}{2} \sum_i n_i \left(n_i - 1\right) + \sum_i (\omega_0 + \delta_i) n_i.$$

To start, we will work on creating the circuit elements needed for a single lattice site:

2.9.1 Single Qubit Design

To allow our sample the flexibility of each transmon qubit having tunable frequencies, we print each junction as a SQUID loop. In the design phase for creating $\omega(\phi)$, we create all qubits symmetrically and shoot for a bandwidth of 2 GHz below the readout resonator frequencies to allow room for different simulation experiments we wish to perform with this sample in the future. As E_c controls the anharmonicity, we control the frequency $\omega(\phi)$ with E_j and the asymmetry parameter d. Fixing the upper and lower frequencies $\omega_{min}, \omega_{max}$ gives us constraints for the asymmetric parameter d and the sum E_Σ. Using these, and the RA product from prior fabricated junctions, we can back out the needed junction areas to print E_{j1}, E_{j2} and create upper and lower bounds on the frequencies for each tuning range.

Our optical lithography geometry for flux coupling to the SQUID loop is very similar to our prior work [37] with a measured measured mutual inductance of 0.15pH between each qubit's flux line and the SQUID loop. Loss from the qubit coupling out to the flux line is numerically simulated in HFSS using the circuit quantization black-box technique [49]. We find the estimated purcell loss for our geometry to be $\backsim$ ms, and is thus not a significant

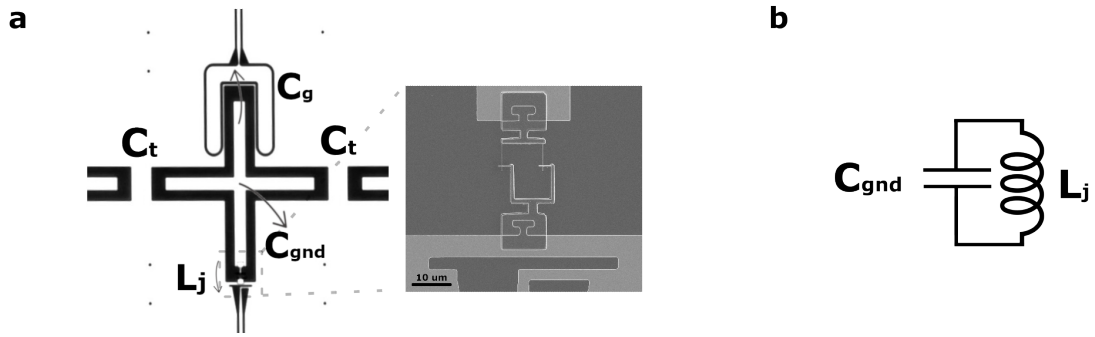

Figure 2.14: **Deign of Single Qubit Parameters**. **a** Our "Single qubit", a transmon with linear capacitance to ground C_g and nonlinear Josephson inductance L_J lies in the middle of a chain - which in this context includes parasitic capacitive coupling to a readout resonator and nearest-neighbor qubits. **b** Initial designs and simulations of a single qubit (which we approximate to a Q.S.H.O. for linear analysis in HFSS) may neglect these parasitic effects by restriction to a single site.

factor in our system.

We also reproduced a similar junction area from the same prior work to reproduce minimal additional coupling due to external flux noise. Performing noise spectroscopy [50] we measure an external $1/f$ flux noise amplitude $\sqrt{A_\phi}$ of $4\mu\phi_0$ for the pure dephasing rate Γ_ϕ of the qubit.

Our real-space design of the transmon qubit must take into account the engineering requirements for the qubit to couple to a readout resonator, to couple to (at most) two neighboring qubits, and to have a SQUID element tuned with a close-proximity flux bias line. In total, four nearby circuit elements motivate a co-planar cross-geometry with four protruding legs, commonly referred to as an "xmon" [51, 52, 53], which we show optically in Fig. 2.14.

This cross geometry generates coupling to neighboring circuit elements via capacitive coupling, but the self-capacitance to ground gives us our E_c term, which we have seen controls the majority of the nonlinearity of the transmon α.

We simulate C_g, and therefore E_C, using Ansys Q3D, a quasi-static Electromagnetic field solver, with the boundary conditions of our experiment (sapphire substrate, vacuum

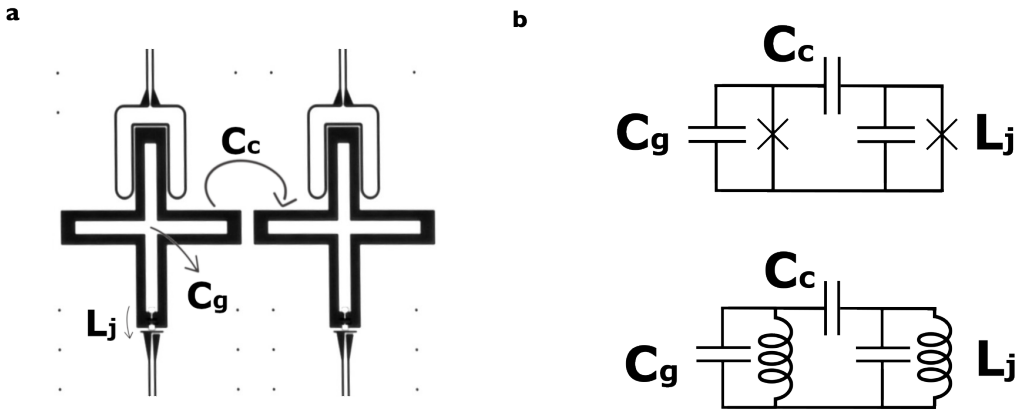

Figure 2.15: **Bose Hubbard Tunneling Term - Capacitive Coupling**. **a** We create the tunneling term through nearest-neighbor capacitive coupling of the transmon qubits. **b** The lumped element model of two qubits describing this interaction (neglecting parasitic couplings from the readout resonator, flux lines). **c** We estimate the coupling strength before fabrication reducing the model to a pair of S.H.O.'s

boundary, superconducting metal and wirebonds). The adaptive mesh iteratively solves the capacitance matrix until a threshold, usually a minimum in percent change of a designated observable, is achieved. In this case, our $C_\Sigma = C_g + C_j \approx 74fF$, so $E_c = \frac{e^2}{2C_\Sigma} \approx 238$MHz value isn't a mission-critical value - our goal in the following experiments here is to produce a synthetic material that satisfies the strongly interacting boson regime $|\alpha| >> |t|$. By fabricating identical transmons we also intend to minimize disorder in both the anharmonicity and the tunneling rate.

2.9.2 Tunneling

The first term $J\sum_{\langle i,j\rangle} a_i^\dagger a_j$ describes tunneling of excitations between neighboring lattice sites. It is also possible to use the Josephson element to create a new tunable inductive coupling circuit (the gmon [54]) allowing independent control over J in magnitude and sign. Briefly, by allowing coupling through an engineered waveguide, directional coupling and topological dynamics can be produced as well [55]. However, these require increasing the

circuit complexity and are potential future directions to improve the flexibility of the sample.

Here we construct nearest-neighbor tunneling in a straightforward manner: neighboring transmon qubits are capacitively coupled through their proximity. The effective overlap in the electric field of the localized excitations for each qubit give a cross-capacitive coupling C_c, while the transmon qubit frequency is dominated by the shunt capacitive coupling to ground C_g and the Josephson inductance L_j. The optical image for our design is shown in Fig. 2.15a - along with the trailing circuit elements for readout and flux tuning for both qubits. To tune a specific coupling, in our model we aim for 10 MHz, we use the coupling model of the linearized lumped element model of this system (Fig. 2.15c). The coupling is equal to the splitting in frequency of the two harmonic oscillators, which simplifies further on the assumption of both having the same L, C values:

$$g = \frac{C_c}{\sqrt{C_{g1}C_{g2}}}\sqrt{\omega_1\omega_2} = \frac{C_c}{C_g^2 L}$$

Detuning between the resonators will shift the effective tunneling, a property we will make extensive use of in the main results.

2.9.3 Readout and Purcell filter

In designing the dual-resonator readout and purcell filter system, we have a few criteria to keep in mind. We require a purcell limit of $>$ 100us at the readout position, and $>$ 1ms in the operating range of qubit frequencies. Additionally, we design the Purcell filter with increased readout resonator speed $1/2\kappa_r \approx$ 100's ns. As all circuit elements, including the filters, are connected to the common transmission line the center frequencies and spacing between are set by the filter bandwidth.

The degrees of freedom we have using this model are the strength of the capacitive couplings between each element: the qubit-readout C_g, readout-filter C_J, and filter-transmission

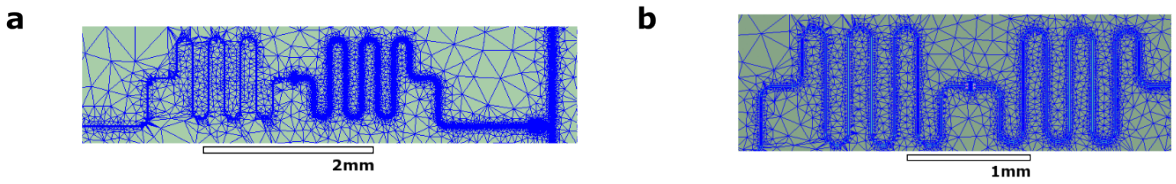

Figure 2.16: **Numerical Simulation of Purcell Filter**. When simulating the real-space geometry of the coupled coplanar waveguide model, different numerical techniques can produce different results. **a** Within HFSS the DrivenModal simulation run on the input/output transmission line ports replicate the S21 experiment and refine the mesh based on the difference in the scattering matrix. However, the narrow readout resonator mode is not sampled well on refinement with this technique (without guiding), leading to an asymmetry in total mesh resolution and poor convergence. **b** By sampling eigenmodes of the total system we do not bias against the real-space distribution of power from the feedline and evenly sample both resonance structures, leading to faster convergence.

line C_κ capacitances. The frequencies and linewidths of the readout and purcell filter frequencies are incorporated as disorder and folded into the parameter $\Delta_{rr,pf}$.

Our parameters roughly match the sample created in [48]. In our used sample $C_g = 3fF$, $C_\kappa = 60fF$,and $C_J = 6fF$, creating a wide-bandwidth ($\approx$ 60MHz) purcell filter. However, rather than a directly ($\Delta_{rr,pf} = 0$) hybridized readout mode, our used sample has fabrication disorder ($\Delta_{rr,pf} \approx$ 60MHz) causing the linewidth κ_r to decrease and the readout ring-up time $1/\kappa_r$ to increase to the μs scale, making frequency multiplexing for scaling up simultaneous readout a more likely option than time-multiplexing going forward. As the vast majority of the design criteria we need were met (purcell filter profile vs frequency, purcell linewidth, purcell center frequencies etc.) we proceed with this sample.

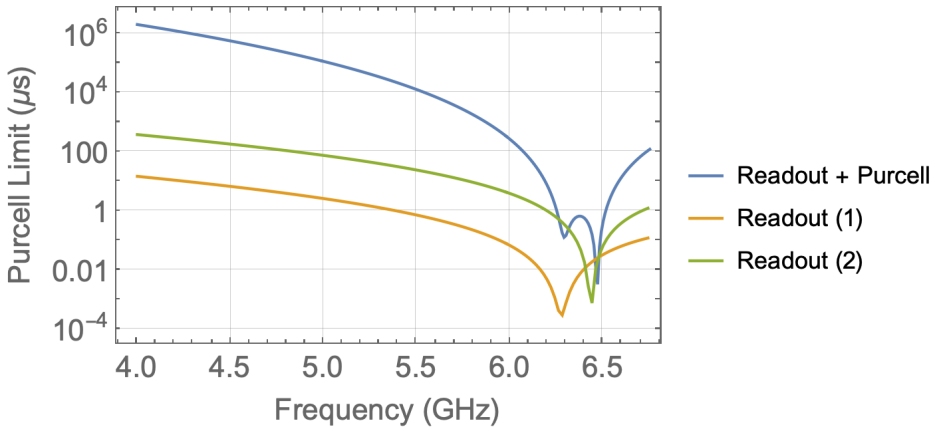

Figure 2.17: **Purcell Filter Design**. The Purcell filter shapes the coupling to the environment, and hence the Purcell loss [1] $T_1 = C_q/Re(Y(\omega))$ for the qubit. The designed loss rate $>$ 1ms for the expermentally operating range $<$ 5.5GHz for the full circuit, and we show the loss rates for the (1) purcell and (2) readout resonator as a reference.

CHAPTER 3

MANUFACTURING

3.1 Fabrication

Our lithography is performed in two steps, corresponding to the two different length scales of our design. The first "base" layer is a faster lower-resolution optical lithography process used to fabricate larger features out of Tantalum where dimensions below 1-2μm are not important to the physics. CPW traces, transmon shunt capacitors, and launcher pads are features commonly fabricated at this step. The second step uses electron beam lithography to create the Josephson elements out of Aluminum - allowing spatial resolution down to the $\sim$ nm scale.

3.1.1 Wafer Processing

Our fabrication process starts by processing the substrate we fabricate our sample on. The substrate is a 450μm c-plane 4-inch Crystek sapphire wafer which we anneal at a maximum temperature of 1500°C for two hours. These wafers are then transferred to the Pritzker Nanofabrication Facility (PNF) at the University of Chicago where the rest of the fabrication takes place. The wafers are cleaned using a traditional TAMI solvent step: iterating through Toluene, Acetone, Methanol, and Isopropyl alcohol for 1.5 minutes, cycling through three sonication settings. The wafers are cleaned again using a two step etching process: in Nano-strip at 80°C for ten minutes and in sulfuric acid at 140°C for 10 minutes with DI rinsing and spin-drying steps between.

3.1.2 Optical Layer

Our base metal layer is made of 200nm Tantalum [56] deposited using an AJA ATC 2200 sputterer at 800°C. To etch into the Ta after deposition we spin a protective AZ1718 resist

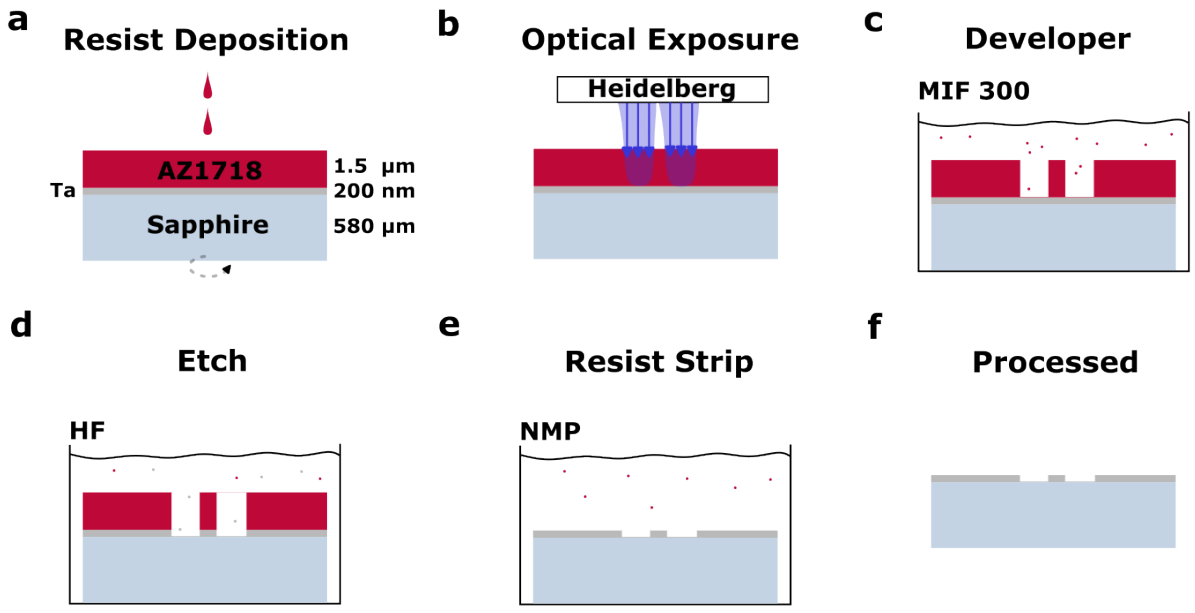

Figure 3.1: **Simplified Optical Fabrication** . **a** After depositing Ta onto the Sapphire substrate, we spin a thin resist layer. **b** By exposing the AZ1718 with an optical-wavelength pattern from the direct writer we create a gradient between polymerized resist and unexposed resist, which is how **c** a difference in developer rate is created, yielding exposed metal underneath our positive photoresist. We **d** etch away this metal with HF and **e** remove the resist covering the rest of the metal, leaving **f** only the etched Ta atop the substrate. Not depicted are detailed cleaning steps, described in the text.

layer on top, soft bake this resist at 95°C for one minute, and optically expose our pre-defined optical layer geometry using a Heidelberg MLA 150 into the resist layer. After exposure we post-bake the resist at 115°C for two minutes and develop the resist for one minute in MIF 300. After rinsing in DI for one minute and spin-drying, the sample is heated in an oven to 120C for ten minutes, then an oxygen plasma asher step is run to de-crust the wafer. The sample is then placed in HF for 19 seconds, then undergoes a DI rinse and is spin-dried. The sample is then sonicated in NMP for 15 minutes, then transferred to a new NMP dish and left at 80°C for four hours. After this time, the wafer is sonicated again at 40°C for two minutes, then transferred to a fresh beaker of NMP at 50°C and sonicted for two minutes again. The wafer is cleaned by sonicating in Acetone and IPA for 1.5 minutes respectively, then rinsed in DI and spin-dried. The wafer is dehydrated for five minutes at 180°C. Optical inspection is performed to benchmark fabrication results.

3.1.3 E-Beam Layer

We apply a bi-layer resist made of MMA EL11 (spun at 4000 RPM, 45 seconds) and PMMA AZ 950 A7 (4000 RPM, 45 seconds) baking each at 180°C for five minutes and cooling the wafer afterwards. Before exposing the resist to the e-beam, we apply a 10nm surface layer of conducting gold using an Angstrom Nextdep thermal evaporator.

After exposing the MMA/PMMA resist layers using the Raith EBPG5000 Plus electron-beam pattern generator, we strip the gold layer using iodine for 45 seconds, DI rinse for 1.5 minutes, and spin dry the wafer. We then develop the resist layers in a 3:1 IPA to DI solution chilled to 6°C for one minute before quickly halting the development process by rinsing with DI and blowing the surface of the wafer with an N2 gun.

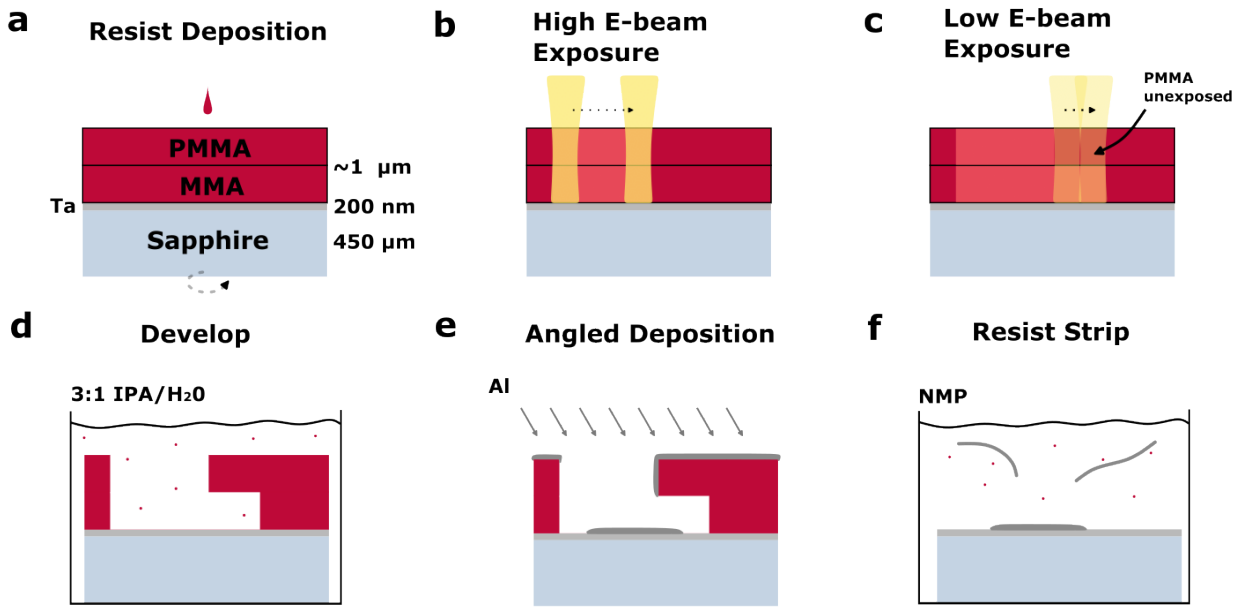

Figure 3.2: **Simplified Ebeam Layer Fabrication** . **a** We spin a dual-layer of MMA/PMMA atop the processed optical layer, which we **b** expose using an electron-beam to directly write the features for the qubit. **c** The MMA layer exposes at a lower power threshold, allowing us to **d** develop the total exposed resist and create undercuts. When we perform angled-deposition of Aluminum **e** to create junctions, these undercuts help break the metal deposition, allowing the **f** liftoff to carry the resist and extra metal off of the surface.

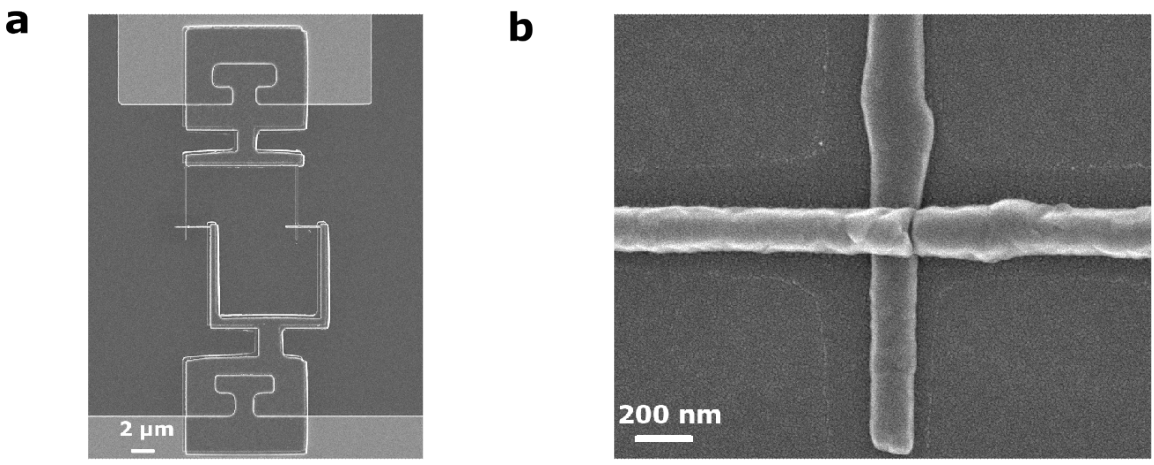

Figure 3.3: **Qubit Fabrication**. We create SIS Josephson junctions using Aluminum atop a Tantalum ground plane. **a** A representative SQUID loop geometry for our sample. The top and bottom square pad features ensure galvanic electrical connection between the Tantalum (light grey) and the Aluminum layers (dark grey) respectively, both of which sit atop the sapphire substrate. The SQUID loop can be seen as the area enclosed by the loop of metal in the middle between both junctions. **b** The Al/AlOx/Al Josephson Junction is formed by evaporating Al in a ballistic trajectory at a shallow angle into the resist pattern at two angles - each forming one of the "fingers" above. After the first deposition an oxide layer is grown to form the barrier, and the overlap between the layers creates the Josephson energy E_J.

3.1.4 Junction Evaporation

The Plassys MEB5500 angled evaporator is, as the name implies, capable of angled evaporation of material on a surface. We take advantage of this to create three successive layers: Aluminum, Aluminum Oxide, and Aluminum to create SIS Josephson Junctions (Fig. 3.3).

After the sample is loaded into the Plassys chamber we pump down for five hours, and run an initial Titanium evaporation step to further decrease the ambient pressures - reaching a starting chamber pressure of $7e^{-8}$Torr and loadlock pressure of $1.9e^{-7}$Torr. Before Al deposition we use an argon ion milling step to etch the surface oxide layer on the sample. We operate the ion milling process at 400kV, and step through three separate angles $\pm 30, 0$ milling for 25 seconds each.

With the oxide removed, the first 60nm Aluminum layer is deposited at a rate of 0.1nm/s.

After this step, the chamber is filled with 50mBar of Oxygen to carefully create a surface layer of Aluminum Oxide - which forms the insulating layer for the SIS junction. We have calibrated this to take 24 minutes at 50mBar for our sample. After rotating the sample in the chamber by 90 degrees, the last layer 150nm of Al is is deposited at a rate of 0.1nm/s.

We add an additional delay step after the last deposition before venting the Plassys, as this is observed to increase Junction fabrication fidelity.

3.1.5 Post-Processing

Before dicing, we apply a surface coating of AZ703 resist and bake for 5 minutes to aid in shielding the wafer during processing under the dicing saw. The wafer is then converted into many individual samples of 10x20mm chips by physically cutting the wafer with a fast-spinning diamond blade actively cooled with water.

Before returning to the lab - each chip is still globally coated in a protective layer of AZ703, Aluminum, and MMA/PMMA resist layers (which ideally all help shield the chips from damage during dicing). To Lift these layers off the chips are: placed in NMP for 4 hours, sprayed down with NMP while transferred to new NMP for two minutes and sonicated, sprayed while transferred to an IPA beaker, sprayed while transferred to an Acetone beaker, then sprayed while transferred to another IPA beaker, then dried with a nitrogen gun.

3.1.6 Resistance Measurements

The Josephson junction element gives our transmon qubits their anharmonicity. The critical current density $J_c = I_c/A$ is, via the Ambegoakar-Baratoff relation:

$$I_c/A = J_c = \frac{\pi\Delta}{2eRA}\tanh\left(\frac{\Delta}{2k_BT}\right) \approx \frac{\pi\Delta}{2eRA}$$

where Δ is the superconducting energy gap, R is the resistance of the gap, and T is the temperature, and we operate in the cryogenic experimental regime $k_b T << \Delta$.

The E_J parameter is, in terms of the critical current density:

$$\frac{E_J}{A} = \frac{\hbar J_C}{2e}$$

so

$$\frac{E_J}{A} = \frac{\hbar \pi \Delta}{(2e)^2 RA}$$

Given Δ is a constant of the Aluminum we are using, the degrees of freedom to control E_J are the area and resistance. We do this by changing the fabrication parameters of exposure on the resist, and change the oxidation parameters to control the thickness of the junction to change the area and resistance respectively.

However, to have the freedom to tune the energy of our qubits we create SQUID loops and we should characterize both junction E_J's - as asymmetries change the flux tuning range of the qubit. In the circuit model these junctions are now in parallel, so measuring the resistance between them becomes difficult if our circuit is the normal fabricated transmon.

We dedicate a portion of our chip to fabricating copies of our transmon qubits with only the left or right junction connected to allow independent resistance probe measurements of the E_{JL} and E_{JR} parameters. As our sample chip also contained witness junctions, the experimentally used sample has witness junctions of $E_J = 4.83(\pm 0.18)$ GHz and $E_J = 14.22(\pm 0.15)$ GHz

3.2 Assembly

We inspect chips for defects under an optical microscope after transporting samples from the nanofabrication facility back to the lab.

First, The sample then placed in a rectangular copper cap with an indium ring seal,

comprising half of an OFHC light-tight enclosure for the 10x20mm chip sample. This copper cap is pressed up to a multi-layer copper PCB containing the signal routing (Fig. 3.4) and mechanically held in place with screws. The copper PCB mediates connections between the circuit elements on the chip and the wiring in the fridge. However, connections between the PCB and the chip must be made.

To suppress slotline modes, enforce microwave boundary conditions, connect signal traces from the package to the chip, and ground the sample we use a manual wirebonder to connect disparate points together with wirebonds (Fig. 3.4). Future samples will likely incorporate air-bridge technology [57] as well. As a practical point in our optical layer the coplanar read-out and purcell resonator bends are too sharp for wirebonding to take place, so those circuit elements in the middle of the chip remain untouched. Once the launchers are wirebonded, an electrical connection between the circuit elements on the chip and the traces within the PCB are made, allowing further elements that are connected to the PCB to interface with our fabricated sample.

We then enclose the sample with a cap and tighten it with brass screws using the second half of the OFHC enclosure. This cap is designed to attach to an additional OFHC copper piece with a coiled Niobium-Titanium wire to create a global solenoid magnetic field for the sample (shown in Fig. 3.4). The PCB and enclosed sample is mounted (via an copper stick) into a multilayered cylindrical shield. Our shielding consists of an outer layer of Mylar, followed by two layers of Mu-metal, a superconducting lead layer, and a thin high purity copper shim which faces the sample [58] (sample can at the bottom in Fig. 3.5).

3.3 Mounting

This can is mounted to the mixing chamber base plate of a BlueFors BF-LD400 dilution refrigerator, where a thermally conducting path along connected OFHC from the mounting brackets to the PCB ensures both reach 8mK with no applied load. This temperature range

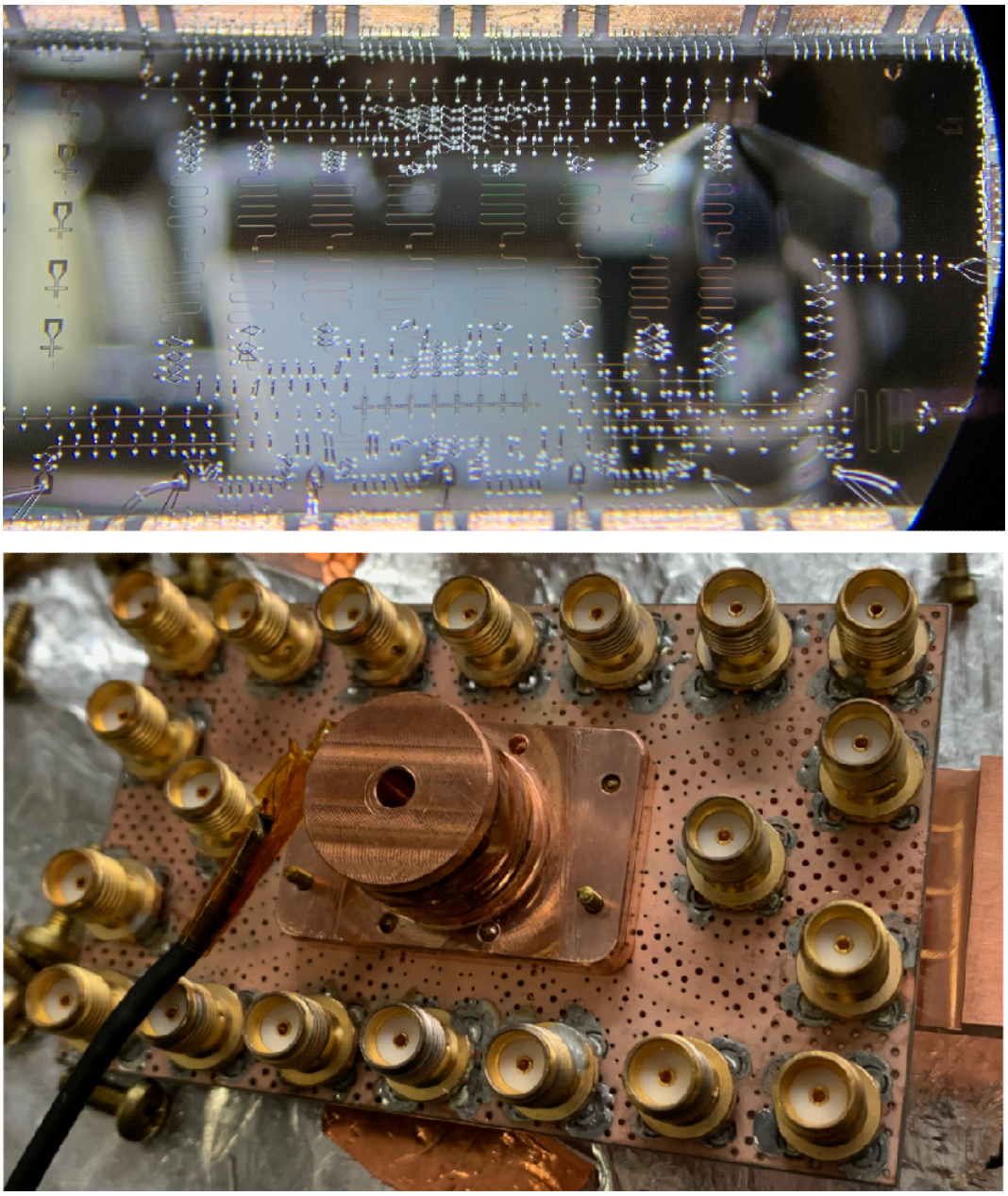

Figure 3.4: **Sample Wirebonding and Mounting**. **Top** The 10x20mm chip is wirebonded with Aluminum wire, grounding accessible CPW traces to prevent radiative coupling and suppress slotline modes. Wirebonds create connections from the mount to the launcher pads, allowing exchange of microwave signals to and from the sample. **Bottom** The sample is enclosed in OFHC within a copper cap, sealed with a ring of indium wire to prevent light-leakage (not seen). The surface-mount SMA connectors mediate microwave signals from the fridge to the sample through the circuit mount. We add a solenoid to generate a local global field seen by all qubits in our lattice.

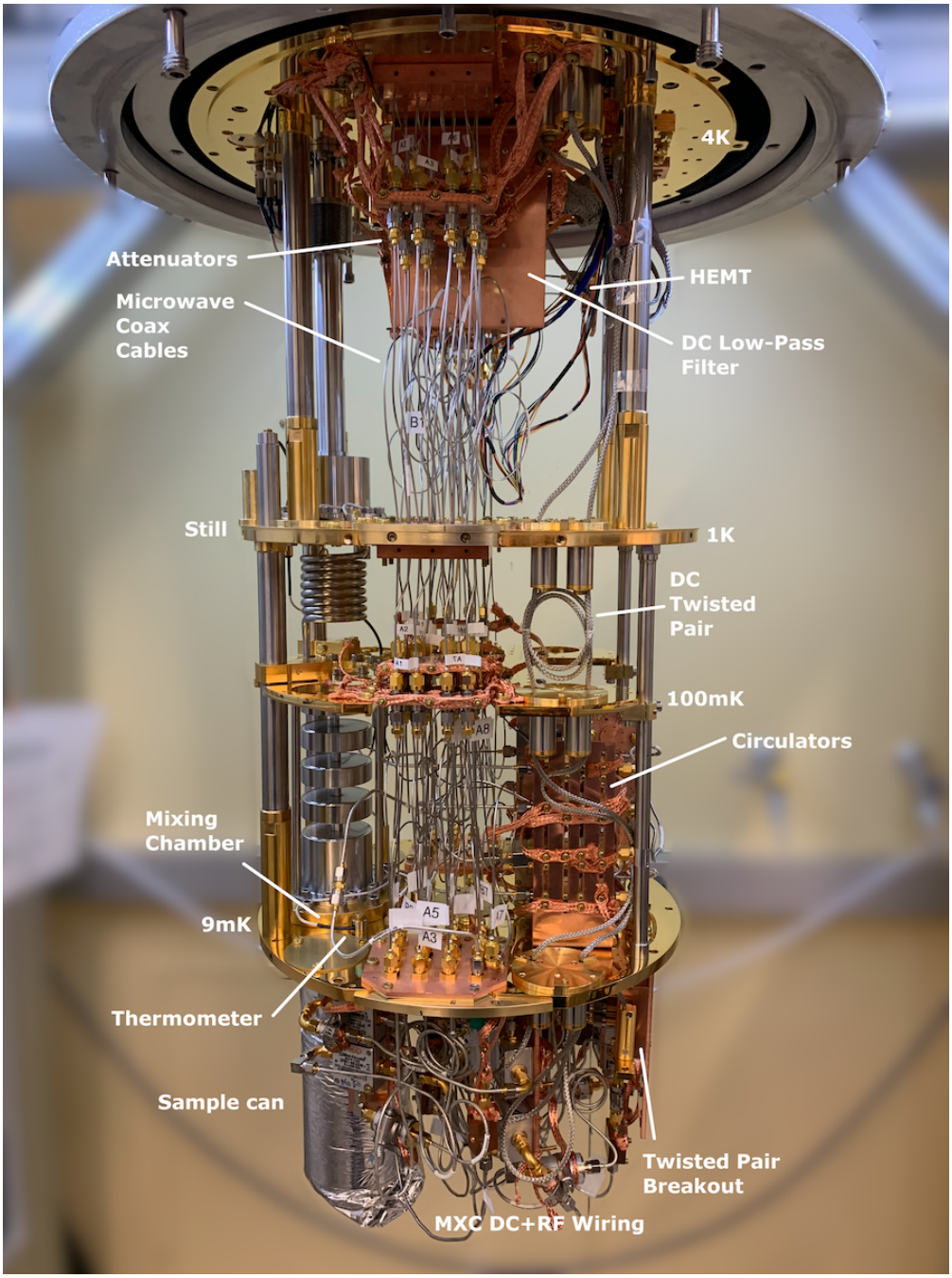

Figure 3.5: **Fridge Assembly**. Our cryogenic wiring inside our BlueFors dilution refrigerator is shown. Microwave compatible coax lines thermalized at 4K, 100mK, and 9mK via fixed attenuators and twisted-pair DC lines send signals to the sample through filters located at 4K and the mixing chamber stage. Signals from the sample are sent through filters, circulators, and a HEMPT amplifier before reaching room temperature.

is important - the superconducting transition temperature of Aluminum $T_c \approx 1$K, placing a hard requirement for the Josephson junction itself to operate at $T < T_c$. However, at the operating range of 4-8GHz we suffer from thermal excitations in the 100's of mK range - forcing the experimental condition that we operate in a regime much colder than this to suppress thermal fluctuations from influencing microwave physics.

3.4 Wiring

As seen on the real-space image of the fridge (Fig. 3.5), fixed attenuators thermalized to different stages of the fridge are used to attenuate the signal as it travels down from room temperature to the sample [59]. Without any filtering, signals sent from the room temperature measurement setup have a background thermal distribution set at room temperature, 300K. This high-temperature blackbody radiation swamps the power of the signal we wish to probe the system with at the mixing chamber stage. As the signal passes through a thermalized attenuator, both the intended signal and the background radiation are attenuated, with the background radiation of the thermalized attenuator at that temperature added in.

The thermal background of photons at room temperature is given by the Bose-Einstein distribution

$$n_{BE}(T,\omega) = \frac{1}{e^{(\frac{\hbar\omega}{k_b T})} - 1}$$

and at each stage the signal passes through a thermalized attenuator the thermal background changes:

$$n_i(T,\omega) = \frac{n_{i-1}(\omega)}{A_i} + \frac{A_i - 1}{A_i} n_{BE}(T_i,\omega).$$

We distribute the dissipative heat load of attenuating the signal at different stages as the signal travels down to the sample. If we examine the wiring diagram (Fig. 3.6) and look at the qubit drive and readout line, the attenuation is spread evenly along the 4K, 100mK, and

mixing chamber (9mK) stages at 20dB of attenuation each. Modeling this attenuation of the 300K thermal distribution using the recursive relation above on the drive line at the center of the readout resonator frequency distributions (6.5GHz), the residual thermal population is $\approx 1/500$ of a photon.

On all input lines to the sample we add IR filtering in the form of a strong eccosorb [60, 61] to protect the sample from radiation at the superconducting gap.

On the flux bias line, responsible for sending both static DC currents and "fast" DC pulses to the SQUID loop junction, we additionally have a 1.8GHz Low-pass filter, then a Bias-Tee. We break the flux biasing into a slow frequency DC component, with aggressive low pass filtering designed to tolerate a constant current load, and a fast frequency AC component with higher cutoff frequency designed for a DC load of 0 Amps. The DC current is sent through a LP filter at 1.9 MHz at the MXC, then converted to twisted pair lines via an custom in-house SMA-dSub PCB thermalized at the MXC. These lines run up to 4K before breaking out to another in-house PCB (thermalized to 4K) where each DC line passes through a two-pole RCRC filter with 7 kHz cutoff frequency before continuing out to room temperature. Each DC line is fed through another RC filter (8 Hz cutoff) with a cut ground plane before connecting to the DC source - an analog devices AD5780 DAC controlled via an Arduino through SPI.

On the "fast" DC side, the bias tee leads signals up through 10,1,and 20 dB of thermalized attenuation at the MXC, still, and 4K stage respectively before reaching room temperature, where the coax lines are wired to the M3102A 1GS/s AWG output ports on the PXI. We add an additional attenuation at room temperature to re-scale the AC voltage (0-20dB), which we have noticed help re-scale the noise amplitude.

The global solenoid is controlled by an external Yokogawa GS 200 supply set to constant current mode. The wiring passes through the same twisted pair lines the AD5780 DC sources do, but the only filtering beyond the self-inductance of the solenoid is at the RCRC filter at

4K.

On the common feedline input and output we have eccosorb and high-frequency low-pass filters from Minicircuits at 9.6GHz to shield the sample. On the input side there is a simple series of 20dB filters at the MXC, still, and 4K stage before we split the input wiring for the two different homodyne setups. On the output side past the IR filtering, we connect in series to two 4-8GHz LNF circulators and one 4-8GHz Quinstar circulator. Our circulators operate normally with a terminator and act as isolators. The output is fed up from the MXC through superconducting Niobium wire to a 4-8GHz LNF HEMT, whose output is fed to room temperature, amplified via a Minicircuits ZX60-832-N-S+ amplifier, then split and feed to two independent homodyne setups.

3.5 Room Temperature

The room temperature dual-homodyne measurement setup that sends and receives signals to the sample, which has taken the vast majority of the data for the experiment presented here, has affectionately been named Gerbert.

3.5.1 Homodyne Detection

Using homodyne detection we look for the shift in amplitude and phase of a single frequency that we monitor. A simple method to do this is digitally generating a microwave tone, sending it down to the sample, and sampling at a similar rate to extract the amplitude and phase shift of that signal. However, we lack the ability to directly digitally synthesize a signal at microwave frequencies such as 6 GHz - the frequency of the readout resonator mode. Instead, we use a Local Oscillator (LO), in our setup a SignalCore SC5511A, whose purpose is to act as a constant high-frequency spectrally pure microwave tone. This operates at a frequency outside of the bandwidth of our other measurement or digital signal generation capability. We send this as input to non-linear IQ mixers which allow us to add (or subtract)

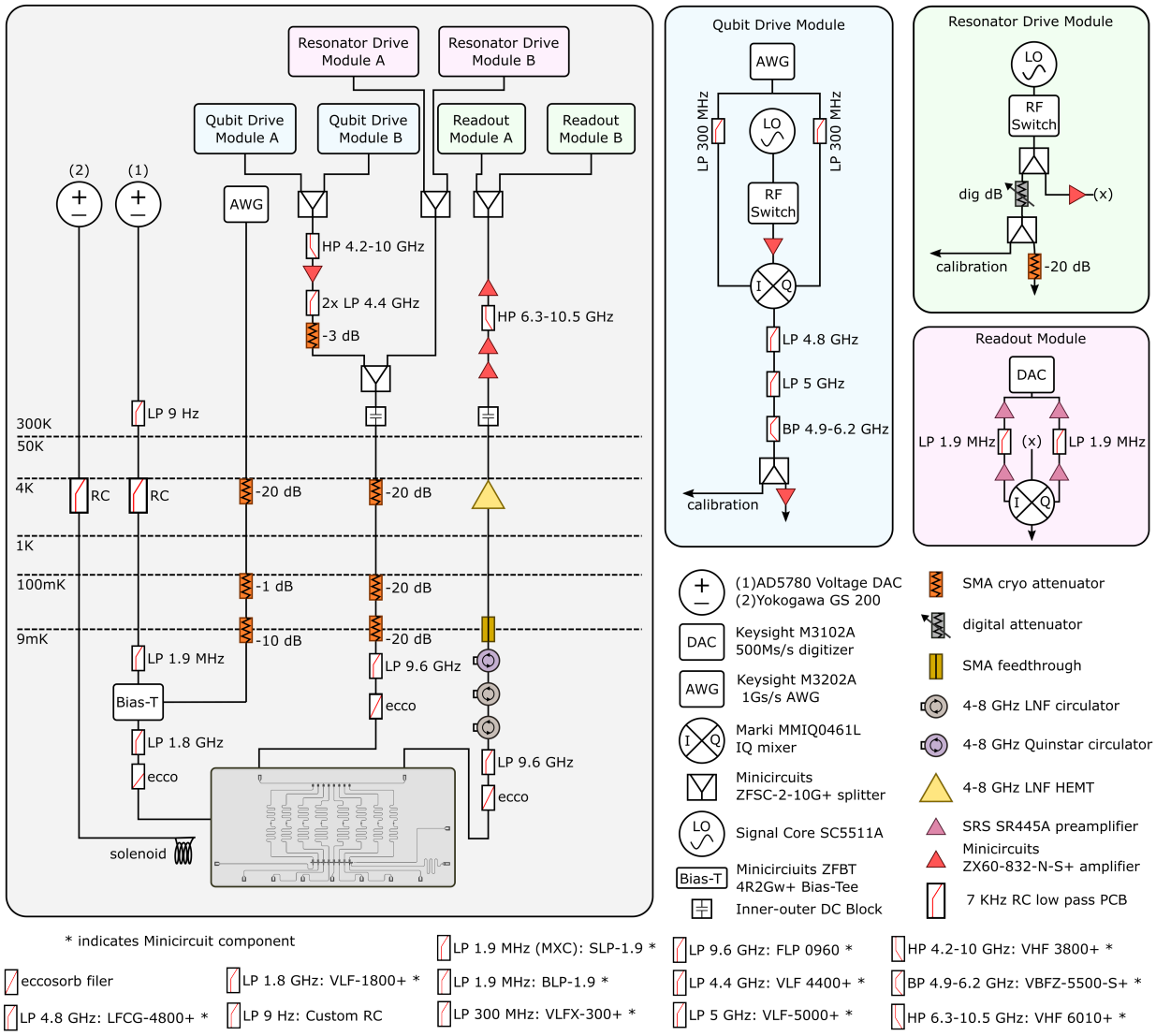

Figure 3.6: **Wiring Diagram Schematic**. Full room temperature and cyrogenic schematic for Microwave and DC signal routing to and from our chip. Homodyne setups probe the state of qubits in our experiment via individually coupled filtered readout resonators through cryogenic compatible microwave lines. Qubits are biased through DC lines, with static DC signals on a low cutoff twisted pair line and "fast" DC signals filtered at a higher cutoff. See [2] Supplementary Figure S1.

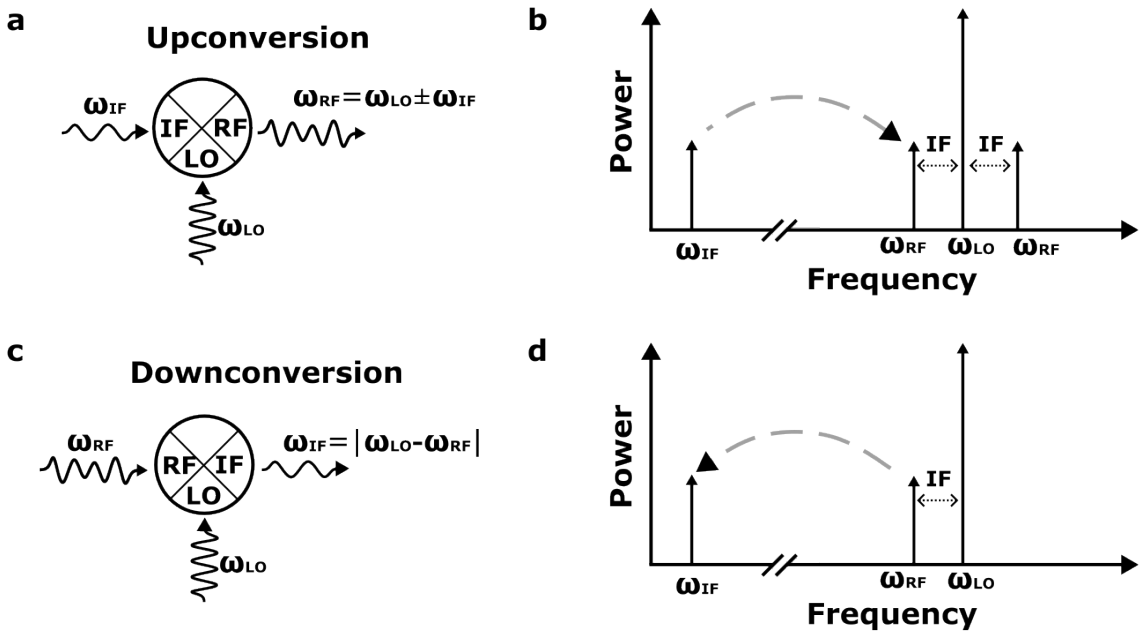

Figure 3.7: **Mixer Up / Down Conversion**. Direct digital synthesis of microwave frequency tones is not achievable with our hardware. We use non-linear microwave mixers and a high-frequency microwave carrier tone (LO) to generate signals to interact with and measure our sample. Up-conversion allows us to generate high-frequency pulses by modulating the LO using an IF frequency. We can measure the distortion of the LO by feeding the measured signal back into the RF port and down-mixing close to DC.

a signal from the LO - respectively up/down conversion.

3.5.2 Mixer

The basic mixer is a three-port device with a Local Oscillator (LO) port, Radio Frequency (RF) port, and an Intermediate Frequency (IF) port. Typically the LO port is driven at an unchanging

$$S_{LO}(t) = A_{LO} \cos \omega_{LO} t$$

To up-convert a signal for interacting with the sample, suppose to probe a readout-resonator, we apply a tone ω_{IF} to the IF port:

$$S_{IF}(t) = A_{IF} \cos \omega_{IF} t$$

An ideal mixer's output combines the signals:

$$S_{RF}(t) = S_{LO}(t) S_{IF}(t) = A_{LO} A_{IF} \cos(\omega_{LO} t) \cos(\omega_{IF} t) =$$

$$\frac{A_{RF}}{2} \cos((\omega_{LO} + \omega_{IF})t) + \cos((\omega_{LO} - \omega_{IF})t)$$

where A_{RF} is $A_{LO} A_{IF}$.

In this case the up-conversion process has sidebands. On either side of the LO frequency, separated by ω_{IF}, our signal appears. In reality, higher harmonics from the non-ideality of the mixer are generated, producing images of the signal at $n \cdot \omega_{IF}$ as well.

For down-conversion, a signal close to ω_{LO} can be sent to the RF port, and low-frequency information will flow out on the IF port. "close" in this case implies that the bandwidth of the ADC or measurement device can handle $\omega_{RF} - \omega_{LO}$.

For simplicity - we will assume the signal sent for down-conversion will be a signle frequency:

$$S_{RF}(t) = A_{RF}(t) \cos(\omega_{RF} t)$$

The LO remains the same:

$$S_{LO}(t) = A_{LO} \cos \omega_{LO} t$$

Again, the ideal mixer combines the signals as:

$$S_{IF}(t) = S_{RF} S_{LO} = A_{RF} A_{LO} \cos(\omega_{RF} t) \cos(\omega_{LO} t) =$$

$$A_{IF} \cos((\omega_{RF} + \omega_{RF})t) \cos((\omega_{RF} - \omega_{RF})t)$$

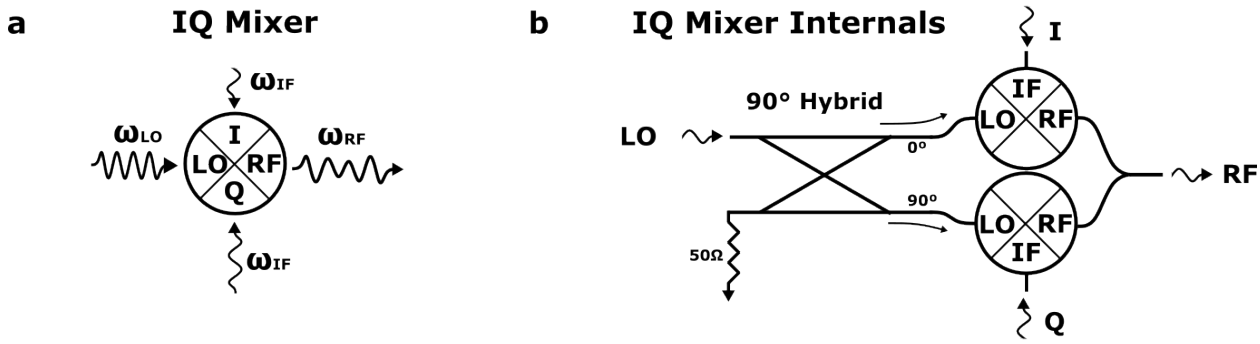

Figure 3.8: **IQ Mixers**. **a** The IQ mixer takes two independent signals I(t), Q(t) rather than a single IF to mix with an LO. **b** The internal structure of an IQ mixer can be understood as a combination of two mixers combined with a phase offset. This allows us to separate the IF input into an in-phase I(t) and an out-of-phase (+90) Q(t) signal for up and down conversion processes.

In our application ω_{RF} and ω_{LO} are either almost equal, or only off by 100's MHz but centered at either the qubit drive (plus a sideband) or the readout frequency, making the high frequency term $(\omega_{LO} + \omega_{RF})$ on the order of 10's of GHz. Thus, the higher sidebands are removed on encountering the high-frequency low-pass filters in our readout setup within the homodyne chain (Fig. 3.6)

In our setup we use IQ mixers, which allow us to drive the quadrature components of the IF port independently.

As shown in Fig. 3.8, the IQ mixer breaks the IF modulation of the LO into quadrature components (I,Q):

$$S_{RF}(t) = I(t)\cos(\omega_{LO}t) + Q(t)\cos(\omega_{LO}t)$$

An advantage of IQ mixing is the destructive interference of sidebands: *Modulating* the I and Q channels at

$$I(t) = A\cos(\omega_{IF}t)$$

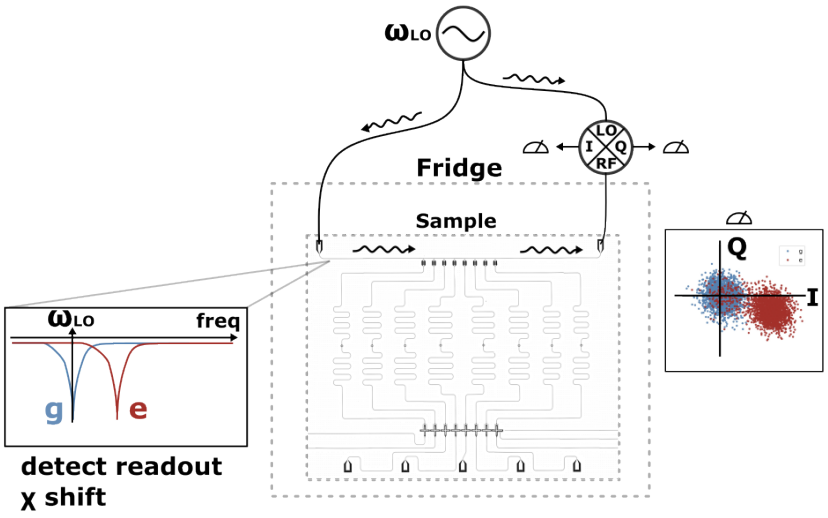

Figure 3.9: **Simplified Qubit Readout Schematic**. We use homodyne detection to probe the state of the qubit through changes to the coupled resonator. A high frequency tone is sent to the resonator, and the state of this resonator is measured by detecting the relative phase and amplitude of this signal from the I and Q channels of the downconverting IQ mixer.

$$Q(t) = A\cos\left(\omega_{IF}t - \pi/2\right)$$

yields:

$$S_{RF}(t) = A(\cos\left(\omega_{IF}t\right)\cos\left(\omega_{LO}t\right) - \sin\left(\omega_{IF}t\right)\cos\left(\omega_{LO}t\right))$$

$$S_{RF}(t) = A\cos\left((\omega_{IF} + \omega_{RF})t\right)$$

For qubit state readout, we apply the readout frequency tone to the sample and the input LO port of the IQ mixer used for down-mixing this signal (Fig. 3.9).

The χ shift of the resonator is probed by looking for the amplitude and phase shift of the signal measured from the time-averaged traces read out on the digitizer taking in down-converted signals from the I and Q channels from the mixer.

In the disordered configuration of our staggered qubit array, each eigenstate is a localized excitation on a qubit at a unique frequency. We use the up-conversion process to drive excitations onto these individual qubits on the common feedline by choosing the sideband

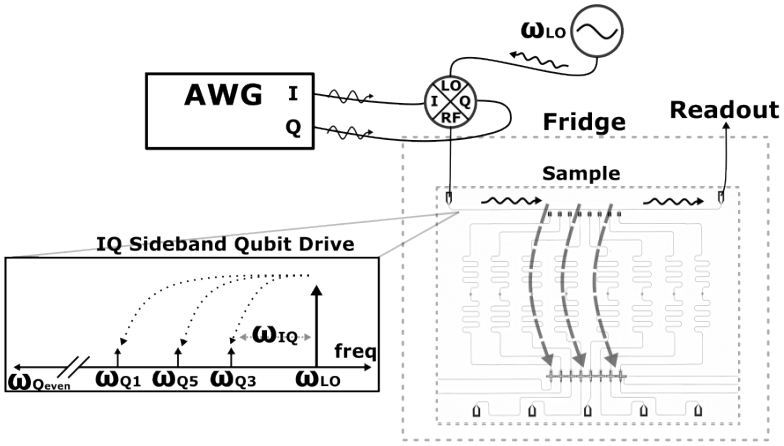

Figure 3.10: **Simplified Qubit Drive Schematic**. We use up-conversion with side-band modulation generated by an AWG pulse-sequencer to drive qubits in the staggered lattice configuration. Charge driving the qubits happens through the common feedline, requiring frequency separation for all qubits to address each one, and microwave hygene to ensure no combination of resonances and sidebands collide during state preparation.

frequency δ_{sdbnd} such that $\omega_{qi} = \delta_{sdbnd} + \omega_{LO}$.

As the nonlinear mixer creates additional sidebands at $\omega_{LO} \pm m \cdot \delta_{sdbnd}$ where $m = 1, 2...$, we position the qubit frequencies and choose the sideband IQ mixing frequencies to maximize the distance between the parasitic sidebands and any other qubit transition in the lattice when driving a transition. Again, this is necessary as we drive transitions through the common feedline, so we require frequency separation to address individual qubits rather than spatial separation and using individual charge drive lines.

CHAPTER 4

CHARACTERIZATION

We perform a series of initial experiments to understand, calibrate, and benchmark the circuit before proceeding to the experiments that constitute the science we seek to study. As a basic example, the fabricated Josephson junction SQUID loops provide upper and lower frequency bounds as a function of applied flux, but without measuring those frequencies, the starting flux, or the current-to-flux ratio we don't have a good handle on manipulating even single qubits in our system.

4.1 Resonator Spectroscopy

Each qubit is capacitively connected to two coupled $\lambda/2$ resonators - a narrow readout resonator and a wide purcell filter, before connecting to the common feedline. Initial characterization of the sample in Continuous Wave (CW) spectroscopy can be quickly done to find the position and linewidth of the readout and purcell resonator frequencies using Network Analyzers. This transmission measurement, sweeping across the frequency of the attached resonator and purcell filter, can be fit to the expected analytic form of the Q.O. model of the same system (Fig. 2.13). Experimentally we use the narrow-linewidth readout mode to perform measurements, though high power readout [62] driving the purcell filter mode is a method we have also successfully tested.

4.2 Two-Tone Spectroscopy

We use two-tone CW spectroscopy next to characterize each qubit connected to their resonator networks. By measuring the shift of the tone applied to the readout resonator while sweeping a separate, second tone to drive the qubit we look for the location in frequency and power where the second tone causes the readout resonance to shift due to the disper-

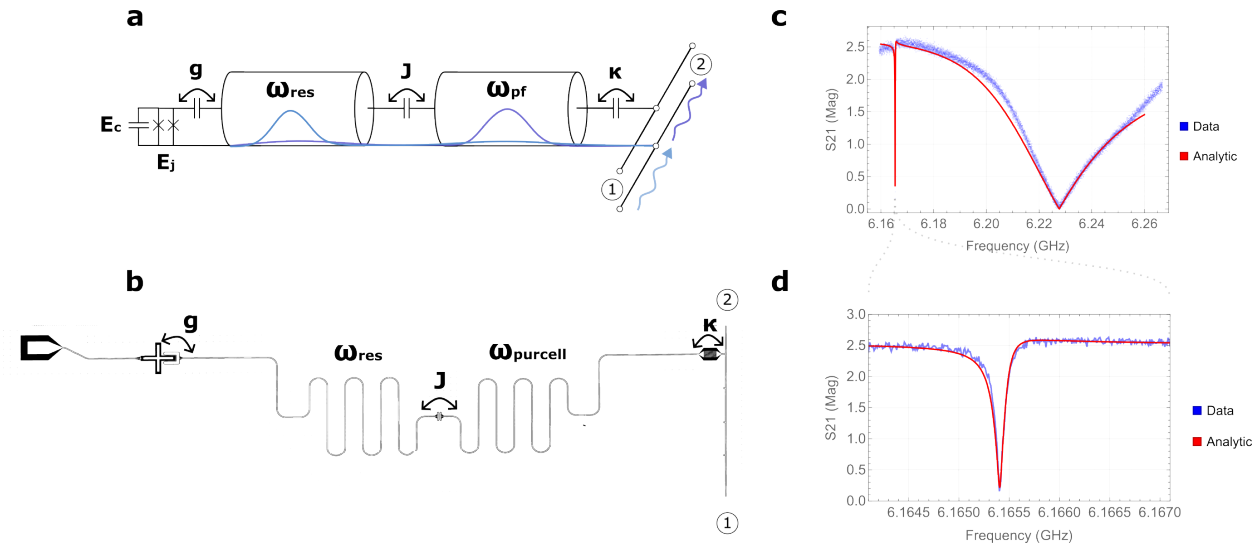

Figure 4.1: **Single-Tone Readout and Purcell Resonator Measurement**. We begin probing the sample by measuring the transmission response of photons sent through the common feedline at the readout and filter frequencies. **a,b** The diagrammatic model and optical image on-chip of the double-resonator system implemented as capacitively coupled CPW $\lambda/2$ resonators. **c,d** The input-output model for this resonator network is matched to the transmission spectrum, which we use to extract the circuit parameters.

sive coupling. We fit these data points to the Jaynes-Cummings model for each qubit as a function of flux.

$$(H_q + H_r + H_I)/\hbar = \omega_q/2\sigma_z + (\omega_r + \chi\hat{\sigma}_z)\hat{a}^\dagger\hat{a}$$

Once we have fit model parameters for each qubit, we truncate the qubit $\omega(\Phi)$ relation to the single 1/2 period containing $\Phi = 0$, which gives us an invertible function $\Phi(\omega)$ within this interval. We use these truncated functions to relate changes in frequency to changes in flux, and we will see later that this becomes quite useful when dealing with crosstalk between qubits.

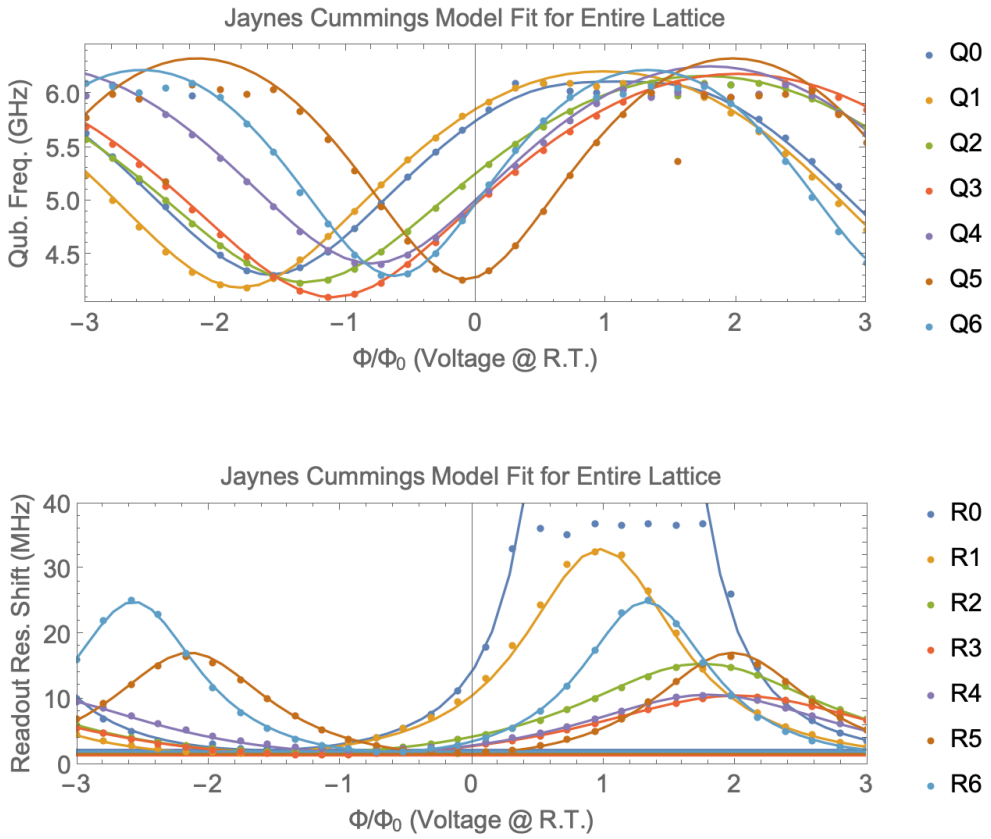

Figure 4.2: **Jaynes-Cummings Model Fit**. For each qubit + readout resonance in our system we perform two-tone spectroscopy extract the **a** readout resonance and **b** qubit frequency as a function of applied flux. In each case we fit the Jaynes-Cummings Hamiltonian to both the measured g/e qubit transition and the measured qubit ground state resonator frequency

4.3 Qubit Readout

To enable single-site microscopy in our lattice we need to calibrate our homodyne detection on the readout mode on each qubit. Using the above CW measurements we see a transition minima in S_{21} at the mode of the readout resonator. To perform homodyne detection we measure the change in response of the magnitude and phase of a single frequency we probe - detecting the χ shift of the readout mode frequency magnitude and phase due to the state of the qubit.

During the pulse sequence there is a dedicated readout window wherein a readout pulse ("windowed" by a square wave) drives the readout resonator mode, where we measure the state of the qubit dispersively via down-mixing the frequency using homodyne detection. The time-trace of this pulse is stored in the Keysight M3102A digitizer, which collects both quadratures of this down-mixed signal from an IQ mixer at 500MS/s. By integrating the signal over time each shot of the experiment contributes to a Gaussian profile distribution4.3 about the mean value in IQ space, with width given by vacuum noise and additional classical contributions from electronics (such as the HEMT) and thermal background.

The separation between the measured values is the fidelity of the readout. For the data presented in Fig. 4.3, the fidelity metric

$$F_q = 1 - (P(0|\bar{0}) - P(\bar{0}|0))/2$$

is used. The readout fidelity in this calibration experiment is 82%. The dominant contributing factor is decay during the readout window, which can be seen visually in the first image. On unstructured relabeling of the states using Gaussian mixture modeling from two distributions, most of the points that have decayed are re-labeled as ground state points. This allows us to construct a confusion matrix, where we use a calibration run to re-normalize the measurement value based on previously measured decay and excitation rates.

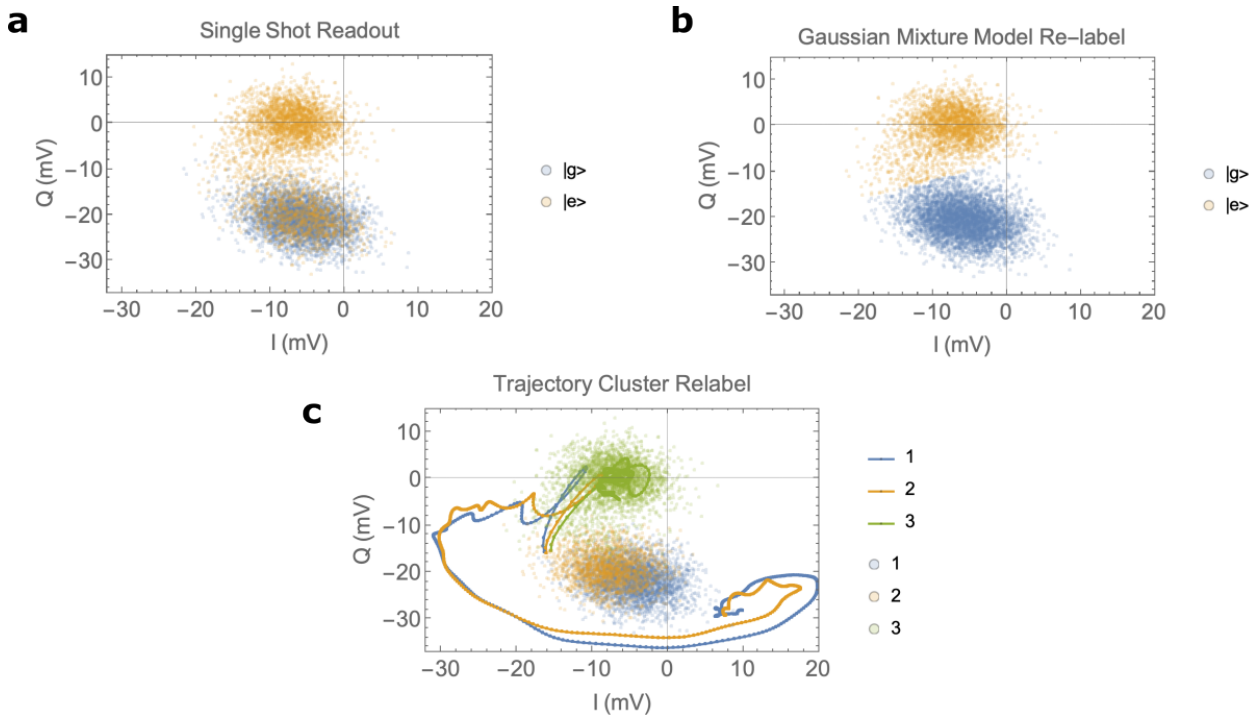

Figure 4.3: **Single Shot Readout**. To calibrate measurements of a qubit, we de-modulate microwave signals at the readout resonator frequency and look at the quadrature components (I, Q) as a function of the initially prepared qubit state $|g\rangle, |e\rangle$. **a** The single-shot measurements show when we prepare $|e\rangle$, many of these states decay to $|g\rangle$ during the readout, whereas heating ($|g\rangle \rightarrow |e\rangle$ is not seen). **b** We can use Gaussian mixture modeling to re-label the states. Using the learned distribution on successive measurements we can renormalize measured $|g\rangle$,$|e\rangle$ values using a confusion matrix. **c** Other methods, for future work, can use information obtained during the readout to further improve the fidelity. Here the full trajectory $(I(t), Q(t))$ is used to label three clusters. The mean cluster trajectories show a curve that aligns with $|e\rangle$ but shifts back towards $|g\rangle$, or qubit decay.

For future work, looking at the time-series trajectory information itself yields additional information. The last figure in Fig. 4.3 is unstructured re-labeling of these trajectories into three bins, showing the expected $|g\rangle$, $|e\rangle$ and an additional label whose mean trajectory aims closer to $|e\rangle$, then bends back towards the mean $|g\rangle$ measurement values, resembling a decay process. By truncating these measurements, the readout fidelity metric increases to $F_q = 0.92\%$ on the same data. Other methods, such as a neural-network approach, are also avenues for improvement in readout [63].

In practice we additionally sample frequencies around the $\pm\chi$ values, searching for a 1D

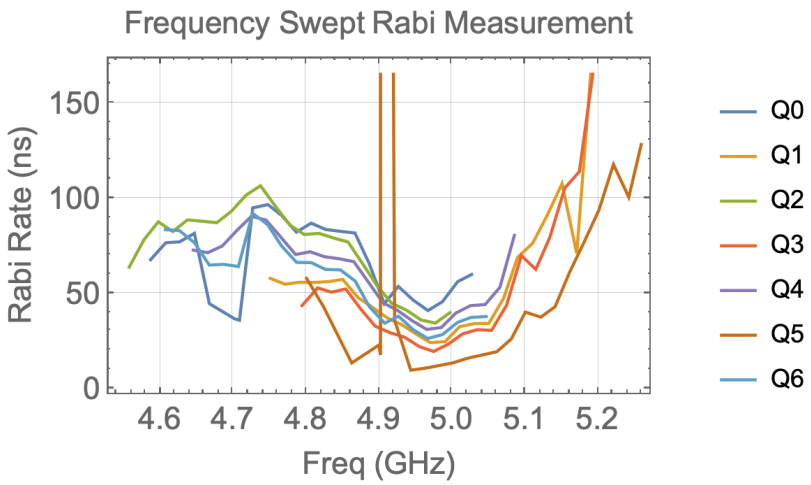

Figure 4.4: **Rabi Rate**. We calibrate the rabi rate for the staggered lattice of qubits. Part of the optimization for choosing the position of the staggered array frequencies is the rabi rate, which we sample by sweeping the frequencies of all qubits and repeating these experiments.

projection where homodyne detection remains invariant to observed crosstalk, e.g. invariance in subspace projected locations of $|g\rangle, |e\rangle$ under excitations of other qubits on the lattice which we observe, in exchange for optimum fidelity.

4.4 Qubit Drive

We apply power on a sideband through the common feedline to apply pulses to individual qubits rather than using hardware such as individually coupled charge drive lines to manipulate the state of the qubit. The advantage is a reduction in circuit complexity, but a disadvantage is the inability to address qubits individually, as all pulses are global. Thus, localization of coupling happens in frequency-space. At this point we already begin to motivate the initial staggered configuration for our qubit lattice, where nearest-neighbors are detuned by $\Delta_{NN} >> J$ with the additional constraint that non-nearest neighbors do not have frequency degeneracy (in our sample the upper and lower bands of qubits of evens and odds have an additional smaller stagger of $>$ 20MHz, allowing applied pulses to uniquely select qubits.

Using the information gained from sweeping the qubits in frequency and measuring the effective Rabi rates, we also choose the static disorder configuration location in frequency such that the drive rate Ω is insensitive to frequency drift. In Fig. 4.4 we can see the higher frequency qubits near 5GHz are close to $\partial_\omega \Omega = 0$ at a location with maximal coupling to the feedline.

4.5 Tomography

We are interested in collecting the single-site density matrix for each lattice site, a process which allows us to draw more in-depth conclusions about the physics of states on our lattice. This is necessary to see physics, such as the growth of global entanglement across the lattice through the single site purities $\mathrm{Tr}(\rho^2)$ as a function of disorder. In general, Tomography is the method of reconstructing the quantum state via repeated measurements performed on successive identical copies of the state. In this series of experiments we only reconstruct the many-body state up to the single-site density matrix using Maximum Likelyhood Estimation [64]. The process for doing this is outlined below.

We start by building a Cholesky decomposition of the density matrix, where t_i are real numbers:

$$T = \begin{pmatrix} t_1 & 0 \\ t_3 + it_4 & t2 \end{pmatrix}$$

and $\rho = \frac{T^\dagger T}{Tr(T^\dagger T)}$, so

$$\rho = \frac{1}{\sum_i t_i^2} \begin{pmatrix} t_1^2 + t_3^2 + t_4^2 & t_2(t_3 - it_4) \\ t_2(t_3 + it_4) & t_2^2 \end{pmatrix}$$

Because we always measure in the Z basis, projections onto X, Y require pre-rotating the state by Y_{-90}, X_{90} respectively (which can be seen by drawing the Bloch sphere). Measur-

ing each eigenvalue of each orthogonal projection X, Y, Z allows us to build the constraint equations to the density matrix:

$\langle X\rangle = Tr(X\rho) = 2t_2t_3$ $\langle Y\rangle = Tr(Y\rho) = 2t_4t_2$ $\langle Z\rangle = Tr(Z\rho) = t_1^2 - t_2^2 + t_3^2 + t_4^2$.

We use the Maximum Likelyhood Estimate method to reconstruct the density matrix by evaluating the 2-norm of the above observables over the repeated measurements: $C(|\psi\rangle) = \sum_i(\langle O\rangle_i - \langle O_\psi\rangle)^2$, where O runs over X, Y, Z and the sum runs over all measurements.

4.6 Flux Crosstalk

In order to tune each qubit's frequency ω_i we apply a local magnetic field by pushing current through that qubit's associated flux line. This current changes the magnetic field threading the SQUID loop, thereby changing the effective E_j and changing the ω_i. This is a good story, and it does work. Unfortunately, when we actually perform the experiment another effect is observed - the applied current I_i for qubit ω_i threads a nonzero magnetic field through other qubits $omega_j$, shifting their frequencies due to parasitic mutual inductance in the sample.

However, it is possible to correct for this. The parasitic mutual inductance between the neighboring SQUID loops and the flux lines, once measured, can be inverted (assuming linearity in the mutual inductance relation). There should exist an basis of N flux-vectors that create constructive magnetic interference at each of the N qubits.

To measure the degree of crosstalk between lines, we measure the induced frequency shift of the qubit ω_i due to changing the current I_j on another qubit's flux line, then normalize this response by the magnitude of the slope of the measured qubit. By sampling the qubit shift locally and normalizing we linearize the crosstalk:

$$\frac{\partial\omega_i}{\partial I_j}(\frac{\partial\omega_i}{\partial\phi_i})^{-1} = \frac{\partial\phi_i}{\partial I_j} \equiv M_{ij}$$

The non-linear relation $\omega(\phi)$ disappears from the mutual-inductance relation. M_{ij} above

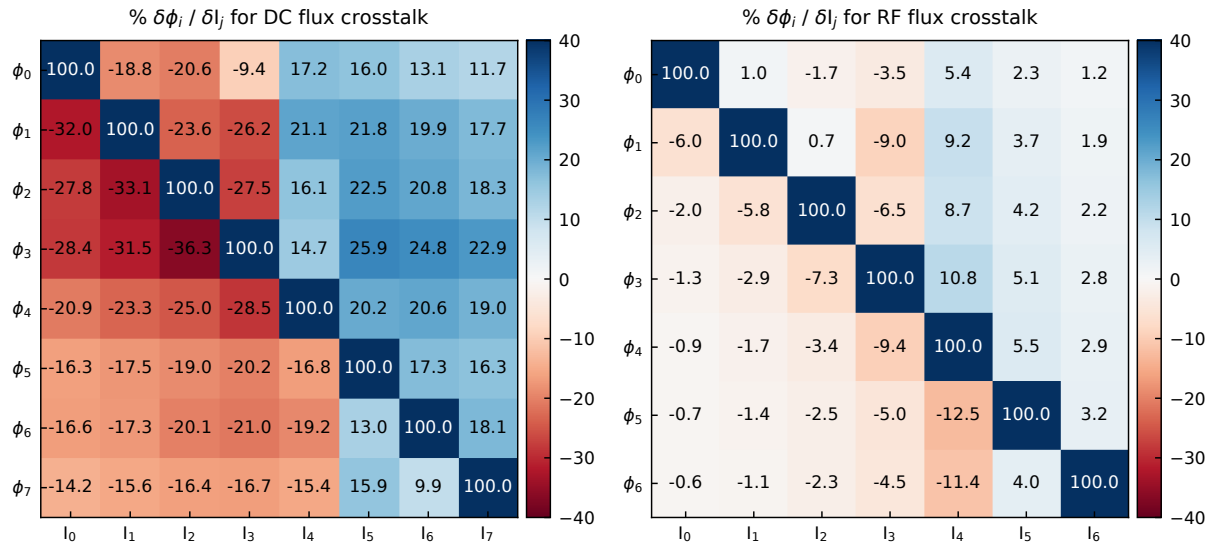

Figure 4.5: **DC, RF Flux Crosstalk Matrices**. Measured using the quibt frequency $\omega_i(\phi)$ response to changing I_j and normalizing to the slope of the measured qubit. See [2] Supplementary Figure S5.

now relates the rate of change of flux to current. Inverting M gives us a map $M_{ij}^{-1} : \Delta\phi \rightarrow \Delta I$ from flux to currents, and diagonalizing it informs us what flux vectors actually create the previously mentioned constructive interference to tune an individual qubit independently.

RF Crosstalk is measured in a similar manner except a square wave pulse is applied instead of a slowly varying DC signal on the flux line. In this regime we use the ratio of the steady state amplitudes in the μs scale to determine the crosstalk. When signals we apply vary over the duration of the experiment such as an adiabatic ramp or the diabatic ramp back to readout we apply the RF crosstalk matrix. The measured crosstalk matrices for our sample are shown in Fig. 4.5.

Measuring the crosstalk response can be done in several ways - we have chosen a method that works in our sample for the experiments we are performing. A potentially faster method to read the DC crosstalk values would be to measure the frequency response of the resonator, rather than the qubit, to flux changes applied to other qubits. Additionally, the decompo-

sition of flux crosstalk into "fast" and DC using the square wave basis may not be robust for future experiments, instead requiring decomposing the AC crosstalk into a frequency-sensitive crosstalk matrix $M(\omega)$ via Ramsey sequences [65]. This could give us additional insight and power to compensate for parasitic mutual inductance and couplings. Another possible solution for compensating flux crosstalk is to optimize for periodicity alone [66].

To mitigate the effect of DC crosstalk in our system we use an additional degree of freedom, a global magnetic field, to minimize the energy used tuning the lattice of qubits while compensating for the crosstalk.

4.7 Solenoid calibration

As each qubit has an individual flux line, when we solve for the current required I_i to produce the magnetic field ϕ_i to create the qubit frequency geometry we want $\omega_i(\phi_i)$, we would normally not have any wiggle room after solving this system. With an additional magnetic field that can thread flux through all qubits, we can decrease the energy required to achieve the required physical field. Since pushing current into the fridge pushes current through the cryogenic resistors and adds a heat load, this is the same thing as decreasing total power $P \sim \sum_i I_i^2$. After using the solenoid to change the distribution of applied current we observe a decrease in mixing chamber temperature from 9.7mK to 8.2mK.

To take advantage of the solenoid we measure the flux sensitivity of each qubit to the solenoid bias, in a similar fashion to the flux bias line measurement. We set the bias voltage on the flux lines to 0V and probe the qubit frequency in two-tone spectroscopy to bias current on the solenoid alone. Using the same physical parameters for the qubit in the Jaynes-Cummings Hamiltonian H_{JC} as the original flux bias line - we can see the shift in the pure voltage scaling due to the bias coming from a new source.

Superimposing the qubit frequency shifts on one another as a function of the solenoid bias (see Fig. 4.6) we see that, by tuning the solenoid, we can shift all of the qubits. to slight

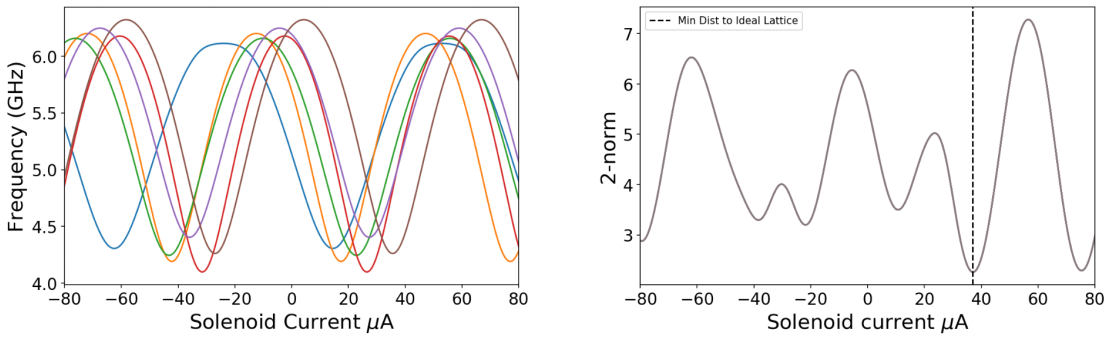

Figure 4.6: **Global Solenoid Calibration**. DC biasing flux lines contributes heat load at the MXC from filtering, biasing the lattice with a global solenoid field alleviates this load. Each qubit's flux sensitivity to the solenoid is measured, then the position for the solenoid is determined by minimizing the distance of the qubits from the desired DC staggered frequency configuration.

aperiodicity and frequency offsets for each qubit, we use a 2-norm metric of the distance in frequency from each qubit to a target lattice frequency configuration $\sum_i(\omega_i(I_{sol}) - \omega_i(\phi_{target})^2$ to optimize the solenoid current.

4.8 Anharmonicity

We calibrate the anharmonicity of each qubit by first putting the qubit into the $|e\rangle$ state, then looking for the frequency at which $|e\rangle/|f\rangle$ resonance occurs in pulse-probe spectroscopy (Fig. 4.7). We have good initial guesses for the frequency to sample in pulsed measurements as we can drive higher transitions using high-power CW spectroscopy.

4.9 Flux Pulse Calibration

When we apply pulses to the qubit SQUID loop through the flux line, there is invariably distortion. The impedance through the flux line is not 50 Ω - we have applied RC, eccosorb, and low-pass filters in-series connected to a Bias-Tee element, which end in a terminated flux line to ground near the qubit. Applying a fast pulse, such as a square wave, from

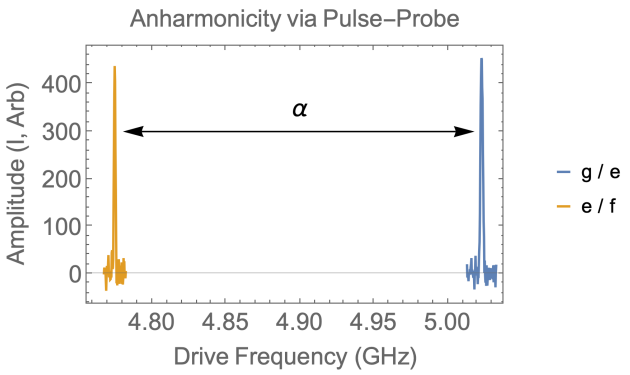

Figure 4.7: **Anharmonicity**. We drive the qubit of interest into the $|e\rangle$ state and sweep for a response to a short rabi drive around the expected anharmonicity. Once a signal is found we calibrate the amplitude and time of the e/f pulse and extract the anharmonicity as the difference between the frequencies.

an AWG will reproduce a waveform distored by the aforementioned circuit elements at the qubit SQUID loop. At the sample, flux pulse distortions on the short and long time scales accumulate and must be compensated [67, 68].

We correct the flux pulse distortions using linear response theory. The applied square wave pulse from the AWG is an input signal $x(t)$ distorted by an effective transfer function $u(t)$ which produces a changed output signal $y(t)$. We use the qubit as an oscilloscope to probe the output signal through time $\omega(t)$.

The output waveform's distortion is given by the convolution of the transfer function with the input signal:

$$y(t) = x(t)u(t)$$

The Fourier transform of the above means we can re-express the impact of the response function in the frequency domain and invert it:

$$Y(\omega) = X(\omega)U(\omega)$$

$$U^{-1}(\omega)Y(\omega) = X(\omega)$$

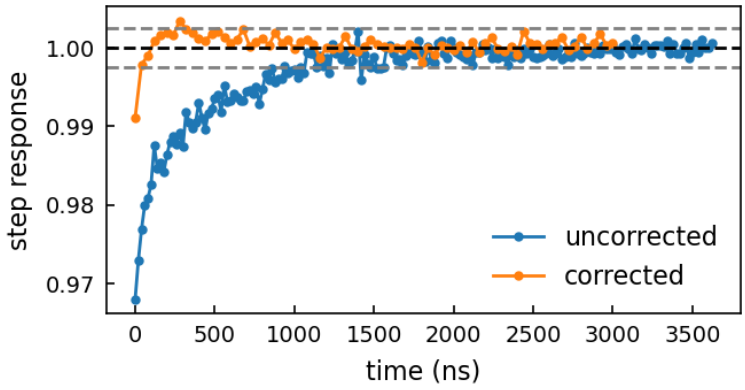

Figure 4.8: **Flux Pulse Calibration**. We use the qubit frequency as an oscilloscope to probe the transfer function distorting pulses between the AWG output port and the qubit SQUID loop. By inverting the transfer function and pre-distorting the pulse we send out of the AWG to the qubit, the signal that reaches the qubit looks far closer to theory. Here we see a pre and post-corrected square wave sent to Q5 using this method. The grey lines enclose a width of 1MHz, .5% of the amplitude of the ramp. See [2] Supplementary Figure S6.

So by inverting the transform on U^{-1}, we can apply the time-domain kernel $u^{-1}(t)$ to $y(t)$ and recover the input waveform we wish to apply - that is, invert the distortion.

We simplify this process by looking at the response of $y(t)$ to a step input $x(t)$. An impulse-response characterization of the transfer function would call for a Dirac-delta distribution on the input:

$$y(t) = \int_{-\infty}^{\infty} u(t)\delta(t-\tau)d\tau = u(t)$$

but it is much easier to synthesize and still recover the transfer function:

$$y(t) = \int_{-\infty}^{\infty} u(t)\Theta(t-\tau)d\tau \rightarrow y'(t) = u(t)$$

When we measure the qubit frequency response $\omega(t)$ we excite the qubit with a broad 20ns gaussian pulse at a time t_0 in the experiment. We then fit the qubit responses at each time to a Lorentzian and plot the central values over the duration of the step pulse to extract

$y(t)$. In practice we further simplify the problem and assume the response function U acts a single pole element and fit the qubit response to the analytic exponential. We invert the frequency response $U^{-1}(\omega)$, with a cutoff applied to truncate high frequency behavior, and apply the inverted kernel to our AWG inputs: $x(t)u^{-1}(t)$ as the corrected and pre-distorted flux bias inputs.

4.10 Tunneling

We have designed our circuit to have a nearest-neighbor capacitive coupling strength $-t\sum a_i^\dagger a_j$ of 10 MHz, but we need to experimentally verify this. We do so by sampling the swap rate for a single excitation between two neighboring qubits (keeping all other lattice sites far detuned) and iterating over values of frequency detuning between the qubits. By sampling detuning values we give ourselves an additional benchmark to ensure our flux-correction protocols are working as intended - as the minimum swapping rate should occur at minimum disorder (neighboring qubits on-resonance) and increasing disorder increases the swap rate. Explicitly, we populate the stationary qubit with one photon and diabatically ramp the other qubit to a specific detuning and measure the swap rate.

In more detail - a two-spin system

$$H = \hbar\omega_L\sigma_{zL} + \hbar\omega_R\sigma_{zR} + \frac{g}{2}\left(\sigma_L^+\sigma_R^- + \sigma_L^-\sigma_R^+\right)$$

Solving $-i\hbar\partial_t|\psi\rangle = H|\psi\rangle$ yields a time-dependent solution for a single excitation with $\omega\ \sqrt{g^2+\Delta^2}$ where $\Delta = \hbar(\omega_L - \omega_R)$. We then extract g searching for the minimum frequency $\omega : \Delta \to 0$. Results for sweeping the neighboring Q0,Q1 are shown below:

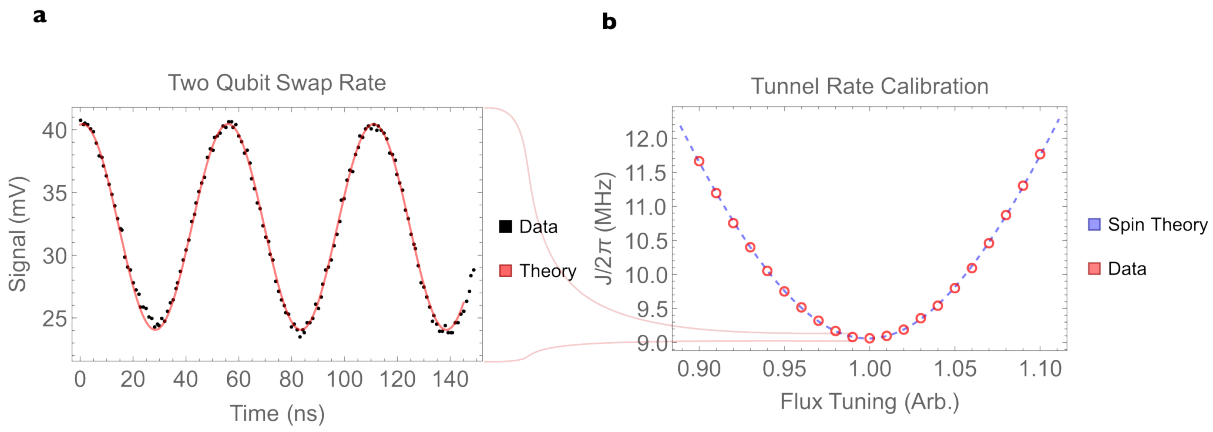

Figure 4.9: **Nearest Neighbor Tunnel Calibration**. By taking two neighboring qubits Q_L, Q_R and **a** measuring the single photon swap rate $g_{eff} = \sqrt{g^2 + \Delta^2}$ between them **b** across detuning values $\Delta = \omega_L - \omega_R$ controlled by a flux tuning vector we are able to extract the zero detuning $\Delta = 0$ bare coupling frequency g between nearest-neighobrs on the lattice.

4.11 Lifetime

We benchmark the excitation loss rate T1 for each qubit by measuring the exponential decay rate of the excited state $|e\rangle$ to the ground state $|g\rangle$. As our experiment involves flux-tuning the qubits along trajectories in frequency, we sample $T1(\omega)$ along the path each qubit takes from the intial staggered configuration ω_i to the disorder-less lattice ω_f. Part of the initial calibrations we perform involve choosing a frequency configuration where we observe high lifetimes over the frequency bandwidth we wish to operate in, which can be pictured as applying a global DC frequency offset to the experiment to shift out of observed low T1 regions. Dephasing $T2^*$ is sampled via a ramsey sequence for each quit in the same way as part of an automated process along these frequency points, yielding typical lifetimes between $1 - 4\mu$s.

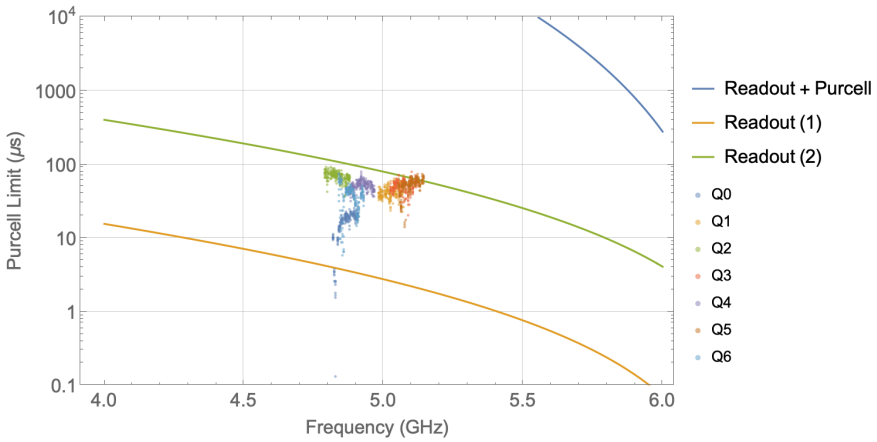

Figure 4.10: **T1 vs** ω . We calibrate the T1 for each qubit in the lattice, sampling along frequency positions (here swept nearby the stagger). We show the purcell limit for the readout scheme again (Fig. 2.17) for reference

4.12 Landau Zener Characterization

ω_1 in the table of values refers to the disordered stagger values for the larger detuning, while ω_2 refers to the smaller stagger. We use two separate disorder configurations to avoid errors from Landau-Zener transitions in state preparation by apply excitations at the smaller array past the $|ee\rangle\langle fg|$ transitions ($\Delta_{NN} < U$).

In characterizing the severity of the unavoidable LZ errors we pick up on readout, wherein the disorderless lattice is "ripped apart" by applying a step-response pulse to each qubit's flux-line to bring each site to the large-staggered array, we calibrate against a worst-case nearest-neighbor LZ error for a square-wave pulse on the flux line transitioning each qubit from the smaller stagger to the larger stagger (Fig. 4.11).

We measure accumulated $|f\rangle$ state population of $< 5\%$ for all qubit pairs using this method. By extension, the larger detuning from the disorder-less lattice using the same functional step pulse to tune qubits to the final larger disordered configuration, we should expect a smaller $|f\rangle$ state population as our parameterized LZ velocity [69] (flux tuning) is faster.

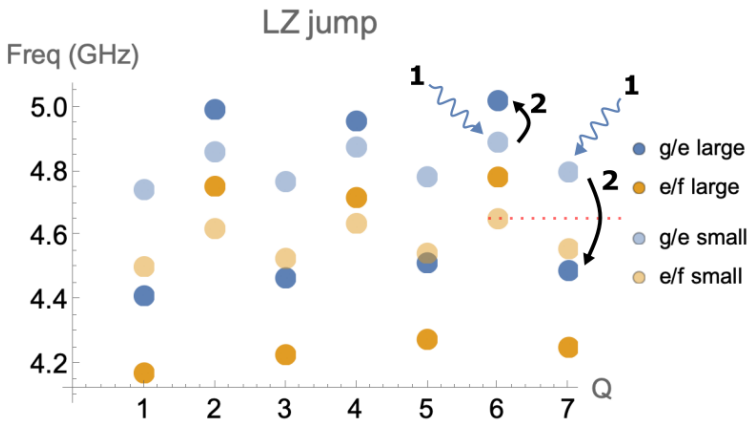

Figure 4.11: **Landau-Zener error characterization**. We accumulate error from Landau-Zener transitions on qubits whose nearest-neighbors have population in the excited state due to our staggered configuration for readout having a detuning $\delta > U$, so the matrix element $|gf\rangle\langle ee|$ can contribute to the dynamics, pushing our system outside of the intended Hilbert space. We characterize this error by looking at neighbors, (1) pushing them to $|ee\rangle$ in the small disorder configuration, then (2) applying a step pulse to push them to the larger staggered configuration, and reading out the $|f\rangle$ state population.

4.13 Table of Values

After benchmarking our sample, the parameters of our sample are (Table 4.1):

Qubit	**1**	**2**	**3**	**4**	**5**	**6**	**7**
$U/2\pi$ (MHz)	-241	-240	-240	-239	-239	-239	-240
$J_{i,i+1}/2\pi$ (MHz)	9.0625	9.032	8.842	8.936	9.023	9.040	–
$\omega_1/2\pi$ (MHz)	4410	4992	4466	4956	4513	5020	4489
$\omega_2/2\pi$ (MHz)	4742	4860	4767	4875	4782	4890	4797
$T1(\mu s)$	14.6	35.5	57.7	28.4	60.3	54.7	40.0
$T2*(\mu s)$	0.85	0.64	1.31	0.77	3.57	0.84	1.4
$\mathrm{F_{ge}}$	0.91	0.92	0.93	0.95	0.87	0.92	0.83
$\omega_\mathrm{r}/2\pi$ (GHz)	6.197	6.323	6.427	6.556	6.655	6.78	6.871
$\kappa_\mathrm{r}/2\pi$ (KHz)	359	553	203	235	292	220	894
$g_\mathrm{r\text{-}q}/2\pi$ (MHz)	60	63	72	64	78	70	70
$\chi_\mathrm{r\text{-}q}/2\pi$ (MHz)	0.48	1.23	0.78	1.24	0.90	1.71	0.73
$\omega_\mathrm{p}/2\pi$ (GHz)	6.256	6.486	6.706	6.936	7.055	6.843	6.604
$\kappa_\mathrm{p}/2\pi$ (MHz)	77.5	52.7	92.5	72.4	103.1	56.9	60.8
$g_\mathrm{r\text{-}p}/2\pi$ (MHz)	3	3.5	6	6.5	5	6	4.5

Table 4.1: **List of Sample Parameters**

CHAPTER 5

EXPERIMENTAL RESULTS

5.1 Preparing Compressible States of Light with Disorder

We have gone through great effort in designing, fabricating, and calibrating a one-dimensional lattice of transmon qubits (Fig. 5.1) capable of producing strongly-interacting Bose Hubbard Physics. However if we proceed to place this lattice within the fridge immediately and carefully measure it as-is, we will simply measure the vacuum state. The critical next step to studying interesting physics on our Bose-Hubbard simulator is to create desired states and then measure observables. We are preparing quantum many-body states, so entanglement and delocalization across lattice sites will increase the complexity of both the state and therefore state preparation. There are several popular ways to overcome these challenges.

In previous work [37], we used a dissipative state preparation scheme on the same lattice architecture with L = 8 sites in the unit filling Mott Insulator state, so N = 8 excitations over eight sites gives N/L = 1 photon per site to form this in-compressible many-body state. To stabilize the Mott Insulator state on the lattice we take one edge lattice site and drive the two-photon transition $|g\rangle \leftrightarrow |f\rangle$, and wait for the engineered (enhanced) decay $|f\rangle \rightarrow |e\rangle$. The excitation tunnels into the neighboring empty lattice and the driven site would refill to $|g\rangle \rightarrow |f\rangle$, repeating the process until the lattice is filled (the neighbor never empties). This process terminates at unit filling as the energy required to fill the "full" lattice with a new photon is detuned by the anharmonicity - so the many-body gap stabilizes the many-body state. This process works in the aforementioned in-compressible Mott Insulator phase, but we now seek a method to stabilize the intermediate compressible states where the density of photons $n = N/L < 1$.

In this work, our approach uses another popular method of state preparation - adiabatic assembly. Suppose we have an initial Hamiltonian $\hat{H}(k)$, parameterized by some scalar k and

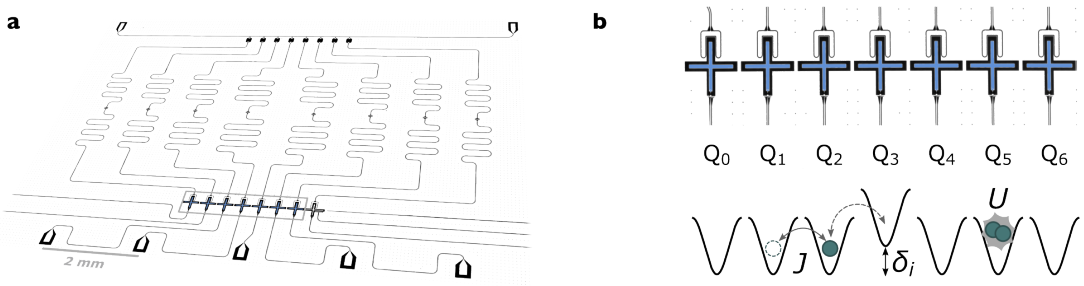

Figure 5.1: **Experimental Platform**. **a** Optical image of the cryogenic microwave circuit. Highlighted in blue **b** is the one-dimensional lattice of transmon qubits which form the strongly interacting Bose-Hubbard Hamiltonian for photon excitations. Image from [2], Figure 1.

a prepared eigenstate $\psi(k)$ within the system. Slowly varying the parameter k allows the eigenstate $\psi(k)$ to "follow" the change we induce and remain an instantaneous eigenstate across the values of k. If the change is adiabatic, all of the initial eigenstates ψ_n follow the connected instantaneous eigenstate paths through the parameterization from $\hat{H}(k(t_i))$ to the final configuration $\hat{H}(k(t_f))$. However, we don't get this for free: the "rate" of our allowed speed $\frac{dk}{dt}$ in this process is limited by the many-body spectrum in the energy level landscape. Our process becomes *diabatic*, or non-adiabatic, once our parameterization speed causes population transfer between eigenstates. We will use this adiabatic tuning method, but we will parameterize the disorder within our system.

5.2 Disorder and Adiabaticity

Let us explicitly write the Bose-Hubbard Hamiltonian calling out the fact that we are free to induce on-site frequency changes using flux-tuning of the transmon qubits:

$$\hat{H}_{BH} = -J \sum_{<i,j>} a_i^\dagger a_j + \frac{U}{2} \sum_i n_i(n_i - 1) \sum_i (\omega_0 + \delta_i) n_i$$

where J and U are, again, the nearest-neighbor tunneling and the on-site anharmonicity

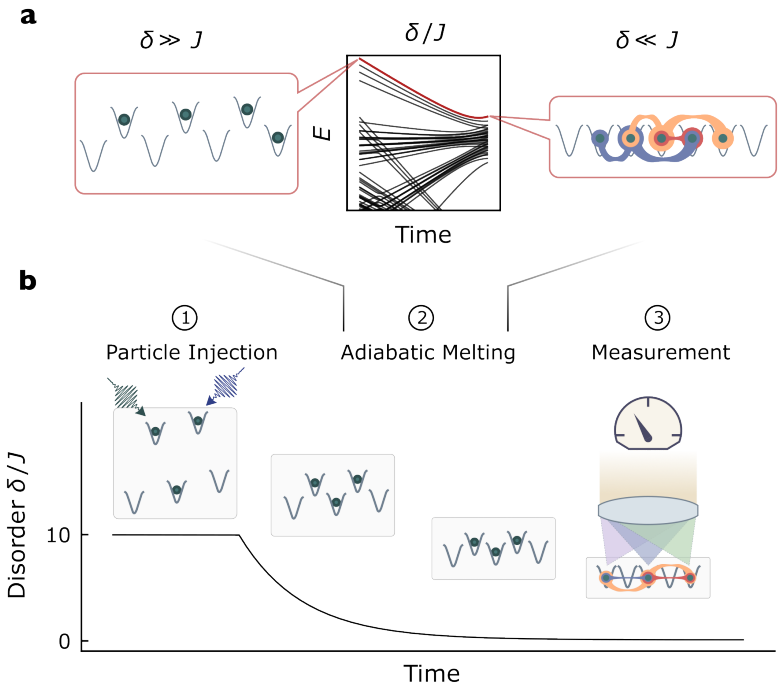

Figure 5.2: **Adiabatic tuning of Disorder**. **a** Eigenstates in a fixed disordered lattice with suppressed tunneling are localized excitations on each site. Adiabatic removal of this disorder connects each of these simple states to one of the disorder-less eigenstates on the traditional 1D chain, which can have delocalized excitations and entanglement. **b** We create the eigenstate in the disordered lattice by (1) applying local excitations to qubits, then (2) ramping the disorder down adiabatically and (3) creating and measuring fluid-like states of light on the lattice. To prepare a target eigenstate on the resonant lattice we choose the corresponding eigenstate in the disordered lattice to prepare. Image from [2], Figure 1.

for the electromagnetic microwave excitations on the transmon lattice sites. ω_i and δ_i are the on-site energy and energy shift due to flux tuning for each lattice site.

To simplify state preparation it makes intuitive sense to simplify the system $\hat{H}$. We do this by adding disorder $|\delta_i| >> |J|$ between lattice sites - ensuring eigenstates are now simply products of localized photons on individual lattice sites. Eigenstate preparation in this disordered configuration amounts to creating products of localized excitations, we simply choose which qubits we need to excite to reach the desired eigenstate and excite them as separate qubit drives.

A major point in this work is treating this added disorder as an adiabatically tunable parameter 5.2. After moving to a desired eigenstate ψ with the above excitations on single qubits (1), we now remove the disorder (2) as a tunable parameter $\hat{H}(\delta \to 0)$ to recover the disorder-less Bose Hubbard lattice (3) and the target eigenstate ψ we desire, where we can perform measurements to characterize these rich many-body states.

This experiment can be run backwards initially (in theory) to look at a desired state in the disorder-less $H(\delta = 0)$, then track along the instantaneous eigenstate paths as the disorder increases until finding which of the initial eigenstates in the disordered configuration correspond to the desired state. Then, preparing that state experimentally and following the adiabatic trajectory of disorder removal will create that desired state.

5.3 Single Particle Eigenstates

The simplest versions of the disorder assembly protocol are the states spanned by single excitations. With only a single excitation, the interaction term $U \sum n_i(n_i - 1)$ which is responsible for generating interactions between photons now contributes no physics. Without disorder, all sites have the same energy so we can ignore the on-site term and we are left with nearest-neighbor tunneling. Thus, $\hat{H} = -J \sum_{<i,j>} \hat{a}_i \hat{a}_j$ and so the system reduces to the eigenmodes of a particle-in-a-box.

We show the dependence of these eigenstates upon disorder and their corresponding energies in Fig. 5.3a. At maximum disorder (left) each eigenstate is an excitation localized to a single site, while near zero disorder the eigenstates are delocalized particle-in-a-box (right). By adiabatically tuning the disorder we follow connected manifolds of instantaneous eigenstates. Thus, we form a unique map of eigenstates between the disordered lattice configuration and the disorder-less configuration. For the single-particle case, we have a unique map between the single lattice site excitation in the disordered configuration and the eigenstate of the particle-in-a-box case.

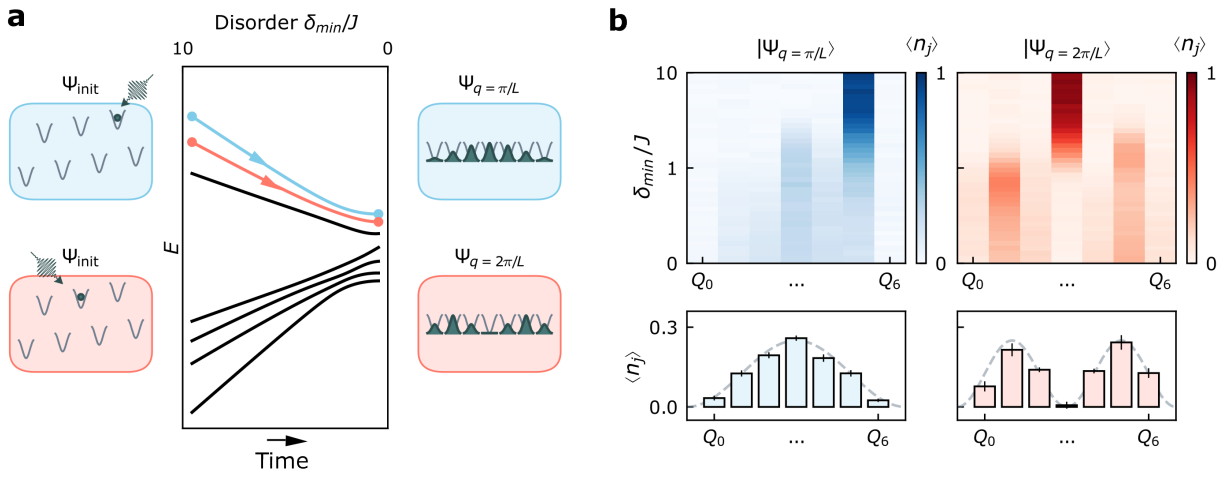

Figure 5.3: **Single Particle Eigenstates**. **a** In the single-particle manifold (shown numerically) we apply excitations to single sites in the "sawtooth" disordered configuration to reach an eigenstate of choice. The highest and second-highest lattice sites map to the lowest and second-lowest quasi-momenta disorder-less eigenstates, producing particle-in-a-box states set by the open boundary conditions of the lattice. **b** We measure the population change over the lattice during the adiabatic ramp by diabatically ramping the lattice apart at variable values of disorder. For both quasi-momenta values we observe the expected delocalization of the single excitation to the lattice quasi-momenta eigenstates. Image from [2], Figure 2.

By examining this "sawtooth" staggered configuration depicted in cartoon form in Fig. 5.3a, we can pick out the highest and second-highest eigenstates by exciting the highest and second-highest frequency qubits: Q_5 and Q_3 indexed by their positions. In Fig. 5.3b, we plot the measured density profile of each instantaneous eigenstate as we adiabatically remove disorder from the staggered lattice. We can see the excitation delocalize from a single site across the empty lattice sites, taking on the profile of the sinusoidal probability distributions for the $q = \pi/L$ and $q = 2\pi/L$ particle-in-a-box/quasi-momentum states. Note that we quote $J > 0$ in our platform, with a global minus sign for the kinetic term in the Hamiltonian. In a hard-core band with a fixed photon number, the lowest and highest-energy eigenstates are connected through a gauge transformation (by changing the sign of J). Without impacting the physics, we focus our efforts in preparing the higher-energy states.

Our system, comprised of qubits with finite decay times for their electromagnetic excitations, exhibits decay for each of the states we prepare. Our adiabatic state preparation protocol therefore must compete against the timescales of these decay processes. We must evolve faster than the decay time of the photons, but slower than the timescales dictated by the transition to diabiaticity.

To simplify adiabatic state preparation in our system, we parameterize the detuning $\delta(t)$ as an exponential ramp to reduce the degrees of freedom needed for optimization: $\delta(t) = \delta_i e^{-t/t_0}$. By sweeping over the timescale of the exponential ramp we are able to quickly establish a ramp trajectory that satisfies adiabaticity while roughly taking advantage of the gradient in the many-body instantaneous-eigenstates as the disorder is removed.

To establish whether an exponential ramp is reversible we look to see if the final state, after *reversing* the trajectory is the same as the initial prepared state. We take the ramp trajectory towards the disorder-less lattice, then we mirror the trajectory back out again to the disordered lattice (Fig. 5.4a). If the ramp rate is too fast and has a diabatic component we will gain population overlap with other eigenstates. Shown in the cartoon figure is an

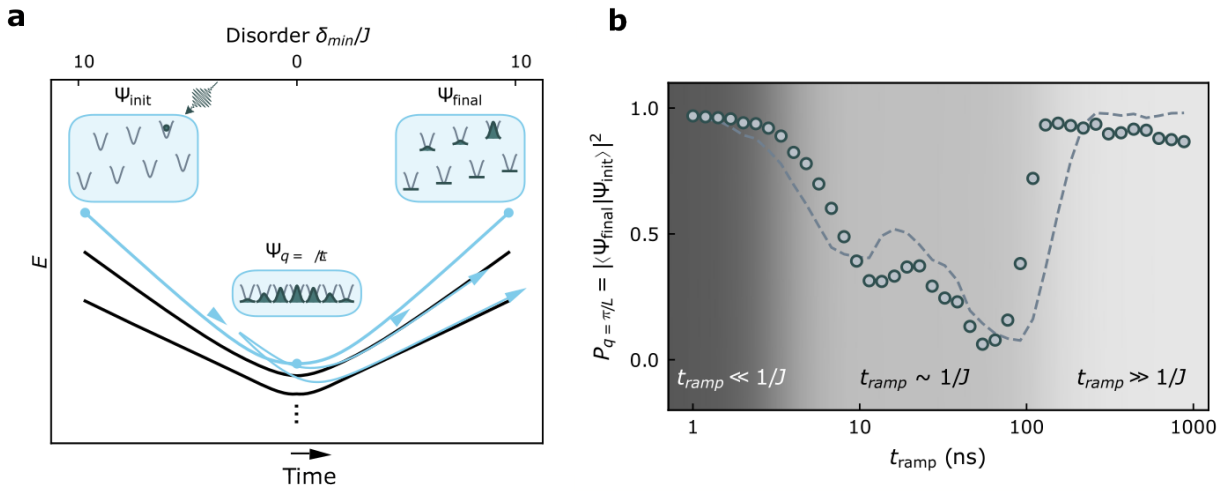

Figure 5.4: **Characterizing Adiabaticity**. We require adiabatic, or reversible, ramps to connect eigenstates between the disordered and disorder-less lattices. **a** To test reversibility of a ramp sequence to remove disorder in the single particle manifold we start with an eigenstate and apply both the ramp and the reversed ramp sequence. If the sequence is reversible the end population distribution should match the initial distribution - a single localized excitation. The population on this site is our fidelity metric. **b** This population recovery is our metric for reversibility as we sweep an exponential ramp profile over timescales ranging 1ns to 1μs. Image from [2], Figure 2.

example for the single particle lowest quasi-momentum case. By ramping diabatically to the lattice we will transfer some population to other eigenstates. By inverting this ramp process the diabatic transition places the transferred population we have accumulated into other eigenstates, into other localized qubits. Thus, to quantify reversibility $|\langle\psi_{init}|\psi_{final}\rangle|^2$ we can look at the loss of population on the prepared site in the localized eigenstate basis on the disordered lattice. To optimize adiabatic trajectories for multi-particle states (Fig. 5.5) we use a similar method to the single particle case, maximizing projection of the population to the initially populated states.

This is the metric we use to evaluate reversibility as we sweep the ramp timescale for the exponential ramp trajectory of disorder. For the single particle case an the lowest quasi-momentum, we collect data on the reversibility over a range of ramp timescales (Fig. 5.4b). Initially the ramp timescale $t_{ramp} \ll J^{-1}$ is fast enough that it outpaces the physical processes for tunneling (which happens at a frequency J) and the excitation remains in place at the same lattice site, so the reversibility metric $|\langle\psi_{init}|\psi_{final}\rangle|^2$ remains high. As the process slows and we enter the $t_{ramp} \sim J^{-1}$ regime, tunneling between the lattice sites takes place and diabatic transitions to other states suppress the population amplitude on the initial lattice site when the ramp is reversed. As the ramp continues to slow down and we enter $t_{\text{ramp}} \gg J^{-1}$, the state adiabatically delocalizes and relocalizes back to the same site as the lattice loses and gains disorder respectively.

5.4 Multi-Particle Melting

Motivated by the success in single-particle state preparation - we can explore the natural extension to multi-particle states on the lattice. With multiple photons existing at the same time the interaction term U will begin perturbing the behavior of our physics away from non-interacting bosons (Fig. 5.7) . As we fill the lattice with N excitations on L lattice sites N/L = 2/7,3/7...6/7, we are preparing what are called "compressible" fluid-like states of

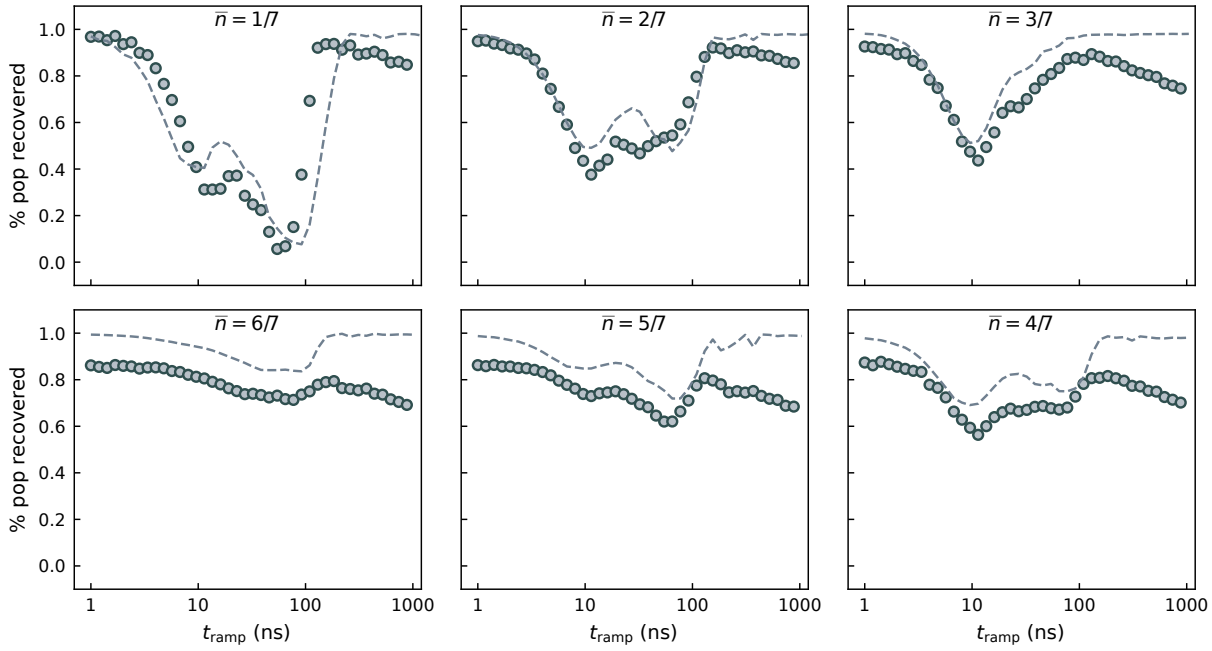

Figure 5.5: **Reversibility vs Density**. To prepare any state adiabatically, including the higher particle number compressible states on the disorder-less lattice, we benchmark the reversibility of the same exponential ramp sequence as in the single particle case. As particle number increases the state fidelity decreases due to loss. Image from [2], Extended Data Figure 1.

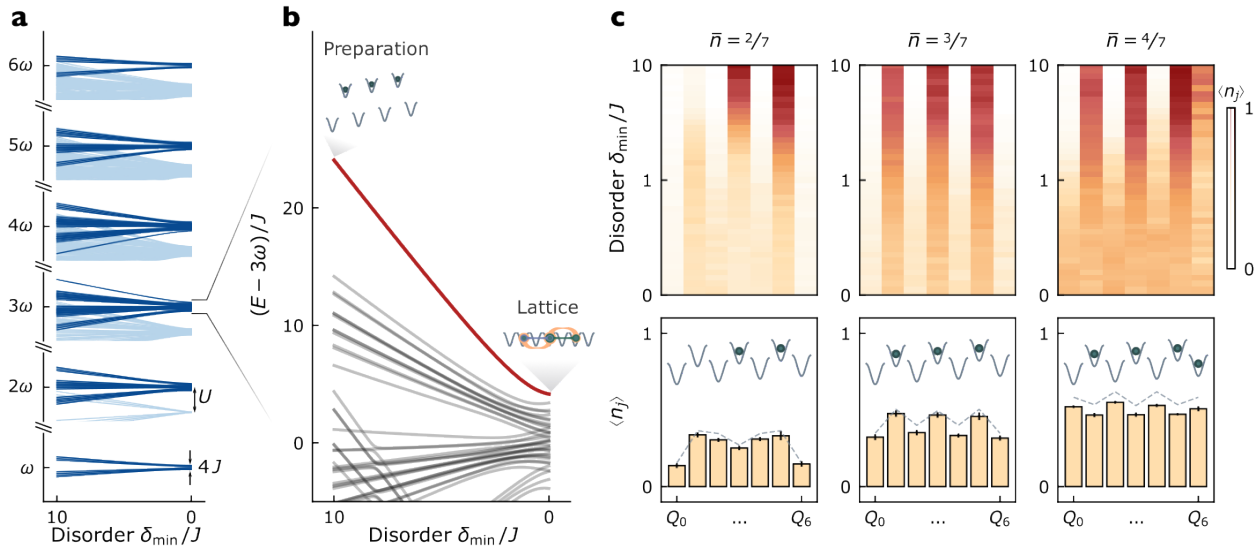

Figure 5.6: **Multi-Particle State Assembly**. By exciting more than one site initially we can prepare multi-particle fluid states on the lattice. **a** The instantaneous eigenstate energy levels increasing in particle number, demonstrating the separation in scales for the tunneling energy J, the anharmonicity U (separating the excitations with doublons), and the energy required to add an entire particle ω. **b** The three-particle manifold. The disordered state is prepared with all sites in the top frequency band populated and all sites in the bottom empty, leading to a large many-body gap in the ram (red) to the lowest quasi-momenta state. **c** Instantaneous population measurements vs disorder during the melt for the lowest quasi-momenta for N=2,3 and 4 excitations. As more photons are added photon loss causes further deviations from the theoretical predictions (dashed line). Image from [2], Figure 3.

light on the lattice. Despite the strong interaction term $U \gg J$ between the photons they can still delocalize and exchange kinetic energy as we remove disorder. At the $N/L = 1$ density we arrive at the incompressible Mott Insulator phase, where applying additional excitations requires applying energy at a frequency detuned by the anharmonicity U - as there are no accessible empty states left near the same energy ω.

The instantaneous eigenstates as a function of disorder for higher particle numbers can be seen in Fig. 5.8a. Here we truncate the Hilbert space to two excitations per lattice site. The smallest energy scale J sets the scale for phonon excitations in the disorder-less lattice, while the interaction term U sets the energy scale for doublons. Looking up from the single particle manifold ω, by adding another N particles with ω (the highest energy scale) we see,

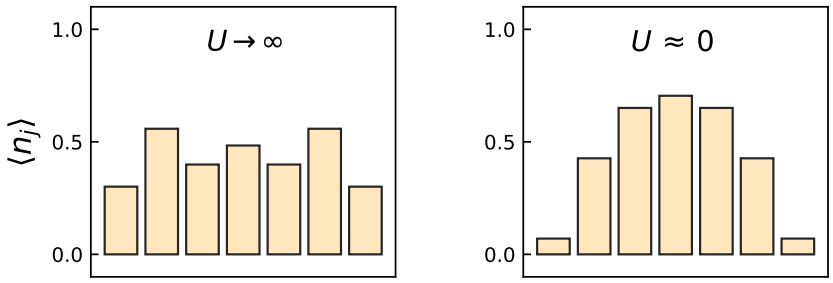

Figure 5.7: **Interacting Photons**. By mediating *strong* interactions between photons using qubits, even **a** three excitations are enough to see a drastic change in particle distribution relative to the **b** non or weakly interacting case, where the lowest quasi-momenta is, if at all, only weakly perturbed.

in the disorder-less case, accessible states up to the last Mott Insulator state with density $N/L = 7/7$.

For the $N/L = 3/7$ particle case, we zoom in on the instantaneous eigenstate diagram to show the trajectory we take experimentally. We excite the highest-energy top band of qubits in the disordered "sawtooth" configuration. In this case we follow an instantaneous eigenstate path that is well-separated in energy from other states, allowing us to traverse an adiabatic path at a fast rate. As in the single-particle case, the localized excitations on the three separate lattice sites delocalize and entangle as the disorder is removed adiabatically, reaching a new eigenstate at the disorder-less configuration.

We measure multi-particle disorder-assisted adiabatic preparation of the lowest quasi-momentum eigenstate for up to $N/L = 6/7$ (Fig. 5.8). These data demonstrate that during the melt the photons delocalize from their initial sites into all lattice sites with the melted density profiles at the end being good agreement with the disorder-free numerics from exact diagonalization, though we observe increasing infidelty scaling with N in our prepared states coming from particle loss and crosstalk.

5.4.1 Tonks-Girardeau Gas Model

Exact diagonalization is not the only tool we need to describe our system. We operate in the regime where interactions outstrip the energy scale of tunneling: $U \gg J$ and so we have a lattice of strongly interacting bosons (photons). Because we restrict excitations to the single particle per site manifold, the sign of U does not influence the physics and we can model our system as a Tonks-Girardeau gas [70, 71] of repulsing bosons in 1D. The ground state is of the Bijl-Jastrow [72] form. This wavefunction is written as the product of single- and two-particle components $\Psi_B(\mathbf{x}) = \phi(\mathbf{x})\varphi(\mathbf{x})$, for $\mathbf{x} = (x_0, x_1, \ldots, x_6)$ [73]. The single-particle component $\phi(\mathbf{x}) = \prod_{i=0}^{6} \cos(\pi x_i/L)$ corresponds to the non-interacting lowest-energy particle-in-a-box state of the lattice. Without interactions each photon sees the finite tight-binding lattice and, without excitations, will all condense to the ground state of the system.

The two-point contact interaction term $\varphi(\mathbf{x}) = \prod_{i<j} |x_i - x_j|$ explicitly prevents the B.E.C. story of overlapping bosons all lying in the ground $\cos(\pi x/L)$ state, as $\Psi \to 0$ whenever two bosons occupy the same space $x_i = x_j$. We can compare the results of the final prepared compressible states $N/L = 1/7...6/7$ to the theoretical predictions given by the analytic model of the infinitely interacting Tonks-Girardeau gas. We can use these analytics, in conjunction with our numerics and experimental results, to pursue observables and structure beyond just the location of population on our lattice.

5.5 Fluid Correlations

Intuitively, the photons inherit strong non-linearities from the qubit lattice sites. This results in repulsion between photons not just on a single site but between delocalized photons across the lattice which can be seen by the relative distortion from the expected cos distribution in the ground state as we add more particles. To measure the repulsion quantitatively, we measure correlations in population and position:

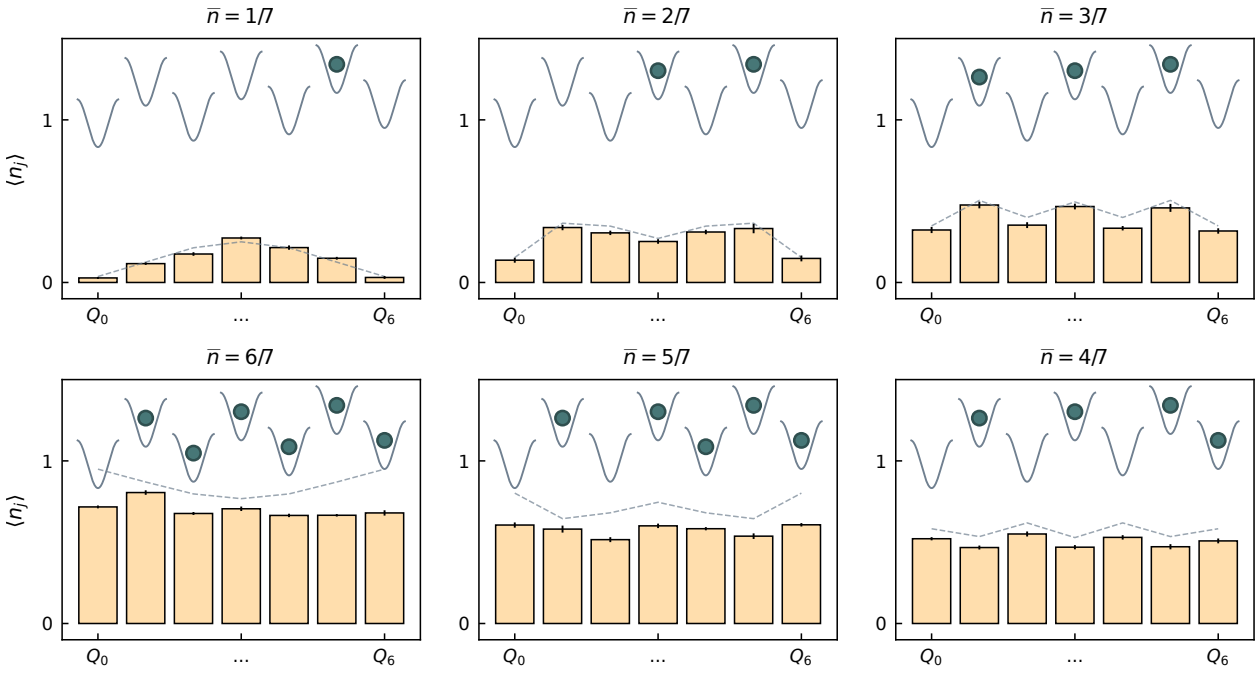

Figure 5.8: **Measured Density Profile vs Exact Diagonalization**. We measure the population distribution of the adiabatically prepared disorder-less states with lowest quasi-momenta varying density below unit filling. These are compared against the numerical results for exact diagonalization, where decreasing fidelity due to loss can be seen for higher particle number. Image from [2], Extended Data Figure 2.

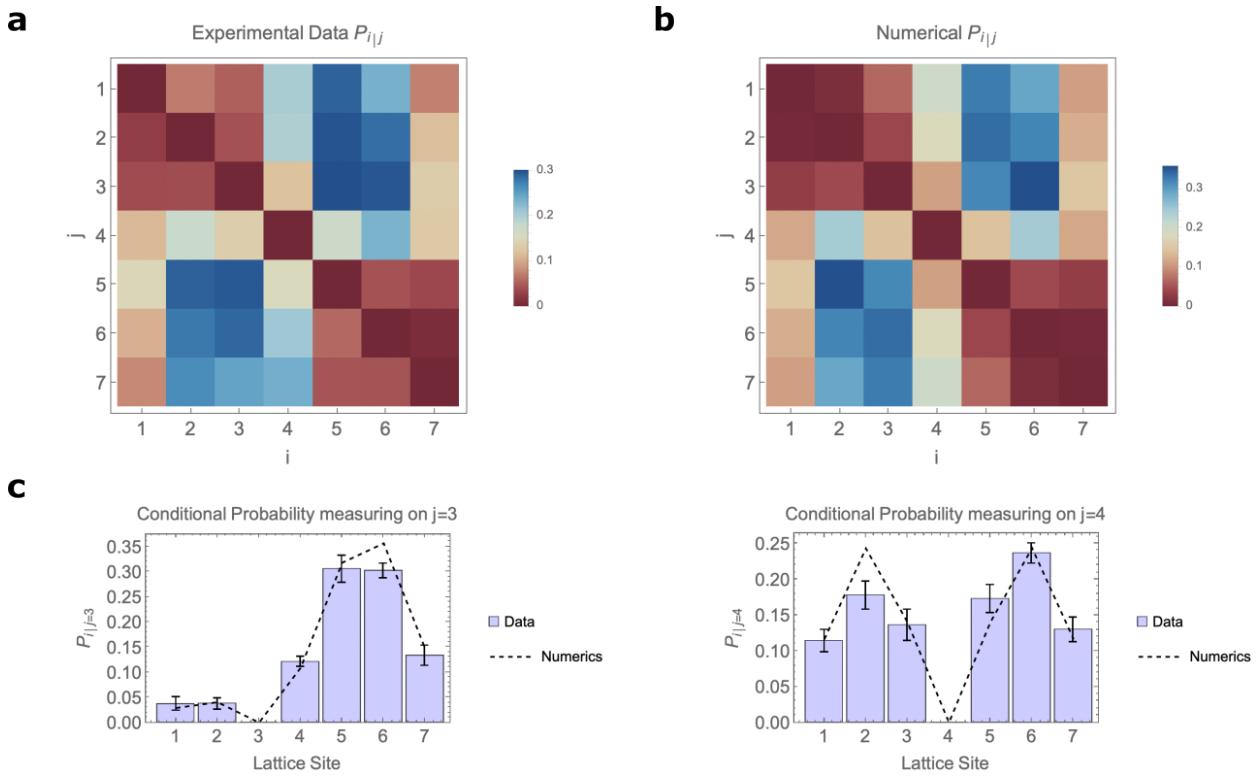

Figure 5.9: **Correlations in the strongly interacting fluid**. We observe particles avoiding one another. **a** The conditional probability $P_{i|j}$, the probability of detecting a photon at site i given detection of a photon at site j, for the two particle lowest quasi-momenta eigenstate. Anharmonicity suppresses detection of a second photon on the conditionally measured site, while the second photon is restricted to remain in the two "boxes" with suppressed amplitude near the detected photon. Figure similar to [2], Figure 4.

5.5.1 Conditional Probability

By looking at a conditional probability metric we can see how the distribution of the residual wavefunction changes after finding a particle on a lattice site, and how the residual wavefunction's distribution is influenced by the interaction.

The conditional probability metric $P_{i|j}$ we use is defined as the probability of detecting a photon at site Q_i *given* we have detected a photon at site Q_j. We restrict our measurement here to the two-particle case, so we can express our multi-particle wavefunction $\Psi(x_1, x_2)$. Once we detect one photon on a lattice site (x_j) the two-particle wavefunction collapses $\delta(x_1 - x_j)\psi(x_2)$ and the conditional probability metric of the second photon $P_{i|j} = |\psi(x_i)|^2$.

The full symmetric $P_{i|j}$ measured and exact numerical datasets can be seen in Fig. 5.9a,Fig. 5.9b, respectively. Cutouts representing the residual probability distributions after conditional detection of a particle on sites Q_3,Q_4 are presented in Fig. 5.9c, with numerical results accompanied. Simultaneous measurement of another excitation on the same site as the conditioned photon is prohibited due to the anharmonicity of the lattice sites - which we have folded into our "infinite interaction" description of the system. Thus, in this strongly interacting 1D system conditional measurement effectively partitions the lattice and confines the residual wavefunction to two boxes. Minimization of the population near the detected site reflects the influence of both repulsion and the minimization of kinetic energy from minimizing curvature of the wavefunction.

5.5.2 Density-Density Correlations

To look at the influence of interactions beyond the two-particle state we can look at the two-point density correlation function

$$g^{(2)}(x) = \frac{1}{\bar{n}^2} \sum_i \langle n_i n_{x+i} \rangle.$$

This tells us the probability of simultaneously detecting two particles separated by a distance of x lattice sites, normalized by the average density. From our previous results of the density distribution in the $N/L = 2/7$ case, we should expect to see a decreased probability of finding particles near one-another on the lattice.

The two-body density correlation measurements for the lowest quasi-momentum states for densities $N/L = 2/7$ to $6/7$ are shown in Fig. 5.10. With limited space on the finite lattice, placing more particles (increasing N/L) diminishes the normalized anti-bunching metric which accounts for the mutual repulsion - as there is decreasing space for photons to move to. For low separation values $x << L$ the asymptotic expansion of the pair correlation function for point-contact bosons (Here $H_{int} = \frac{U}{2} \sum_i \hat{n}(\hat{n} - 1)$) looks like [71]

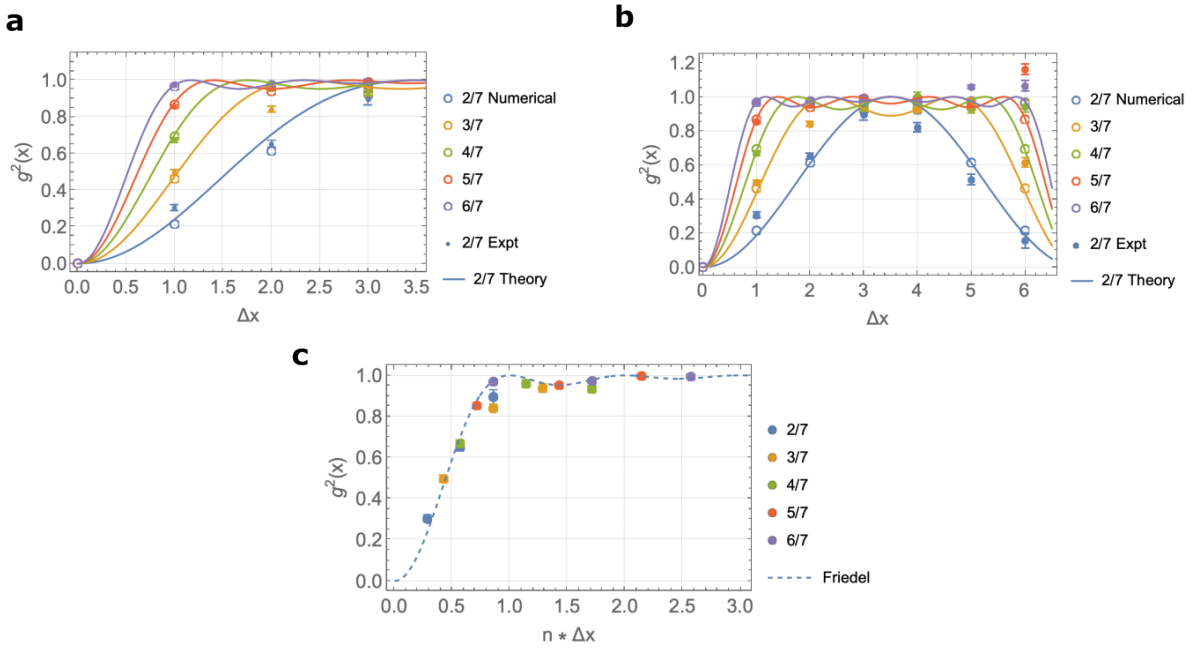

Figure 5.10: **Density-Density Correlations**. By measuring the population simultaneously on separate lattice sites, we can extract the density-density correlation metric $g^2(x)$, allowing us to see fermionization of the strongly interacting bosons. **a** Here, for lattice separation $x << L$ the $g^2(x)$ scales as $1 - (\sin a/(a))^2$ where $a = nx/L$ with a limiting behavior of $g^2(x) \to 1$. However, we quickly sample outside this limit in our lattice size and discover **b** the full symmetric behavior of the correlation function. In all cases The density-density correlation function, normalized across the lattice, shows anti-bunching of photons clearly at $\Delta x = 1$ which reduces as the density N/L increases - as photons have less space to separate. Measured values across densities match theoretical predictions for a Tonks gas of infinitely interacting bosons. **c** In the limit $x << L$ we can re-scale by the density n/L, and see that all measurements collapse to a density-independent Friedel oscillation with Fermi momenta $k_F = \pi\bar{n}$. Image similar to [2], Figure 4.

$$g^2(x) = 1 - \left(\frac{\sin(\pi\rho x)}{\pi\rho x}\right)^2$$

If we collect the measured correlation data for "low" separations $x \leq 3$ and re-normalize the measurements by the total density, all plots collapse to the same density-independent theoretical $g^2(x)$ curve (Fig. 5.10c), now demonstrating (more clearly) the expected Friedel oscillations of a fermionized Tonks-Girardeau gas with fermi momenta $k_F = \pi n$.

The full expression of the correlation function for the point-like bosons, which map to the spinless free fermion gas, is

$$g^2(x) = 1 - \left(\frac{\sin(\pi\rho x)}{n^{-1}\sin(\pi x L^{-1})}\right)^2$$

which is valid beyond the asymptotic limit $x << L$. We show the rest of our experimental data for the density-density correlation metric along with this expression in Fig. 5.10b.

5.6 Delocalization and Entanglement

Decreasing disorder adiabatically allows the localized excitations to tunnel and delocalize. As these photons delocalize they avoid one-another, which we have characterized by looking at the density-density correlation function. However, we have yet to probe the entanglement generated by the delocalization through tunneling between the lattice sites.

In our experimental setup we do not perform simultaneous readout of all lattice sites (left for future work!), so we do not directly measure the full density matrix of the system, only up to simultaneous pairs of sites. Thus, to track the change in entanglement of the instantaneous eigenstates over the entire lattice as disorder is removed, we track the entanglement each individual site have to the rest of the system. The global entanglement [74, 75] is an average of the impurity $1 - Tr(\rho_i^2)$ of each lattice site Q_i:

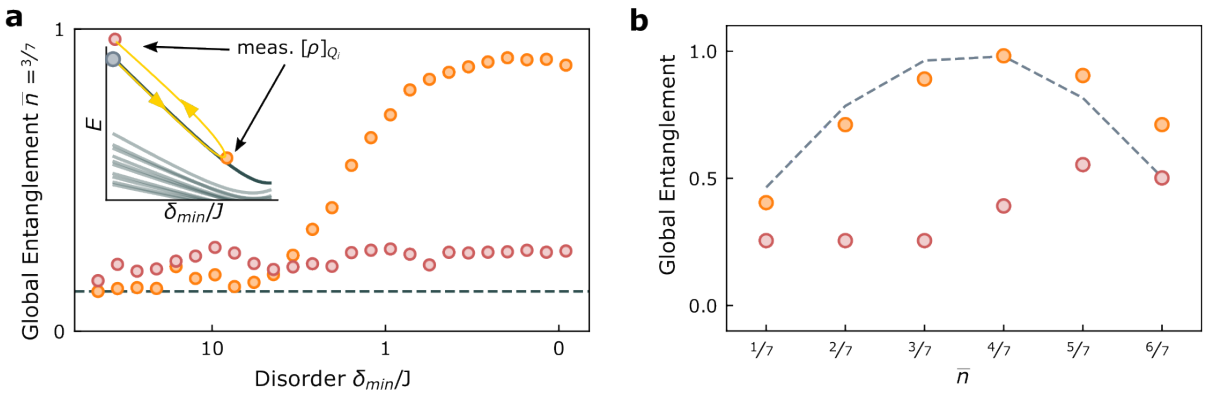

Figure 5.11: **Entanglement in the Fluid**. Tunneling of photons between lattice sites mediates entanglement as disorder is removed during the adiabatic ramp. To characterize this we measure the global entanglement $E_{gl} \equiv 2(1 - \langle Tr(\rho_i^2) \rangle)$ by tracking the total single-site impurities. **a** We measure E_{gl} for $N = 3$ during the adiabatic ramp and sample disorder values (orange), comparing to an adiabatically reversed ramp sequence (red) to rule out loss of single-site purity from environmental effects. **b** We vary the particle number and perform the same experiment, showing the final global entanglement values and reversed values for each case. The entanglement is maximized in the regime where particle-hole symmetry is highest (partial measurement here reveals the most about ψ), and increased particle loss is responsible for the deviation from symmetry and numerics as density increases. Image from [2], Figure 4.

$$E_{gl} = 2 - \frac{2}{N} \sum_{i=1}^{N} Tr(\rho_i^2)$$

When initially localized by disorder the many-body state ρ looks like a direct product of all ρ_i's, and thus the purity of a single qubit remains high when looking at localized eigenstates. As disorder is removed delocalization is mediated by tunneling and entanglement of the state grows across the lattice, contributing to the impurity of each site.

We measure the global entanglement as a function of disorder for $N/L = 3/7$ in Fig. 5.11. To make this measurement the lowest quasi-momentum three particle fluid is initially prepared in the localized stagger, then the disorder is ramped down adiabatically to the point we wish to sample where we return the lattice to the stagger configuration diabatically. At

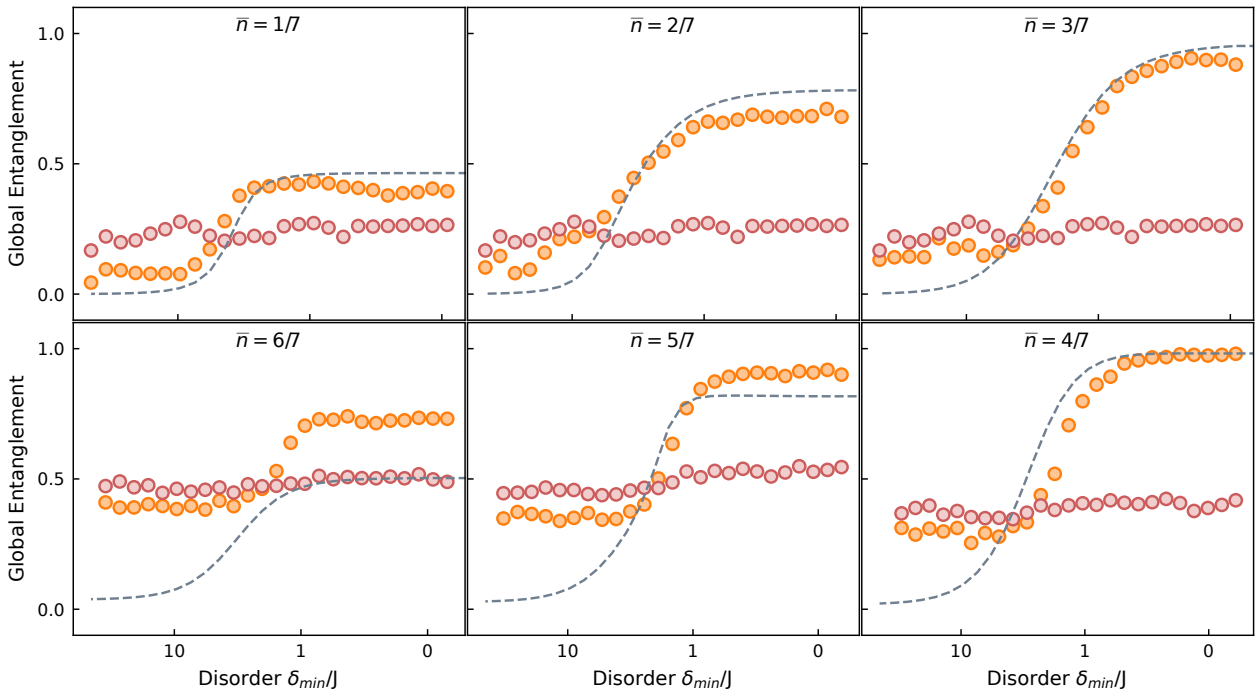

Figure 5.12: **Global Entanglement vs Filling**. We measure E_{gl} across the adiabatic delocalization trajectory for each compressible state below unit filling. Image from [2], Extended Data Figure 3.

this point we reconstruct the single-site density matrix ρ_i for each Q_i. This process is then repeated for each disorder value, sampled exponentially to the disorder-less lattice.

The mechanism we ascribe to the increase in impurity for single-qubit density matrices during this process is increased entanglement due to delocalization in the lattice. To exclude increased impurity due to decoherence from the environment itself we run a second reversible version of the experiment (Fig. 5.11a, inset) at each value of disorder (red) and show that the value of entanglement we measure after following an adiabatic trajectory in removing disorder and placing it back and measure a similar global entanglement as the initial value - excluding dephasing from the environment as a major contributor to our entanglement metric.

We measure the entanglement growth for densities $N/L = 1/7$ up to $6/7$ as well (Fig. 5.12), with dashed lines theoretical results coming from exact diagonalization of the system. We

can see that at half filling the entanglement is maximized - from an information perspective the number of available microstates is maximized at half-filling and diminish as either holes or particles become sparse. Thus partial measurement of a lattice site provides the most information of the system in the states near half-filling.

CHAPTER 6

OUTLOOK AND CONCLUSION

We now have a method to generate compressible eigenstates, either single or many-body, within the disorder-less lattice. Combined with previous work, we have access to both compressible and incompressible states of light, spanning the two phases of matter in the Bose-Hubbard phase diagram. If we consider the end of these experiments, the prepared many-body eigenstates, as starting points instead then these rich many-body eigenstates on the lattice lattice can be used for further experimentation.

In the work presented so far we have characterized the steady-state behavior of the eigenstates, but we have not examined dynamical physics possible with these states. Taking advantage of the same axis of control we used for state preparation, flux tuning, we can probe the susceptibility of the prepared fluid states on one end of the chain to a small periodic drive on the other (Fig. 6.1). Here we present, briefly, susceptibility measurements for the first three particle number eigenstates. By sweeping the drive frequency of the flux-driven qubit, we see larger responses close to the expected many-body phonon resonances in the susceptibility data. Further conclusions and experimental results along these lines will be left for future publications.

Quantum simulation is a leading technique to understand physical systems in the regime that intersect the many-body, the quantum, and the strongly interacting and strongly correlated. Traditional analytical tools and classical computation are insufficient on their own to tackle the fascinating new physics being demonstrated in these systems. To progress our understanding in this regime, many types of quantum simulators have been constructed. However, quantum simulation involves not only the construction of the analogous Hamiltonian but *also* the preparation of the (potentially complex) state of interest.

In this work we have described and presented the process for creating a one-dimensional array of transmon qubits, a cryogenic microwave circuit capable of simulating the Bose-

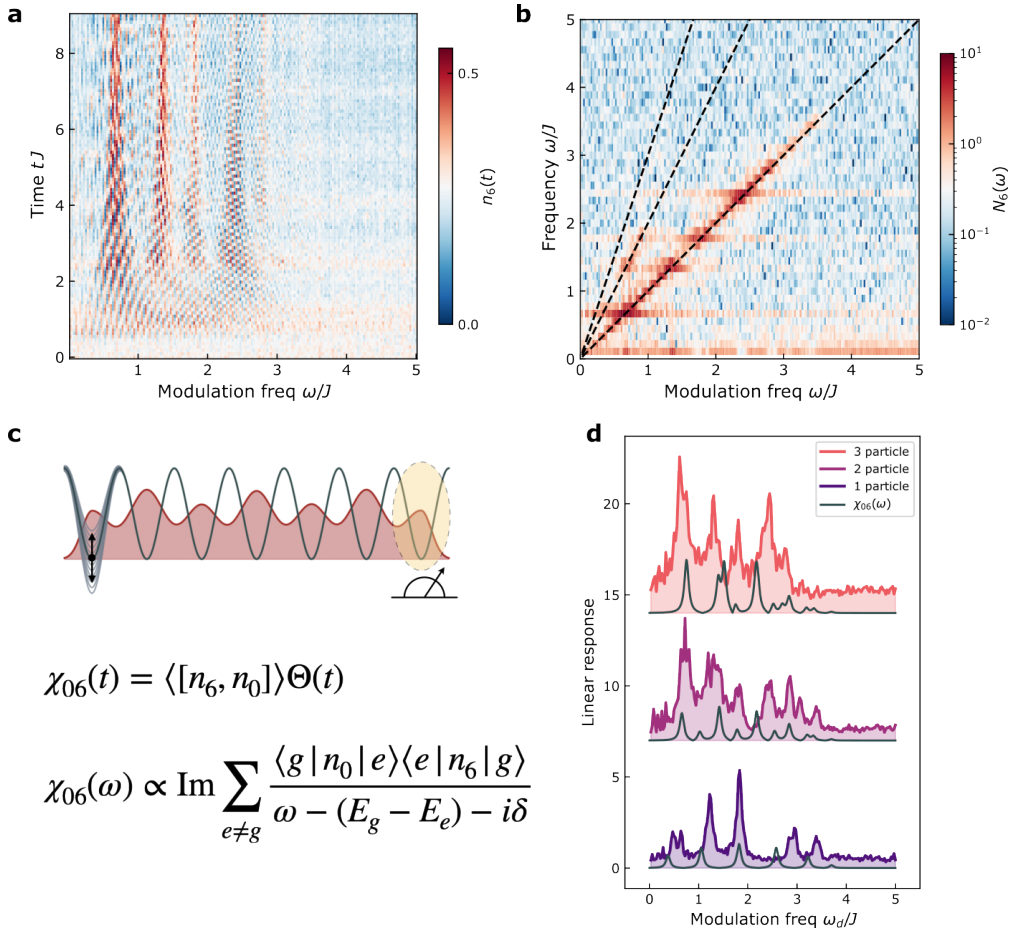

Figure 6.1: **AC Susceptibility**. One immediate extension is **c** probing the susceptibility to an AC drive on one end of the chain. We measure the **a** time-domain response at the other end of the chain to this drive and **b** the frequency response, with linear (diagonal, dashed) contributions at ω and higher non-linear responses at $2\omega, 3\omega$ (dashed). This process is repeated for different states **d**, and we compare the measured and expected response for each.

Hubbard Hamiltonian. Importantly, we have also presented a simple and extendable method for preparing the many-body compressible fluid states of light. That is, the frequency tunability of each qubit in our lattice can be thought of as disorder and an adiabatically tunable parameter, so we have tackled many-body state preparation through simplifying the system by localizing the eigenstates first, preparing excitations, then delocalizing by removing disorder.

We have presented benchmarks on the single-particle states and developed a metric, reversibility of the prepared state, to validate this process. Additionally, we have measured the particle number distribution for the first two quasi-momenta states in the first particle manifold, demonstrating our control over the eigenstates by simply choosing which qubit in the disordered configuration to excite.

We have also discussed measurements of higher particle numbers on the lattice, starting with particle density distributions for the lowest quasi-momenta states. These measurements are compared the expected distribution form exact diagonalization, which in turn is compared against the infinite interaction limit of the Tonks-Girardeau gas.

Further, we investigated the delocalization and entanglement growth that occurs for these multi-particle states as we removed disorder adiabatically. Delocalization was studied through two multi-site correlation metrics: the conditional probability measure $P_{i|j}$ and the density-density correlation function $g^2(x)$.

The conditional probability metric gave us insight into how, on the two-particle manifold, detection of a single particle re-shapes the residual probability distribution in the presence of strong interactions, strongly contrasting from the case where many identical bosons lying in the same state will yield little change in the residual distribution upon measurement. When we measured the density-density correlations on the lattice for different particle numbers (for the lowest quasi-momenta state) we saw the influence of strong interactions emerge in the anti-bunching ($g^2(x) < 1$) result. However, we also see in this measurement very nice

agreement between the theoretical predictions of the infinitely interacting Tonks-Girardeau model of a 1D fermionized chain of bosons and our system in the correlation function, allowing us to see Friedel oscillations (albeit small!) in the physics of our microwave photons.

We measured entanglement growth as we removed disorder by measuring the average impurity of each individual lattice site (E_{gl}), allowing us to track the entanglement growth of the many-body state for the lattice without measuring the full density matrix. We present measurements of the global entanglement metric for each of the lowest quasi-momenta compressible states and sample across decreasing disorder to track it's growth from the localized to delocalized cases. Additionally, we compare these measured values to the reversed case, where the ramp sequence is adiabatically brought back to the staggered configuration, where we observe a lack of entanglement growth which we use to rule out entanglement with elements outside the intended Hilbert space and conclude that entanglement is happening as theoretically expected with defects dominated by decay processes that scale with excitations.

This method of state preparation is broadly applicable. With ancilla qubits, OTOC's for measuring scrambling of quantum information [76] or probing anyon statistics [77]. Within chiral CQED lattices [78] the creation of nontrivial topological fluid states of light [79] is possible.

REFERENCES

[1] Houck, A. A. *et al.* Controlling the spontaneous emission of a superconducting transmon qubit. *Phys. Rev. Lett.* **101**, 080502 (2008).

[2] Saxberg, B. *et al.* Disorder-assisted assembly of strongly correlated fluids of light. *Nature* **612**, 435–441 (2022). URL `https://doi.org/10.1038/s41586-022-05357-x`.

[3] Anderson, P. W. More is different. *Science* **177**, 393–396 (1972). `https://www.science.org/doi/pdf/10.1126/science.177.4047.393`.

[4] Cohen, M. L. Essay: Fifty years of condensed matter physics. *Phys. Rev. Lett.* **101**, 250001 (2008).

[5] Kapitza, P. Viscosity of liquid helium below the λ-point. *Nature* **141**, 74–74 (1938).

[6] Anderson, M. H., Ensher, J. R., Matthews, M. R., Wieman, C. E. & Cornell, E. A. Observation of bose-einstein condensation in a dilute atomic vapor. *Science* **269**, 198–201 (1995). `https://www.science.org/doi/pdf/10.1126/science.269.5221.198`.

[7] Davis, K. B. *et al.* Bose-einstein condensation in a gas of sodium atoms. *Physical review letters* **75**, 3969 (1995).

[8] De-Picciotto, R. *et al.* Direct observation of a fractional charge. *Physica B: Condensed Matter* **249**, 395–400 (1998).

[9] Stormer, H. L. Nobel lecture: The fractional quantum hall effect. *Rev. Mod. Phys.* **71**, 875–889 (1999).

[10] Cooper, L. N. Bound electron pairs in a degenerate fermi gas. *Phys. Rev.* **104**, 1189–1190 (1956).

[11] Bardeen, J., Cooper, L. N. & Schrieffer, J. R. Microscopic theory of superconductivity. *Phys. Rev.* **106**, 162–164 (1957).

[12] Feynman, R. P. Simulating physics with computers. *International Journal of Theoretical Physics* **21**, 467–488 (1982).

[13] Bloch, I., Dalibard, J. & Nascimbene, S. Quantum simulations with ultracold quantum gases. *Nature Physics* **8**, 267–276 (2012).

[14] Greiner, M., Mandel, O., Esslinger, T., Hänsch, T. W. & Bloch, I. Quantum phase transition from a superfluid to a Mott insulator in a gas of ultracold atoms. *nature* **415**, 39–44 (2002).

[15] Bakr, W. S., Gillen, J. I., Peng, A., Fölling, S. & Greiner, M. A quantum gas microscope for detecting single atoms in a Hubbard-regime optical lattice. *Nature* **462**, 74–77 (2009).

[16] Trotzky, S. *et al.* Time-resolved observation and control of superexchange interactions with ultracold atoms in optical lattices. *Science* **319**, 295–299 (2008).

[17] Brown, P. T. *et al.* Bad metallic transport in a cold atom Fermi-Hubbard system. *Science* **363**, 379–382 (2019).

[18] Islam, R. *et al.* Measuring entanglement entropy in a quantum many-body system. *Nature* **528**, 77–83 (2015).

[19] Bluvstein, D. *et al.* Controlling quantum many-body dynamics in driven Rydberg atom arrays. *Science* **371**, 1355–1359 (2021).

[20] Blatt, R. & Roos, C. F. Quantum simulations with trapped ions. *Nature Physics* **8**, 277–284 (2012).

[21] Poyatos, J. F., Cirac, J. I. & Zoller, P. Quantum reservoir engineering with laser cooled trapped ions. *Physical review letters* **77**, 4728 (1996).

[22] Islam, R. *et al.* Onset of a quantum phase transition with a trapped ion quantum simulator. *Nature communications* **2**, 1–6 (2011).

[23] Joshi, M. K. *et al.* Observing emergent hydrodynamics in a long-range quantum magnet. *Science* **376**, 720–724 (2022).

[24] Britton, J. W. *et al.* Engineered two-dimensional ising interactions in a trapped-ion quantum simulator with hundreds of spins. *Nature* **484**, 489–492 (2012).

[25] Carusotto, I. *et al.* Photonic materials in circuit quantum electrodynamics. *Nature Physics* **16**, 268–279 (2020).

[26] Paraoanu, G.-S. Recent progress in quantum simulation using superconducting circuits. *Journal of Low Temperature Physics* **175**, 633–654 (2014).

[27] Ozawa, T. *et al.* Topological photonics. *Reviews of Modern Physics* **91**, 15006 (2019).

[28] Roushan, P. *et al.* Spectroscopic signatures of localization with interacting photons in superconducting qubits. *Science* **358**, 1175–1179 (2017).

[29] Karamlou, A. H. *et al.* Quantum transport and localization in 1d and 2d tight-binding lattices. *npj Quantum Information* **8**, 1–8 (2022).

[30] Fitzpatrick, M., Sundaresan, N. M., Li, A. C. Y., Koch, J. & Houck, A. A. Observation of a dissipative phase transition in a one-dimensional circuit qed lattice. *Phys. Rev. X* **7**, 011016 (2017).

[31] Kollár, A. J., Fitzpatrick, M. & Houck, A. A. Hyperbolic lattices in circuit quantum electrodynamics. *Nature* **571**, 45–50 (2019).

[32] Kollár, A. J., Fitzpatrick, M., Sarnak, P. & Houck, A. A. Line-graph lattices: Euclidean and non-Euclidean flat bands, and implementations in circuit quantum electrodynamics. *Communications in Mathematical Physics* **376**, 1909–1956 (2020).

[33] Owens, J. C. *et al.* Chiral Cavity Quantum Electrodynamics. *arXiv preprint arXiv:2109.06033* (2021).

[34] Andersen, T. I. *et al.* Observation of non-abelian exchange statistics on a superconducting processor. *arXiv preprint arXiv:2210.10255* (2022).

[35] Ketterle, W. Nobel lecture: When atoms behave as waves: Bose-Einstein condensation and the atom laser. *Reviews of Modern Physics* **74**, 1131 (2002).

[36] Ma, R., Owens, C., Houck, A., Schuster, D. I. & Simon, J. Autonomous stabilizer for incompressible photon fluids and solids. *Physical Review A* **95**, 43811 (2017).

[37] Ma, R. *et al.* Author Correction: A dissipatively stabilized Mott insulator of photons. *Nature* **570**, E52–E52 (2019).

[38] Martinis, J. M. & Osborne, K. Superconducting qubits and the physics of josephson junctions (2004).

[39] Koch, J. *et al.* Charge-insensitive qubit design derived from the Cooper pair box. *Phys. Rev. A* **76**, 42319 (2007).

[40] Bronn, N. T. *et al.* Broadband filters for abatement of spontaneous emission in circuit quantum electrodynamics. *Applied Physics Letters* **107**, 172601 (2015).

[41] Pozar, D. *Microwave Engineering* (Wiley, 2011).

[42] Josephson, B. D. Possible new effects in superconductive tunnelling. *Physics letters* **1**, 251–253 (1962).

[43] Josephson, B. D. The discovery of tunnelling supercurrents. *Rev. Mod. Phys.* **46**, 251–254 (1974).

[44] You, X., Sauls, J. A. & Koch, J. Circuit quantization in the presence of time-dependent external flux. *Phys. Rev. B* **99**, 174512 (2019).

[45] Jaynes, E. & Cummings, F. Comparison of quantum and semiclassical radiation theories with application to the beam maser. *Proceedings of the IEEE* **51**, 89–109 (1963).

[46] Koch, J. *et al.* Charge-insensitive qubit design derived from the cooper pair box. *Phys. Rev. A* **76**, 042319 (2007).

[47] Sete, E. A., Martinis, J. M. & Korotkov, A. N. Quantum theory of a bandpass purcell filter for qubit readout. *Phys. Rev. A* **92**, 012325 (2015).

[48] Heinsoo, J. *et al.* Rapid High-fidelity Multiplexed Readout of Superconducting Qubits. *Physical Review Applied* **10**, 34040 (2018).

[49] Nigg, S. E. *et al.* Black-box superconducting circuit quantization. *Physical Review Letters* **108**, 240502 (2012).

[50] Braumüller, J. *et al.* Characterizing and optimizing qubit coherence based on squid geometry. *Phys. Rev. Applied* **13**, 054079 (2020).

[51] Chen, Y. *et al.* Qubit architecture with high coherence and fast tunable coupling. *Physical review letters* **113**, 220502 (2014).

[52] Barends, R. *et al.* Coherent josephson qubit suitable for scalable quantum integrated circuits. *Phys. Rev. Lett.* **111**, 080502 (2013).

[53] Kelly, J. S. *Fault-tolerant superconducting qubits* (University of California, Santa Barbara, 2015).

[54] Chen, Y. *et al.* Qubit architecture with high coherence and fast tunable coupling. *Phys. Rev. Lett.* **113**, 220502 (2014).

[55] Kim, E. *et al.* Quantum electrodynamics in a topological waveguide. *Phys. Rev. X* **11**, 011015 (2021).

[56] Place, A. P. *et al.* New material platform for superconducting transmon qubits with coherence times exceeding 0.3 milliseconds. *Nature communications* **12**, 1–6 (2021).

[57] Chen, Z. *et al.* Fabrication and characterization of aluminum airbridges for superconducting microwave circuits. *Applied Physics Letters* **104**, 052602 (2014).

[58] Vepsäläinen, A. P. *et al.* Impact of ionizing radiation on superconducting qubit coherence. *Nature* **584**, 551–556 (2020).

[59] Krinner, S. *et al.* Engineering cryogenic setups for 100-qubit scale superconducting circuit systems. *EPJ Quantum Technology* **6**, 2 (2019).

[60] Pop, I. M. *et al.* Coherent suppression of electromagnetic dissipation due to superconducting quasiparticles. *Nature* **508**, 369–372 (2014).

[61] Santavicca, D. & Prober, D. Impedance-matched low-pass stripline filters. *Measurement Science and Technology* **19**, 087001 (2008).

[62] Reed, M. D. *et al.* High-fidelity readout in circuit quantum electrodynamics using the jaynes-cummings nonlinearity. *Phys. Rev. Lett.* **105**, 173601 (2010).

[63] Lienhard, B. *et al.* Deep-neural-network discrimination of multiplexed superconducting-qubit states. *Physical Review Applied* **17**, 014024 (2022).

[64] Hradil, Z. Quantum-state estimation. *Phys. Rev. A* **55**, R1561–R1564 (1997).

[65] Abrams, D. M., Didier, N., Caldwell, S. A., Johnson, B. R. & Ryan, C. A. Methods for measuring magnetic flux crosstalk between tunable transmons. *Phys. Rev. Applied* **12**, 064022 (2019).

[66] Dai, X. *et al.* Optimizing for periodicity: a model-independent approach to flux crosstalk calibration for superconducting circuits (2022).

[67] Langford, N. K. *et al.* Experimentally simulating the dynamics of quantum light and matter at deep-strong coupling. *Nature Communications* **8**, 1715 (2017).

[68] Rol, M. A. *et al.* Fast, high-fidelity conditional-phase gate exploiting leakage interference in weakly anharmonic superconducting qubits. *Phys. Rev. Lett.* **123**, 120502 (2019).

[69] Wittig, C. The landau- zener formula. *The Journal of Physical Chemistry B* **109**, 8428–8430 (2005).

[70] Tonks, L. The complete equation of state of one, two and three-dimensional gases of hard elastic spheres. *Physical Review* **50**, 955 (1936).

[71] Girardeau, M. Relationship between systems of impenetrable bosons and fermions in one dimension. *Journal of Mathematical Physics* **1**, 516–523 (1960).

[72] Bijl, A. The lowest wave function of the symmetrical many particles system. *Physica* **7**, 869–886 (1940).

[73] Cazalilla, M. A., Citro, R., Giamarchi, T., Orignac, E. & Rigol, M. One dimensional bosons: From condensed matter systems to ultracold gases. *Rev. Mod. Phys.* **83**, 1405–1466 (2011).

[74] Amico, L., Fazio, R., Osterloh, A. & Vedral, V. Entanglement in many-body systems. *Reviews of Modern Physics* **80**, 517–576 (2008).

[75] Meyer, D. A. & Wallach, N. R. Global entanglement in multiparticle systems. *J. Math. Phys* **43**, 4273 (2002).

[76] Swingle, B., Bentsen, G., Schleier-Smith, M. & Hayden, P. Measuring the scrambling of quantum information. *Physical Review A* **94**, 40302 (2016).

[77] Grusdt, F., Yao, N. Y., Abanin, D., Fleischhauer, M. & Demler, E. Interferometric measurements of many-body topological invariants using mobile impurities. *Nature communications* **7**, 1–9 (2016).

[78] Clark, L. W., Schine, N., Baum, C., Jia, N. & Simon, J. Observation of Laughlin states made of light. *Nature* **582**, 41–45 (2020).

[79] Grusdt, F., Letscher, F., Hafezi, M. & Fleischhauer, M. Topological growing of laughlin states in synthetic gauge fields. *Physical review letters* **113**, 155301 (2014).